國立臺灣大學理學院大氣科學系

碩士論文

Department of Atmospheric Sciences

College of Science

National Taiwan University

Master's Thesis

2022 年 TAHOPE 期間兩場梅雨鋒面個案之比較：探討造成降水特徵差異的物理機制

A Comparison of Two Meiyu Front Cases during TAHOPE 2022: Exploring the Physical Mechanisms for the Differences in Precipitation Features

朱品瑞

Pin-Rui Zhu

指導教授：楊明仁 博士

Advisor: Ming-Jen Yang, Ph.D.

中華民國 114 年 12 月

December 2025

doi:10.6342/NTU202504817

國立臺灣大學碩士學位論文
口試委員會審定書

本論文係 朱品瑞 君（學號 R12229013 ）在國立臺灣大學大氣科學學系、所完成之碩士學位論文，於民國 114 年 11 月 7 日承下列考試委員審查通過及口試及格，特此證明

口試委員：

楊明仁 （簽名）
（指導教授）

侯昭平　　王重傑

李欣翰　　陳正平

系主任、所長 （簽名）

doi:10.6342/NTU202504817

誌謝

時光飛逝，轉眼間兩年半的碩士生涯即將畫下句點，也代表著我馬上就要從熟悉的學生身份正式轉換為職場新鮮人，因此，我格外珍惜這最後的在學時光，並十分幸運在此期間內，能向許多優秀的師長與同儕學習，亦有一群好朋友彼此加油打氣，心中滿懷感激。首先，我要感謝我的指導教授楊明仁老師，給予我許多發現問題、獨立思考、嘗試錯誤，並善用各種既有資源解決問題的機會與訓練，相信這些寶貴的經驗一定會成為我日後人生旅途中相當重要的助力。同時，我也要感謝口試委員陳正平老師、王重傑老師、宋偉國老師以及侯昭平老師，謝謝您們在口試前用心閱讀我的論文初稿，並給予我溫暖的鼓勵與祝福，亦於口試時提供許多精闢的回饋與建議，使本研究的內容得以更加周延。

接著，我要感謝我的爸媽，謝謝您們始終給予我滿滿的關懷與支持，耐心傾聽我對生活中各種大小事的抱怨，並為我打造最堅固、最溫暖的避風港，使我得以順利完成碩士學業。同時，也要感謝對流與降水實驗室的好夥伴們：感謝茂正學長與炯恩學長不厭其煩地與我進行科學討論及經驗傳承；感謝尚恩學長、英璋學長與九令在程式技術上的分享與即時救援；感謝伃茗為我的日常生活帶來許多溫暖的交流、協助與關心；也感謝瑞均、彥葦與晴葳在各項重要時刻之前所給予的鼓勵，很開心能和大家一同在實驗室中努力與成長。

此外，感謝我的室友 Allen，你的友善與包容，讓我的住宿生活如同在家一般自在舒適，也使我能突破白天與夜晚的限制，在身體與精神狀態允許的任何時間盡全力趕工，很高興在這兩年半內，能與你共同創造如此美好的住宿回憶；同時，也感謝心宇、映汝、俊能、育銓、洸宇、小平等好友平時陪我聊天、吃飯或出門散心，這段時間內有你們的真心相伴，使我平凡的生活增添了許多色彩。

最後，感謝警察廣播電臺的好節目、好音樂，陪伴了我無數個從白天努力到黑夜，再從黑夜努力到白天的日子；也要感謝這次有堅持到底的品瑞，雖然接下來的旅程可能不會一帆風順，但只要能秉持這份精神，相信所有挑戰最終都能迎刃而解！

doi:10.6342/NTU202504817

摘要

在 2022 年 5 月 25 日至 8 月 10 日進行的臺灣區域豪雨觀測與預報實驗(Taiwan-Area Heavy rain Observation and Prediction Experiment, TAHOPE)中，本研究選取了兩道梅雨鋒面個案進行分析，分別對應第一次特別觀測期(Special Observation Period 1, SOP1)與第三次密集觀測期(Intensive Observation Period 3, IOP3)。儘管於 5 月 25 日(SOP1)與 6 月 6 日(IOP3)的 0700–1900 UTC 期間，這兩道梅雨鋒面在臺灣海峽中北部之 975 hPa 等壓面上具有相當接近的平均位置，但 SOP1 個案在北臺灣(桃園以北)地區產生的總降水量卻接近 IOP3 個案的三倍，呈現非常顯著的差異，本研究旨在探討造成此降水差異的可能因素與物理機制。

分析結果顯示，儘管 IOP3 個案的鋒面斜率、鋒面強度及綜觀尺度的運動學特徵相較於 SOP1 個案而言均明顯偏強，但 SOP1 個案具備更有利的熱力條件及中小尺度運動場結構(如：持續性的低層輻合帶，可不斷激發新對流胞)，並伴隨著較顯著的碰撞合併過程、較高的低層液態水含量與可能較高的雲微物理尺度降水效率，這些因素共同促使 SOP1 個案在北臺灣地區產生明顯高於 IOP3 個案的總累積雨量，因此鋒面過境時所伴隨的降水多寡可能並非單純由其結構與強度所決定，而是環境水氣含量、中小尺度過程與雲微物理過程綜合作用之下的結果。

關鍵詞：TAHOPE、梅雨鋒面、低層輻合帶、碰撞合併、低層液態水含量。

doi:10.6342/NTU202504817

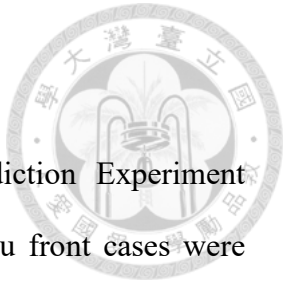

Abstract

During the Taiwan-Area Heavy rain Observation and Prediction Experiment (TAHOPE) conducted from 25 May to 10 August 2022, two Meiyu front cases were selected for investigation in this study, corresponding to Special Observation Period 1 (SOP1) and Intensive Observation Period 3 (IOP3), respectively.

Although the two Meiyu fronts at 975 hPa were similarly positioned over the central to northern Taiwan Strait between 0700 UTC and 1900 UTC on 25 May (the SOP1 case) and 6 June (the IOP3 case), the rainfall totals observed over northern Taiwan (over and north of Taoyuan) in the SOP1 case were nearly three times as much as those in the IOP3 case, showing a highly significant difference. This study aimed to uncover the possible controlling factors and physical mechanisms responsible for this contrast.

Our analysis indicated that although the IOP3 case exhibited a noticeably steeper frontal slope, greater frontal intensity, and stronger synoptic-scale kinematic features, the SOP1 case possessed more favorable thermodynamic conditions and mesoscale-to-convective-scale kinematic structures (e.g., persistent low-level convergence zones repeatedly initiating new convection), along with more pronounced collision-coalescence, higher low-level liquid water content, and potentially greater cloud-microphysics precipitation efficiency. These factors collectively led to substantially higher accumulated rainfall over northern Taiwan in the SOP1 case than in the IOP3 case, suggesting that the amount of precipitation during the frontal passages may not be solely determined by the structure and intensity of the front, but rather by the combined effects of environmental moisture and both mesoscale-to-convective-scale and microphysical processes.

Keywords: TAHOPE, Meiyu front, Low-level convergence zones, Collision-coalescence, Low-level liquid water content

doi:10.6342/NTU202504817

Table of Contents

國立臺灣大學碩士學位論文 口試委員會審定書 i

誌謝 ii

摘要 iii

Abstract iv

Table of Contents v

List of Tables vii

List of Figures ix

Chapter 1 Introduction 1

1.1 Literature Review 1

1.2 Overview of TAHOPE 2022 4

1.3 Motivation 6

1.4 Thesis Organization 7

Chapter 2 Data and Methods 8

2.1 Dataset Descriptions 8

2.1.1 Synoptic-Scale Analysis Data 8

2.1.2 Surface Station and QPESUMS Data 9

2.1.3 Sounding and Radar Data 10

2.2 Study Area 11

2.3 Definition of the Meiyu Front 12

2.4 Radar Data Preprocessing 14

2.5 3D Wind Retrieval 14

2.6 Interpretations of Dual-Polarization Radar Parameters 15

2.7 Convective-Stratiform Separation Algorithm 20

2.8 Methods for Identifying Low-Level Size Sorting Signature 23

doi:10.6342/NTU202504817

Chapter 3 Case Overview 26

3.1 Overall Precipitation Features 26

3.2 Overall Comparison of the Two Selected Periods 27

Chapter 4 Analysis Results 30

4.1 Synoptic Insights 30

4.2 Thermodynamic Insights 36

4.3 Kinematic Insights 39

4.3.1 The SOP1 Case 40

4.3.2 The IOP3 Case 42

4.4 Warm-Cloud Microphysical Insights 43

4.4.1 Temporal Evolution of Different Precipitation Regimes 43

4.4.2 Temporal Evolution of S-Pol PID and Polarimetric Parameters 45

4.4.3 CFAD Analysis for EP1 48

4.4.4 CFAD Analysis for EP2 52

4.4.5 Parameter Space Analysis 54

4.4.6 Low-Level Size Sorting Signature for the IOP3 Case 56

Chapter 5 Conclusions and Future Work 59

5.1 Conclusions 59

5.2 Future Work 62

References 63

Tables 69

Figures 77

doi:10.6342/NTU202504817

List of Tables

Table 1.1 List of IOPs and SOPs during TAHOPE 2022. (adapted from 楊明仁等，2023)..... 69

Table 2.1 Descriptions for ERA5 reanalysis data..... 70

Table 2.2 Descriptions for CWB QPESUMS product in Taiwan..... 70

Table 2.3 Basic specifications of the S-Pol, RCWF, and RCSL radars. In the following table, PPI stands for Plan Position Indicator, and RHI stands for Range Height Indicator..... 71

Table 2.4 Summary of the classification criteria for different precipitation regimes based on radar reflectivity at 2-km height and the height of 20-dB*Z* echo top..... 72

Table 4.1 Summary of the synoptic-scale statistical analysis for the SOP1 and IOP3 cases. Values in parentheses indicate the relative strength of the stronger case compared to the weaker case, expressed as percentages. The cross (✕), ballot box with check (☑), and ordinary check mark (✓) denote the weaker case, the stronger case with relative strength ≥ 10%, and the stronger case with relative strength < 10%, respectively..... 73

Table 4.2 Hourly fractions (%) of the total convective precipitation regimes (including deep, moderate, and shallow convection), stratiform precipitation regimes, and weak-echo regions for the SOP1 case. The orange- and white-shaded portions denote the first and second episodes of enhanced surface precipitation, respectively..... 74

Table 4.3 As in Table 4.2, but for the IOP3 case..... 74

Table 4.4 Hourly fractions (%) of the deep convection, moderate convection, and shallow convection for the SOP1 case. The orange- and white-shaded

doi:10.6342/NTU202504817

portions denote the first and second episodes of enhanced surface precipitation, respectively. 75

Table 4.5 As in Table 4.4, but for the IOP3 case. 75

Table 5.1 Summary of the key findings in this study. “Collision-coalescence” is abbreviated as “Collision”. 76

doi:10.6342/NTU202504817

List of Figures

Figure 1.1 Different microphysical fingerprints for liquid-phase precipitation, including (a) coalescence, (b) breakup, (c) evaporation, and (d) size sorting. The lighter cyan shading in (c) indicates a range of possible fingerprints for Z_{DR}. The value of each polarimetric parameter is on the horizontal axis, increasing rightward, whereas height is on the vertical axis, increasing upward. (Kumjian et al. 2022)..... 77

Figure 1.2 As in Figure 1.1, but for ice-phase precipitation including (a) vapor depositional growth of ice crystals, (b) aggregation, (c) riming, (d) riming with the Hallett-Mossop rime splintering process occurring, (e) sublimation, (f) refreezing, and (g) melting. The purple shading in (e) indicates a range of possible fingerprints for K_{DP}. The dashed and solid lines in (f) show the refreezing of partially and fully melted hydrometeors, respectively. (Kumjian et al. 2022)..... 78

Figure 2.1 Locations of the 86 surface stations used to analyze precipitation features in the two Meiyu front cases. Dot color indicates station elevation..... 79

Figure 2.2 Locations of sounding and radar stations. Azimuth is measured following the meteorological convention, with 0° denoting true north and increasing clockwise..... 79

Figure 2.3 The study area for statistical analysis of the synoptic environment. The red rectangle indicates the region used for analyzing the barrier jet and integrated vapor transport (IVT) divergence, while the blue rectangle denotes the region where other thermodynamic and kinematic parameters are examined..... 80

Figure 2.4 The study area for the analysis of cloud microphysical characteristics

doi:10.6342/NTU202504817

(indicated by the red color shading). 80

Figure 2.5 Schematic of 975-hPa Meiyu front identification based on adopted criteria, shown for 6/06 0300 Z. Only the region enclosed by the two black lines is identified as the Meiyu front. Color shading indicates horizontal θ_e gradient (K/1000 km), and green dots mark locations with relative vorticity > 5×10^{-5} s^{-1}. 81

Figure 2.6 Typical Z_{DR} values for raindrops of various sizes and hail. Black arrows beside the hail particle represent spinning and tumbling motions. (Wakimoto and Bringi 1988; Houze 2014) 82

Figure 2.7 Schematic illustration of the spatial relationship among a convective center, its background region, and the resulting convective precipitation regime. (Steiner et al. 1995; Houze 2014)..... 82

Figure 2.8 An example of the output from the convective-stratiform separation algorithm at 6/06 0800 Z. (a) S-Pol radar reflectivity at 2-km height. (b) Corresponding classification result. 83

Figure 2.9 An example of size sorting object identification at 6/06 0848 Z. Background colors show radar observations of (a) Z_{DR} and (b) K_{DP} at 1.5-km height. Red and blue contours indicate regions where Z_{DR} and K_{DP} values exceed the magnitude thresholds, respectively. For contour objects that also satisfy the size thresholds and are considered valid pairings, the centroids of Z_{DR} and K_{DP} objects are marked with red circles and blue squares, respectively. 83

Figure 3.1 CWB daily accumulated rainfall maps for (a) 5/25 LST, (b) 5/26 LST, (c) 5/27 LST, and (d) 5/28 LST. Source: Central Weather Bureau (CWB). 84

Figure 3.2 As in Figure 3.1, but for (a) 6/06 LST, (b) 6/07 LST, (c) 6/08 LST, and

doi:10.6342/NTU202504817

(d) 6/09 LST. Source: Central Weather Bureau (CWB). 85

Figure 3.3 Hourly accumulated precipitation averaged over the 86 surface stations located in and north of Taoyuan during (a) 5/24 0000 Z–5/27 0000 Z, (b) 6/06 0000 Z–6/09 0000 Z, (c) 5/25 0700–1900 Z, and (d) 6/06 0700–1900 Z. Black boxes in (a) and (b) mark the two 12-hour periods analyzed, whose time series are shown in (c) and (d), with color shading highlighting two episodes of enhanced surface precipitation..... 87

Figure 3.4 The average position of the Meiyu front at the 975-hPa level during (a) 5/25 0700–1900 Z (SOP1 case) and (b) 6/06 0700–1900 Z (IOP3 case). Color shading indicates horizontal θ_e gradient (K/1000 km), and green dots mark locations with relative vorticity > 5×10^{-5} s^{-1}..... 87

Figure 3.5 12-hour accumulated rainfall statistics over the 86 surface stations in and north of Taoyuan during 5/25 0700–1900 Z (SOP1 case) and 6/06 0700–1900 Z (IOP3 case). For each boxplot, the five numbers from bottom to top on the left-hand side correspond to the minimum, first quartile, median (second quartile), third quartile, and maximum..... 88

Figure 3.6 12-hour accumulated quantitative precipitation estimation (QPE) during (a) 5/25 0700–1900 Z (SOP1 case) and (b) 6/06 0700–1900 Z (IOP3 case). 88

Figure 3.7 The Hovmöller diagrams of 12-hour accumulated QPE along the east-west cross-section at 25°N for (a) 5/25 0700–1900 Z (SOP1 case) and (b) 6/06 0700–1900 Z (IOP3 case). In each panel, the values were averaged over a 0.0625° (≈15 km) meridional band, indicated by the red box in (c). Furthermore, the thick black dashed lines in (a) and (b) represent the location of the coast, with the terrain profile displayed at the bottom of

doi:10.6342/NTU202504817

both panels. 89

Figure 4.1 JMA surface weather charts for (a) 5/25 0000 Z, (b) 5/25 0600 Z, (c) 5/25 1200 Z, and (d) 5/25 1800 Z. Source: Japan Meteorological Agency (JMA). 90

Figure 4.2 As in Figure 4.1, but for (a) 6/06 0000 Z, (b) 6/06 0600 Z, (c) 6/06 1200 Z, and (d) 6/06 1800 Z. Source: Japan Meteorological Agency (JMA). 91

Figure 4.3 12-hour averaged weather charts at (a) 700 hPa, (b) 500 hPa, and (c) 200 hPa for the SOP1 case. Black contours denote geopotential height (gpm). In panels (a) and (b), color shading indicates relative vorticity (10^{-5} s^{-1}) and wind barbs show horizontal winds (knots). In panel (c), color shading represents divergence (10^{-5} s^{-1}), arrows denote horizontal wind direction, and red contours mark the isotach of 50 m s^{-1}, highlighting the approximate location of the upper-level jet stream. 92

Figure 4.4 As in Figure 4.3, but for the IOP3 case. 93

Figure 4.5 Schematic of the north-south cross section at 121°E, extending from 24°N to 28°N (red line). 94

Figure 4.6 Vertical cross-section of θ_e (color shading; K) and v-w wind (arrows; m s^{-1}, with vertical velocity multiplied by 100) along the north-south section shown in Figure 4.5, for the SOP1 case at (a) 0600 Z, (b) 1200 Z, and (c) 1800 Z. 95

Figure 4.7 As in Figure 4.6, but for the IOP3 case at (a) 0600 Z, (b) 1200 Z, and (c) 1800 Z. 96

Figure 4.8 Vertical cross-section of θ (color shading; K) and v-w wind (arrows; m s^{-1}, with vertical velocity multiplied by 100) along the north-south section shown in Figure 4.5, for the SOP1 case at (a) 0600 Z, (b) 1200 Z, and (c)

doi:10.6342/NTU202504817

1800 Z. 97

Figure 4.9 As in Figure 4.8, but for the IOP3 case at (a) 0600 Z, (b) 1200 Z, and (c) 1800 Z. 98

Figure 4.10 Time series of the regionally averaged (a) frontal slope and (b) horizontal θ_e gradient (K/1000km; indicator of frontal intensity) at the 975-hPa level for the SOP1 case (blue line) and the IOP3 case (red line). 99

Figure 4.11 Sounding observations at Banqiao station for (a) 5/25 0000 Z (SOP1 case) and (b) 6/06 0000 Z (IOP3 case), with the temperature profile in blue and the dewpoint profile in red. 100

Figure 4.12 As in Figure 4.11, but for (a) 5/25 1200 Z (SOP1 case) and (b) 6/06 1200 Z (IOP3 case). 101

Figure 4.13 The temporal evolution of the difference between the saturation equivalent potential temperature (θ_{es}) and the equivalent potential temperature (θ_e), i.e., the saturation deficit, at Banqiao station for the IOP3 case at 0000 Z (red line), 0600 Z (green line), 1200 Z (blue line), and 1800 Z (pink line). 102

Figure 4.14 Horizontal winds at 2-km height retrieved from SAMURAI-TERRAIN (barbs; knots), convergence (blue dashed contours; s^{-1}, thick and thin contours denote -10×10^{-4} s^{-1} and -5×10^{-4} s^{-1}, respectively), and CWB composite reflectivity (color shading; dB*Z*) for the SOP1 case at (a) 0700 Z, (b) 0736 Z, (c) 0800 Z, and (d) 0836 Z. 103

Figure 4.15 As in Figure 4.14, but for the SOP1 case at (a) 0900 Z, (b) 1000 Z, (c) 1100 Z, (d) 1200 Z, and (e) 1336 Z. 104

Figure 4.16 As in Figure 4.14, but for the IOP3 case at (a) 0800 Z, (b) 0900 Z, (c) 1000 Z, and (d) 1100 Z. 105

doi:10.6342/NTU202504817

Figure 4.17 As in Figure 4.14, but for the IOP3 case at (a) 1500 Z, (b) 1600 Z, (c) 1700 Z, and (d) 1800 Z. 106

Figure 4.18 Temporal evolution of the total convective precipitation regimes (red line; including deep, moderate, and shallow convection), stratiform precipitation regimes (cyan line), and weak-echo regions (blue line) for (a) 5/25 0800–1900 Z and (b) 6/06 0800–1900 Z. 107

Figure 4.19 Temporal evolution of deep convection (red line), moderate convection (orange line), and shallow convection (green line) for (a) 5/25 0800–1900 Z and (b) 6/06 0800–1900 Z. 108

Figure 4.20 Temporal evolution of the fractions of S-Pol rain PID (light, moderate, and heavy rain) and polarimetric parameters at 1.5-km height for the SOP1 case: (a) rain PID, (b) Z_H, (c) Z_{DR}, and (d) K_{DP}. The first and second episodes of enhanced surface precipitation are bounded by yellow and orange lines, respectively. 109

Figure 4.21 As in Figure 4.20, but for the IOP3 case. 110

Figure 4.22 CFADs (%) of Z_H for EP1. (a),(c),(e) correspond to the SOP1 case, and (b),(d),(f) to the IOP3 case, with panels arranged by row as entire domain, convective, and stratiform precipitation regimes. The black line in each panel indicates mean profile. 111

Figure 4.23 As in Figure 4.22, but for CFADs (%) of Z_{DR}. 112

Figure 4.24 As in Figure 4.22, but for CFADs (%) of K_{DP}. 113

Figure 4.25 As in Figure 4.22, but for CFADs (%) of vertical velocity.....114

Figure 4.26 CFADs (%) of Z_H for EP2. (a),(c),(e) correspond to the SOP1 case, and (b),(d),(f) to the IOP3 case, with panels arranged by row as entire domain, convective, and stratiform precipitation regimes. The black line in each

doi:10.6342/NTU202504817

panel indicates mean profile. 115

Figure 4.27 As in Figure 4.26, but for CFADs (%) of Z_{DR}. 116

Figure 4.28 As in Figure 4.26, but for CFADs (%) of K_{DP}. 117

Figure 4.29 As in Figure 4.26, but for CFADs (%) of vertical velocity..... 118

Figure 4.30 Four-quadrant parameter space for EP1. (a),(c),(e) correspond to the SOP1 case, and (b),(d),(f) to the IOP3 case, with panels arranged by row as entire domain, convective, and stratiform precipitation regimes. In each panel, colored dots represent individual time points (UTC), and the red cross represents their average. The corresponding microphysical processes for every quadrant are also annotated. 119

Figure 4.31 As in Figure 4.30, but for EP2. 120

Figure 4.32 Time series of the mean separation distance between paired Z_{DR} and K_{DP} objects during EP1 of the IOP3 case over the entire analysis domain at 1.5-km height. 121

doi:10.6342/NTU202504817

Chapter 1 Introduction

1.1 Literature Review

East Asia, characterized by the most pronounced large-scale land-sea thermal contrast around the globe, is home to the largest monsoon region in the world. During late spring to early summer (from mid-May to mid-June or July), East Asia experiences a climatological rainfall maximum outside the summer typhoon season, referred to as “Meiyu” in China, “Baiu” in Japan, and “Changma” in Korea (Chen and Chang 1980; Chen et al. 1998; Zhou et al. 2004; Jeong et al. 2012; Hu et al. 2021). In this period, a quasi-stationary Meiyu front, oriented in the northeast-southwest or east-west direction and most pronounced at low levels, forms and extends from eastern China to southern Japan, driven by the gradual transition of the winter monsoon to the summer monsoon (Chen et al. 1998; Zhou et al. 2004).

In general, the Meiyu front is a belt-shaped zone of maximum cloudiness that corresponds to a long and narrow precipitation band along the northern boundary of the monsoon or tropical airmass (Akiyama 1973). Because the Meiyu front typically undergoes repeated development and decay, resulting in the successive formation of frontal cloud bands, the cloudiness zone can persist for several days to even a few weeks (Chen and Chang 1980; Hu et al. 2021). Moreover, frequent occurrences of convective cells and mesoscale convective systems (MCSs) within the Meiyu frontal cloud zone

doi:10.6342/NTU202504817

often lead to heavy rainfall and strong winds, causing flash floods and other related hazards in several East Asian countries, including Taiwan (Jeong et al. 2012; Wang et al. 2014; Chen et al. 2022; Cornejo et al. 2024; Hou et al. 2025).

From a synoptic perspective, the Meiyu front coincides with the early summer monsoon trough in East Asia, and its existence may be viewed as a manifestation of that trough (Chen 1983). For the Meiyu front over southeastern China, its temperature gradient is weak or nearly absent (i.e., weak baroclinicity), different from that of typical midlatitude fronts. Instead, it is characterized by a strong moisture contrast (i.e., a pronounced equivalent potential temperature gradient), an equivalent barotropic structure, and strong cyclonic wind shear in the lower troposphere (Akiyama 1973; Chen and Chang 1980; Chen 1983; Ninomiya 1984; Ding 1992; Hu et al. 2021). Hence, the Meiyu front also coincides with a low-level positive vorticity zone (Akiyama 1990).

Another key feature is a synoptic-scale supergeostrophic low-level jet (SLLJ) that frequently develops on the southern side (i.e., in the warm sector) of the Meiyu front, as the Indian monsoon extends eastward and further turns into southerlies over the South China Sea (Matsumoto et al. 1970; Matsumoto et al. 1971; Ding 1992; Chen et al. 1998). Typically, the SLLJ transports warm, moist air toward the Meiyu front, causing strong moisture convergence and creating a convectively unstable layer. This moist and unstable air can then be lifted by the front itself or by the terrain, which often leads to heavy rainfall

doi:10.6342/NTU202504817

(Chen 1983; Ding 1992; Chen et al. 2005; Tu et al. 2020; Chen et al. 2022). The orographic influences on low-level flow and extreme precipitation during the Meiyu season have been highlighted by Cornejo et al. (2024). In addition, the SLLJ can also induce a secondary circulation, with ascent occurring in the left-front quadrant of the jet axis (i.e., near the northern tip of the SLLJ) or in advance of the wind maximum, contributing to enhanced precipitation (Chen 1982; Chen et al. 1998).

Historically, the Meiyu front has long been a major topic in Taiwan's meteorological research. Two field campaigns, the Taiwan Area Mesoscale Experiment (TAMEX) in 1987 (Kuo and Chen 1990) and the Southwest Monsoon Experiment/Terrain-influenced Monsoon Rainfall Experiment (SoWMEX/TiMREX) in 2008 (Jou et al. 2011), have conducted comprehensive studies on Meiyu fronts. Building on these efforts, the most recent Taiwan-Area Heavy rain Observation and Prediction Experiment (TAHOPE) in 2022 (楊明仁等，2023) further extends this line of investigation (see Section 1.2).

In these field campaigns and other recent studies, high-resolution dual-polarization Doppler radars have played a crucial role in obtaining detailed insights into the kinematic, dynamical and microphysical processes of various weather systems. For instance, DeHart and Bell (2020) analyzed radar-observed variables, including particle identification (PID), radar reflectivity factor (Z_H), differential reflectivity (Z_{DR}), and specific differential phase (K_{DP}), for Hurricanes Harvey (2017) and Florence (2018) to compare their rainfall and

doi:10.6342/NTU202504817

polarimetric characteristics. The methodologies employed in their studies were likewise applied in our research. Moreover, Kumjian et al. (2022) reviewed the relationships between various cloud microphysical processes and the vertical gradients of polarimetric radar parameters, emphasizing that these gradients can act like “fingerprints” of ongoing microphysics (Figure 1.1 and Figure 1.2). Specifically, Figure 1.1 and Figure 1.2 depict the processes below and above the melting layer for liquid- and ice-phase precipitation, respectively, both excluding the influences of the bright band. Our study also applied this concept to generally infer dominant processes.

1.2 Overview of TAHOPE 2022

The Taiwan-Area Heavy rain Observation and Prediction Experiment (TAHOPE) was a major field campaign led by Taiwan, conducted in collaboration with the U.S. Prediction of Rainfall Extremes Campaign In the Pacific (PRECIP) and Japan’s Tropical cyclones-Pacific Asian Research Campaign for Improvement of Intensity estimations/forecasts (T-PARCII). Together, these three programs constituted a trilateral international joint field campaign, characterized by synergistic intensive observations.

TAHOPE primarily targeted severe weather events occurring over Taiwan and its surrounding areas, with a focus on Meiyu fronts, afternoon thunderstorms, tropical depressions, and typhoons. Owing to Taiwan’s moisture-rich environment, complex

doi:10.6342/NTU202504817

terrain with steep mountains, and dense operational observing network, the island serves as an excellent natural laboratory for investigating the mesoscale and small-scale processes associated with heavy rainfall events. With this international field campaign, researchers can not only gain a better understanding of the physical mechanisms underlying these severe weather events, but also evaluate the applicability of related scientific theories. Furthermore, critical parameters influencing forecast skill can be identified through data assimilation of the intensive observations. When these research outcomes are integrated into operational forecasting practices, they have the potential to further enhance the accuracy of numerical weather prediction, thereby mitigating the impacts of natural disasters on society, life, and property.

Due to the global outbreak of the COVID-19 pandemic, TAHOPE was postponed and ultimately conducted from 25 May to 10 August 2022. During this nearly three-month period, a total of eight Special Observation Periods (SOPs) and eleven Intensive Observation Periods (IOPs) were executed. Both SOPs and IOPs were associated with significant weather events; however, IOPs involved additional intensive observations, such as radiosonde launches beyond the routine schedule, while SOPs did not.

The schedule of each SOP and IOP, along with their corresponding dominant weather phenomena and observational targets, is summarized in Table 1.1. In brief, the early stage of the campaign (from late-May to mid-June) was dominated by Meiyu fronts

doi:10.6342/NTU202504817

and their accompanying MCSs. From mid-June onward, the campaign mainly focused on afternoon thunderstorms, occasionally influenced indirectly by typhoons (e.g., IOP6) and both directly and indirectly by tropical depressions (e.g., IOP8, IOP9, and IOP10).

1.3 Motivation

Despite the long history of Meiyu-front research in Taiwan (see Section 1.1), TAMEX lacked dual-polarization observations, and although SoWMEX employed a dual-polarization radar, it primarily focused on southern Taiwan. Consequently, detailed cloud microphysical analyses of the fronts over northern Taiwan remain limited.

Furthermore, in 2022, two Meiyu fronts affected Taiwan, observed respectively from SOP1 to IOP1 and subsequently during IOP3 of TAHOPE. Although both cases were associated with Meiyu fronts and the mean frontal positions were similar during certain periods, an inverse relationship between the frontal strength and the accumulated precipitation over northern Taiwan appeared: the weaker front was accompanied by heavier rainfall (details are provided in Chapter 3), which is worth further investigation.

Because TAHOPE targeted northern Taiwan with dual-polarization Doppler radar observations, we take advantage of this valuable opportunity to gain updated insights of Meiyu front cases in this region, combining cloud microphysical analyses with other evaluations. Building on the contrasting frontal strength and rainfall totals described

doi:10.6342/NTU202504817

above, this study will address the following three scientific questions:

(1) What were the similarities and differences between the two cases regarding their synoptic-scale and mesoscale features?

(2) Among these similarities and differences, which factors were crucial in driving the differences in precipitation features between the two cases?

(3) What were the underlying physical mechanisms responsible for the pronounced rainfall over northern Taiwan associated with the first Meiyu front case, specifically during 0700–1900 Z on May 25?

1.4 Thesis Organization

This thesis is organized into five chapters. Excluding the introduction, the remaining four chapters are organized as follows. Chapter 2 introduces the data and methods, including data sources, study area, definition of the Meiyu front, radar data preprocessing, interpretations of dual-polarization radar parameters, and the main analysis techniques applied in this study. Chapter 3 provides an overview of the two Meiyu front cases, highlighting their precipitation features over northern Taiwan. Chapter 4 presents the main results, covering analyses of synoptic conditions, thermodynamics, kinematics, and cloud microphysics. Chapter 5 summarizes the principal findings and outlines future research directions.

doi:10.6342/NTU202504817

Chapter 2 Data and Methods

2.1 Dataset Descriptions

2.1.1 Synoptic-Scale Analysis Data

For the two Meiyu front cases examined in this study, surface weather charts from the Japan Meteorological Agency (JMA) together with cloud imagery from the Himawari-8 geostationary satellite provide essential information on the synoptic-scale environment over East Asia and the orientation of the Meiyu fronts.

To further quantify the two Meiyu fronts and compare their thermodynamic (e.g., moisture) and kinematic (e.g., strength of low-level jets) characteristics at the synoptic scale, we additionally employed the ERA5 reanalysis data from the European Centre for Medium-Range Weather Forecasts (ECMWF) and the Morphed Integrated Microwave Imagery - Total Precipitable Water Version 2 (MIMIC-TPW2) product produced by the Cooperative Institute for Meteorological Satellite Studies (CIMSS) at the University of Wisconsin-Madison. Key attributes of the two dataset are summarized below.

(1) ERA5 Reanalysis Data

ERA5 is generated by the ECMWF Integrated Forecast System (IFS); during this process, a large collection of historical global observations are ingested into a four-dimensional variational (4D-Var) data assimilation framework to produce the best estimate of the atmospheric state at each analysis time and grid point, available

doi:10.6342/NTU202504817

from 1940 to present (Hersbach et al. 2020; Hersbach et al. 2023). The data are provided on a 0.25° × 0.25° latitude-longitude grid (approximately 27 km × 27 km) at hourly intervals. Additional ERA5 characteristics are listed in Table 2.1.

(2) MIMIC-TPW2

The MIMIC-TPW2 product combines microwave observations from multiple polar-orbiting satellites to produce globally gridded fields of total precipitable water (TPW) using a morphological compositing technique (Wimmers and Velden 2011). The data are provided on a 0.25° × 0.25° latitude-longitude grid (approximately 27 km × 27 km) at hourly intervals.

2.1.2 Surface Station and QPESUMS Data

To analyze the precipitation features associated with the two Meiyu front cases over northern Taiwan, hourly rainfall data from the 86 surface stations located in Taoyuan and the administrative regions to its north were utilized. The spatial distribution of these stations is shown in Figure 2.1. It is important to note that the hourly rainfall data herein represent rainfall accumulated over the preceding hour (e.g., the data at 08:00 represent the rainfall totals from 07:00 to 08:00).

Meanwhile, for precipitation over the surrounding oceanic areas, especially the northern Taiwan Strait, this study adopted the high-resolution Quantitative Precipitation

doi:10.6342/NTU202504817

Estimation and Segregation Using Multiple Sensors (QPESUMS) product, which was jointly developed by the Central Weather Bureau (CWB) of Taiwan and the U.S. National Severe Storms Laboratory (NSSL). QPESUMS integrates data from mixed-band weather radars, surface rain gauges, and numerical weather prediction model outputs to generate a high-resolution, rapid-update QPE product (Chang et al. 2021). The data are provided on a 0.0125° × 0.0125° latitude-longitude grid (approximately 1.4 km × 1.4 km) at 10-minute intervals. Other characteristics of the QPESUMS product are listed in Table 2.2.

It should also be noted that QPESUMS provides backward-accumulated hourly rainfall estimates at various time offsets (e.g., 07:10–08:10, etc.). In this study, only those ending at the top of the hour (e.g., 07:00–08:00, 08:00–09:00, etc.) are selected, in order to ensure temporal alignment and consistency with the hourly rain gauge observations.

2.1.3 Sounding and Radar Data

To investigate the mesoscale, convective-scale, and cloud microphysical features of the two cases, we utilized both routine and additional upper-air sounding data launched at Hsinchu, Banqiao (Taipei), and Pengchiayu. Moreover, observations from the S-Pol radar of the U.S. National Center for Atmospheric Research (NCAR), deployed at the Gang Nan Seaside Scenic Spot in Hsinchu, and from the Wufenshan (RCWF) as well as Shulin (RCSL) surveillance radars operated by CWB were also used. The locations of the

doi:10.6342/NTU202504817

aforementioned sounding and radar stations are shown in Figure 2.2; the basic specifications of the three radars are summarized in Table 2.3.

2.2 Study Area

For statistical analysis of the synoptic environment, the corresponding study area is illustrated in Figure 2.3. Specifically, the analysis of the barrier jet and integrated vapor transport (IVT) divergence focused on the vicinity of northern Taiwan (the red rectangle in Figure 2.3), while other thermodynamic and kinematic parameters were analyzed over the northern South China Sea (the blue rectangle in Figure 2.3). This region is identical to that used in Tu et al. (2020), which investigated the relationship between moisture transport associated with the marine boundary layer jet (MBLJ) and heavy rainfall events during the Meiyu season in Taiwan.

For the analysis of cloud microphysics, the study area was restricted to the land area in northern Taiwan located approximately 40 to 80 km north of the S-Pol radar, as illustrated in Figure 2.4. This choice corresponded to the region with the most pronounced difference in accumulated rainfall between the two cases and also ensured a sufficient number of reliable samples based on the following two considerations. First, the plan position indicator (PPI) scanning strategy of radars forms a cone-shaped scanning volume that leads to data scarcity at upper levels near the radars and lower levels farther from

doi:10.6342/NTU202504817

them. Second, the accuracy of polarimetric parameters deteriorates with increasing distance from the radars, primarily due to radar signal attenuation, beam broadening, and nonuniform beam filling (NBF) (Ryzhkov 2007; Gorgucci and Baldini 2015).

2.3 Definition of the Meiyu Front

As reviewed in Chapter 1, Meiyu fronts over southeastern China and in the vicinity of Taiwan are characterized by two prominent features: a pronounced horizontal gradient of equivalent potential temperature (θ_e) and significant horizontal cyclonic wind shear. Building on this understanding, Hu et al. (2021) established specific quantitative thresholds for these two characteristics based on Meiyu fronts situated near 30°N. These objective criteria allow the identification of Meiyu fronts to move beyond conventional subjective approaches, enabling more consistent and reproducible analyses.

Hence, we adopted the thresholds proposed by Hu et al. (2021), with appropriate modifications to better match our study area and research purposes. A mature Meiyu front was herein defined as a region that simultaneously satisfied the following three conditions:

(1) Satellite imagery must show the region as a zone of maximum cloud coverage associated with the Meiyu frontal cloud band.

(2) On the 975-hPa pressure level, the region must exhibit a banded structure with a horizontal θ_e gradient exceeding 80 K/1000 km, oriented in a northeast-southwest or

doi:10.6342/NTU202504817

east-west direction.

(3) On the 975-hPa pressure level, the region must also feature relative vorticity exceeding 5×10^{-5} s^{-1}, indicating stronger low-level cyclonic wind shear.

Regarding Condition (2), due to potential vorticity conservation, the cold-air layer behind the Meiyu front tends to become shallower as it moves southward, making frontal characteristics near Taiwan primarily manifest at lower levels. To better capture the influence of near-surface fronts while reducing surface-related interference, the 975-hPa pressure level was selected. Additionally, Meiyu fronts in this region may not always exhibit θ_e gradients as strong as those in Hu et al. (2021), which adopted a threshold of 100 K/1000 km; therefore, the θ_e gradient threshold was slightly relaxed to 80 K/1000 km to better capture their continuous, banded structure.

As for Condition (3), the threshold of 5×10^{-5} s^{-1} for relative vorticity was chosen because it is roughly comparable to the order of planetary vorticity over Taiwan, ensuring that relative vorticity meaningfully contributes to absolute vorticity rather than being overshadowed by the planetary vorticity (i.e., the Coriolis effect).

To illustrate the Meiyu front definition adopted here, an example from 0300 Z on June 6, 2022, is shown in Figure 2.5. At this time, only the region enclosed by the two black lines meets all criteria and is thus identified as the Meiyu front.

doi:10.6342/NTU202504817

2.4 Radar Data Preprocessing

In general, radar data must undergo a quality control (QC) procedure to ensure high quality before use. The S-Pol radar data had already gone through comprehensive QC conducted by the Earth Observing Laboratory (EOL) of NCAR and the Radar Meteorology Group at Colorado State University, while the RCWF and RCSL radar data had undergone basic QC by CWB.

Because the overall quality of the radar data was already acceptable, only several additional preprocessing steps were applied in this study. These included (1) removing grid points with a correlation coefficient (ρ_{HV}) less than 0.85 or a spectrum width greater than 5 m/s; (2) removing abnormal radial winds in the Wufenshan and Shulin radar data associated with aircraft takeoffs and landings at Taipei Songshan Airport; and (3) removing abnormal radial winds in the S-Pol radar data within the azimuth range of 26.25° to 30.75° for the four elevation angles (0.5°, 1.0°, 1.5°, and 2.0°).

Additionally, a manual inspection confirmed that no velocity aliasing was present in the radial wind fields of the three radars. Hence, a dealiasing procedure was not required.

2.5 3D Wind Retrieval

To compare the mesoscale and convective-scale kinematic features of the two cases, the complete three-dimensional wind field was recovered through multiple-Doppler

doi:10.6342/NTU202504817

synthesis based on PPI observations from the S-Pol, RCWF, and RCSL radars.

In this study, we adopted the Spline Analysis at Mesoscale Utilizing Radar and Aircraft Instrumentation (SAMURAI) software (Bell et al. 2012), specifically the SAMURAI-TERRAIN version (Cha and Bell 2023), with the horizontal and vertical node spacing set to 1 km and 0.5 km, respectively. Furthermore, the retrieval domain covered a 140 km × 140 km area encompassing northern Taiwan and adjacent offshore region, and extended vertically from the surface up to 17 km in altitude.

SAMURAI-TERRAIN is a wind retrieval software based on three-dimensional variational data assimilation (3DVAR) techniques. It can assimilate actual radial velocity observations from radar along with other data sources (e.g., dropsondes, satellite vector winds, and model or reanalysis data), while simultaneously incorporating specified error estimates for each data type, and applying the anelastic mass continuity equation as an additional physical weak constraint. Finally, through an iterative process with the conjugate gradient method, the cost function is minimized to objectively produce a maximum likelihood estimate of the three-dimensional wind field at each time (Bell et al. 2012; Foerster et al. 2014; Cha and Bell 2023).

2.6 Interpretations of Dual-Polarization Radar Parameters

Dual-polarization Doppler radars can transmit both horizontally and vertically

doi:10.6342/NTU202504817

polarized electromagnetic waves simultaneously. Compared to traditional single-polarization Doppler radars, they can provide additional information on the size, shape, and type of hydrometeors, particularly valuable for analyses related to cloud microphysics. In this study, three dual-polarization radar parameters were utilized, as described below:

(1) Radar Reflectivity Factor (Z_H and Z_V)

As radar-transmitted electromagnetic waves propagate outward, they may encounter hydrometeors (e.g., raindrops, hailstones) or other targets (e.g., terrain, insects), resulting in backscattering. The strength of the scattered energy returned to the radar is called the radar reflectivity factor, commonly known as radar echo. For dual-polarization radars, when the polarization direction of both transmitted and received waves is horizontal, the received signal is termed the horizontal reflectivity factor (Z_H). Conversely, when both directions are vertical, the corresponding signal is known as the vertical reflectivity factor (Z_V).

Under the Rayleigh approximation and assuming the hydrometeors are perfect spheres, the radar reflectivity factor simply corresponds to the sixth moment of the particle size distribution, with units of mm^6/m^3 (often converted to dB*Z*) (Seliga and Bringi 1976):

$$Z = \int_0^\infty D^6 N(D) dD \tag{2.1}$$

However, in practice, as hydrometeors grow larger, their shapes gradually deviate

doi:10.6342/NTU202504817

from spheres and become oblate spheroids. This change results in different scattering cross-sections in the horizontal and vertical directions, leading to differences in horizontal and vertical reflectivity factors, as represented by the following equations (Seliga and Bringi 1976):

$$Z_H = \int_0^\infty {D_{eq}}^6 \left| \frac{m^2 - 1}{4\pi + (m^2 - 1)P'} \right|^2 N(D_{eq}) dD_{eq} \tag{2.2}$$

$$Z_V = \int_0^\infty {D_{eq}}^6 \left| \frac{m^2 - 1}{4\pi + (m^2 - 1)P} \right|^2 N(D_{eq}) dD_{eq} \tag{2.3}$$

Here, D_{eq} denotes the equivolume diameter of hydrometeors, and m is the complex index of refraction for water-phase particles. Furthermore, P and P' represent geometrical factors. Detailed descriptions of these variables can be found in Seliga and Bringi (1976). As indicated by the above equations, the radar reflectivity factor is proportional to the sixth power of the hydrometeor diameter. Therefore, as the size of hydrometeor increases, the reflectivity factor increases significantly. In addition, a greater number of hydrometeors also contributes to higher reflectivity; however, the effect of particle size is generally more dominant.

(2) Differential Reflectivity (Z_{DR})

The differential reflectivity (Z_{DR}) is defined as the logarithmic ratio of the horizontal to vertical reflectivity factors and can be expressed by the following equation, with units in decibels (dB) (Seliga and Bringi 1976; Houze 2014):

doi:10.6342/NTU202504817

$$Z_{DR} = 10 \log_{10} \left(\frac{Z_H}{Z_V} \right) \quad (2.4)$$

As hydrometeors grow larger and their shapes become more oblate, Z_H increases due to the enlarged horizontal scattering cross-section, while Z_V decreases because of the reduced vertical scattering cross-section. This leads to a continuous increase in the ratio of Z_H to Z_V, resulting in a larger Z_{DR}. Thus, Z_{DR} is related to the size of hydrometeors, increasing as particle size grows and decreasing as it diminishes.

Generally, raindrops exhibit Z_{DR} values ranging from approximately 0 to 5 dB. Large aggregate snowflakes also tend to have relatively higher Z_{DR} values. However, due to continuous spinning and tumbling motions during descent, hailstones often lack a preferred orientation, causing the mean values of Z_H and Z_V to become similar and resulting in Z_{DR} values typically close to zero (Houze 2014). The relationship between hydrometeor size and Z_{DR} values is depicted in Figure 2.6.

(3) Specific Differential Phase (K_{DP})

As radar-transmitted electromagnetic waves propagate through hydrometeors suspended in the atmosphere, each particle experiences two primary sources of incident waves: (1) the direct wave emitted by the radar itself, and (2) the forward-scattered waves produced by other hydrometeors located between the radar and the target particle. The superposition of these two components results in a net electric field that is phase-shifted relative to that originally transmitted, a phenomenon

doi:10.6342/NTU202504817

referred to as propagation phase shift (Jameson and Mueller 1985).

If hydrometeors are non-spherical, the phase shift experienced by the horizontally polarized wave (ϕ_H) differs from that of the vertically polarized wave (ϕ_V). The difference between the two is defined as the differential phase (ϕ_{DP}), which is measured in degrees (°) (Houze 2014):

$$\phi_{DP} = \phi_H - \phi_V \tag{2.5}$$

The derivative of differential phase with respect to range is known as the specific differential phase (K_{DP}), with units in degrees per kilometer (°/km) (Houze 2014):

$$K_{DP} = \frac{d\phi_{DP}}{dr} = \frac{d}{dr}(\phi_H - \phi_V) \tag{2.6}$$

According to Bringi and Chandrasekar (2001), under the assumption of Rayleigh approximation, K_{DP} can be further expressed in the following more complex form:

$$K_{DP} = \frac{\pi k_0}{12} Re\left\{\int D^3 N(D)\left[\frac{\varepsilon_r - 1}{1 + \frac{1}{2}(1-\lambda_z)(\varepsilon_r - 1)} - \frac{\varepsilon_r - 1}{1 + \lambda_z(\varepsilon_r - 1)}\right] dD\right\} \tag{2.7}$$

In this expression, k_0 denotes the wavenumber in vacuum, ε_r represents the dielectric constant of water-phase hydrometeors, and λ_z is a parameter related to the axis ratio of hydrometeors. Detailed descriptions of these variables can be found in Bringi and Chandrasekar (2001). As shown in Eq. (2.7), the expression for K_{DP} involves the third moment of the drop size distribution. Since this moment is associated with the total volume of precipitation particles, K_{DP} values can serve as a

doi:10.6342/NTU202504817

proxy for the liquid water content within the sampled volume. In summary, K_{DP} is related to the liquid water content, increasing as the amount of liquid water grows and decreasing as it diminishes.

For hail and other ice particles, K_{DP} values typically range from near 0 °/km for drier particles to approximately 1 °/km for wetter particles. In contrast, raindrops exhibit a wider dynamic range of K_{DP}, spanning from 0 up to 7 °/km (Houze 2014).

2.7 Convective-Stratiform Separation Algorithm

Given the substantial differences between convective and stratiform precipitation regimes, such as the organization of the cloud systems, vertical motion, precipitation growth mechanisms, and the vertical structure of diabatic heating, it is essential to distinguish between the two in cloud microphysical analyses. To this end, this study adopted a convective-stratiform separation algorithm (Steiner et al. 1995; Yuter and Houze 1997; Didlake and Houze 2009; Wu et al. 2022), which classifies precipitation regimes based on the horizontal structure of radar reflectivity, including its intensity and gradient. The detailed procedures are described as follows:

(1) Identify convective centers

A grid point at 2-km height in the gridded S-Pol radar data was directly regarded as a convective center if its reflectivity exceeded 42 dB*Z* (i.e., sufficiently strong

doi:10.6342/NTU202504817

echoes). In addition, a grid point with reflectivity below 42 dBZ could also be classified as a convective center if the difference between its reflectivity and the background reflectivity (Z_{bg}) exceeded a predefined convective center criterion (ΔZ_{cc}) (i.e., sufficiently sharp horizontal reflectivity gradient).

Here, Z_{bg} is defined as the mean reflectivity of all nonzero values within an 11-km radius surrounding each grid point, and ΔZ_{cc} is given by the following equation (Yuter and Houze 1997):

$$\Delta Z_{cc} = a\cos\left(\frac{1}{b}\frac{\pi Z_{bg}}{2}\right) \tag{2.8}$$

The coefficients a and b in Eq. (2.8) are adjustable parameters, depending on the targeted weather system (e.g., typhoons, Meiyu fronts, afternoon thunderstorms) and the radar instrumentation used. In this study, we adopted the settings of $a = 9$ and $b = 45$ originally proposed by Didlake and Houze (2009), and subsequently utilized by Wu et al. (2022). Although both studies focused on typhoons rather than the Meiyu front, applying these values still yielded reasonable results (as discussed later). Therefore, no further adjustments were made.

In summary, in this step, any grid point at 2-km height with reflectivity exceeding 42 dBZ or exceeding $Z_{bg} + \Delta Z_{cc}$ was classified as a convective center.

(2) Expand convective precipitation regimes

For all grid points identified as convective centers in the first step, a

doi:10.6342/NTU202504817

corresponding convective radius (R) was assigned based on the background reflectivity value at each point. Subsequently, each convective center served as the origin of a circular area with radius R, within which all enclosed grid points were also classified as part of the convective precipitation regimes.

Here, R was defined by a piecewise function depending on the magnitude of the background reflectivity (Didlake and Houze 2009):

$$R = \begin{cases} 0.5, & Z_{bg} < 20 \\ 0.5 + 3.5\left(\dfrac{Z_{bg} - 20}{15}\right), & 20 \le Z_{bg} < 35 \\ 4, & Z_{bg} \ge 35 \end{cases} \tag{2.9}$$

By doing so, the convective precipitation regimes were identified as horizontally contiguous areas at 2-km height.

(3) Classify convective precipitation subtypes and label other regimes

For all grid points classified as convective precipitation regimes in the second step, further subclassification was performed based on the height of 20-dBZ echo top, with points classified as deep convection (DC), moderate convection (MC), or shallow convection (SC) when the echo top exceeded 10 km, was between 4 and 10 km, or was less than 4 km, respectively (Tao and Jiang 2015; Fritz et al. 2016; Rogers et al. 2020; Wu et al. 2022).

Additionally, grid points in non-convective precipitation regimes were classified as stratiform (ST), weak-echo (WE), or no-echo (NE) regions when

doi:10.6342/NTU202504817

reflectivity at 2-km height exceeded 20 dB*Z*, was less than 20 dB*Z*, or was zero/missing (NaN), respectively (Wu et al. 2022).

The aforementioned classification criteria are summarized in Table 2.4, and the spatial relationship among a convective center, its background region, and the resulting convective precipitation regime is shown in Figure 2.7. Moreover, manual inspection confirmed that the results were generally reasonable (Figure 2.8), supporting the algorithm's suitability for subsequent cloud microphysical analyses.

2.8 Methods for Identifying Low-Level Size Sorting Signature

An object-based identification method (Loeffler and Kumjian 2018; Loeffler et al. 2020; Tam et al. 2022) was applied to quantitatively assess the size sorting signature, with the separation distance between regions of enhanced Z_{DR} and K_{DP} serving as a proxy for the significance of size sorting (a larger separation distance indicates a more evident size sorting, and vice versa; see Section 4.4.6 for details). The procedure can be roughly divided into the following four steps:

(1) Identify Z_{DR} and K_{DP} objects

Using gridded S-Pol radar data at 1.5-km height, contiguous regions of enhanced Z_{DR} and K_{DP} values (hereafter referred to as Z_{DR} objects and K_{DP} objects,

doi:10.6342/NTU202504817

respectively) were identified. Specifically, Z_{DR} and K_{DP} objects were defined as contiguous regions where their values exceeded the magnitude thresholds corresponding to the 97th and 93rd percentiles, respectively, across all grid points at 1.5-km height.

It is worth noting that, because the beam of S-Pol radar at its lowest elevation angle (i.e., 0.5°) typically intersected our study area at approximately 1 to 1.5 km above ground, the 1.5-km level was chosen to ensure the reliability of the observed data for subsequent analysis.

(2) Remove small Z_{DR} and K_{DP} objects

In the first step, Z_{DR} and K_{DP} objects were identified based on magnitude thresholds; however, this approach may include some objects with excessively small areas. To enhance the representativeness, objects below specified size thresholds were further excluded from subsequent analysis. Specifically, any Z_{DR} or K_{DP} object with an area smaller than the 80th and 75th percentiles, respectively, of all corresponding objects at 1.5-km height was considered too small and thereby discarded.

(3) Calculate the centroid coordinates of Z_{DR} and K_{DP} objects

The centroids of each Z_{DR} and K_{DP} object passing the aforementioned threshold filters were calculated and recorded in this procedure, with each centroid defined as

doi:10.6342/NTU202504817

the mean latitude and longitude of all grid points within the object.

(4) Match Z_{DR} and K_{DP} objects and calculate separation distance

In this step, we first employed a mutual nearest-neighbor pairing strategy, such that a pair was considered valid only if a Z_{DR} object was the nearest neighbor of a K_{DP} object and, simultaneously, that K_{DP} object was also the nearest neighbor of the same Z_{DR} object. This approach differs slightly from that used by Tam et al. (2022) and other previous research (Loeffler and Kumjian 2018; Loeffler et al. 2020) because their analyses primarily focused on the separation distance between Z_{DR} and K_{DP} objects in intense convective systems (e.g., squall lines, supercell tornadoes, and non-supercell tornadoes), whereas the case analyzed in our study did not belong to such systems, making the regions of enhanced Z_{DR} and K_{DP} more dispersed and less pronounced. To avoid erroneous pairings, we therefore adopted this strategy.

After the Z_{DR} and K_{DP} objects were paired, the geometrical distance between the centroids of each pair was calculated. Only those with separation distances less than 15 km were retained to minimize erroneous pairings. In addition, all pairings were manually inspected to eliminate any clearly incorrect or unreasonable matches (as shown in Figure 2.9), thereby ensuring the accuracy of the analysis.

doi:10.6342/NTU202504817

Chapter 3 Case Overview

3.1 Overall Precipitation Features

As noted in Section 1.3, both the SOP1 to IOP1 and IOP3 of TAHOPE correspond to periods when Taiwan was under the influence of Meiyu fronts. Based on the daily accumulated rainfall maps (in LST) from CWB, the primary precipitation hotspot during the Meiyu frontal events from SOP1 to IOP1 was concentrated over the central-to-northern part of Taiwan, while secondary hotspots varied in location with date, occurring either over the coastal plains (5/26) or in mountainous regions (5/25 and 5/27) of the southern part of Taiwan, as shown in Figure 3.1a–d. Since both the S-Pol radar observations and the additional radiosonde launches of TAHOPE were conducted in and north of Hsinchu, this study only focuses on the precipitation features over northern Taiwan. Within this domain, the most pronounced rainfall occurred on 5/25 (SOP1), when daily accumulated rainfall exceeded 150 mm across the coastal areas of Taoyuan City and New Taipei City, with amounts over 130 mm also observed in the mountainous regions of Taipei City (Figure 3.1a).

As for IOP3, although it was the longest-lasting IOP within TAHOPE, spanning approximately six days, the precipitation over Taiwan was primarily concentrated in the first three days, with the most pronounced rainfall again occurring over the central-to-northern region. Hence, the later periods are excluded from further discussion in this study.

doi:10.6342/NTU202504817

Compared to IOP1, the total precipitation over northern Taiwan during this period was significantly less, with daily accumulated rainfall generally below 90 mm (Figure 3.2a–d).

To further quantitatively compare the precipitation features of the two periods, with all times expressed in UTC, the station-averaged hourly rainfall at each time point was calculated using data from the 86 surface stations in and north of Taoyuan. This approach was employed to depict the mean hourly accumulated precipitation variations associated with the two Meiyu fronts over northern Taiwan. Consistent with the general perception of the Meiyu season, northern Taiwan experienced multiple precipitation episodes of varying amounts, with the most prominent peaks in mean hourly accumulated rainfall occurring on 5/25 (exceeding 16 mm) and 6/07 (approximately 13 mm) (Figure 3.3a, b). The physical mechanisms underlying the latter case have been comprehensively investigated in the previous study (Yang et al. 2024).

3.2 Overall Comparison of the Two Selected Periods

Building on the overall precipitation features of the two Meiyu front events during TAHOPE 2022, this study specifically focused on two 12-hour periods, 0700–1900 Z on 5/25 (defined as the SOP1 case) and 6/06 (defined as the IOP3 case) (black boxes in Figure 3.3a, b). For analyses in subsequent sections, each case was further divided into

doi:10.6342/NTU202504817

two episodes of enhanced surface precipitation, hereafter referred to as Episode 1 (EP1) and Episode 2 (EP2), as indicated by the color-shaded periods in Figure 3.3c, d.

In the two cases, the average positions of the Meiyu fronts at 975 hPa over the Taiwan Strait were nearly identical, differing by less than 50 km (Figure 3.4a, b). While the average position cannot capture the instantaneous state of the front, which may also affect precipitation, the synoptic-scale and cloud microphysical analyses in this study applied temporal averaging over several hours and spatial averaging over areas spanning several tens of kilometers; therefore, minor differences in frontal position can be neglected. Meanwhile, Figure 3.4a and Figure 3.4b also show a clear contrast in the structure and intensity (i.e., $\nabla\theta_e$) of the two fronts: the front in the SOP1 case had a loose, weaker structure, whereas that in the IOP3 case was more organized and stronger.

However, the two cases exhibited a striking inverse relationship between frontal strength and rainfall totals over northern Taiwan. The mean 12-hour accumulated rainfall over the 86 surface stations in and north of Taoyuan was only 28.18 mm for the IOP3 case and up to 95.55 mm for the SOP1 case (i.e., about 3.4 times as much as that for IOP3). In addition, the maximum accumulation for the SOP1 case approached nearly 200 mm, roughly three times as high as that for the IOP3 case (Figure 3.5).

Further analysis from QPESUMS data revealed that the most significant differences in spatial distribution of 12-hour rainfall totals were concentrated in northern Taiwan: in

doi:10.6342/NTU202504817

the SOP1 case, the precipitation extended from over the Taiwan Strait toward the coastal areas in and north of Taoyuan, where accumulation maxima of 150–200 mm were observed. By contrast, in the IOP3 case, the accumulation in the same coastal region was only 30–50 mm, with precipitation mainly distributed over the Taiwan Strait (Figure 3.6a, b). These features of precipitation distribution were also evident in the Hovmöller diagrams along the east-west cross-section at 25°N (Figure 3.7a, b), and a similar pattern was likewise revealed by the Global Precipitation Measurement (GPM) satellite observations (figures not shown).

It should be emphasized that the scientific objective of this study, as mentioned earlier, is to investigate why two Meiyu front cases with similar mean frontal positions produced markedly different rainfall totals over northern Taiwan. For this reason, the offshore rainfall maximum on 6/06 is excluded from the selected cases. The event on 6/07 is also excluded because the frontal position at that time had already changed. In the next chapter, a more detailed examination of the two cases will be provided.

doi:10.6342/NTU202504817

Chapter 4 Analysis Results

4.1 Synoptic Insights

In this section, we examine whether differences in the synoptic environment between the SOP1 and IOP3 cases can account for the pronounced contrast in their rainfall totals. According to JMA surface weather charts, the Meiyu front was already located over northern Taiwan at the start of SOP1 (5/25 0000 Z). From 0600 Z to 1800 Z on the same day, the front exhibited a slight northward retreat toward the offshore region, but overall, it remained close to northern Taiwan throughout this period (Figure 4.1a–d). As for IOP3, the Meiyu front was still located over the East China Sea, several hundred kilometers away from Taiwan at 6/06 0000 Z. During the subsequent 18 hours, the front rapidly shifted southward and lingered over northern to central Taiwan (Figure 4.2a–d). It is worth noting that because these charts were manually analyzed and somewhat subjective, this study still mainly relied on ERA5 reanalysis data to determine the mean frontal positions, as discussed in Section 3.2.

After examining the evolution of the surface Meiyu fronts, we next assessed the corresponding mid- to upper-level synoptic conditions. The 12-hour averaged weather charts at 700 hPa, 500 hPa, and 200 hPa revealed that Taiwan was neither influenced by any significant mid- to upper-level trough-ridge systems nor located near the right entrance region of the upper-level jet stream in both the SOP1 (Figure 4.3a–c) and IOP3

doi:10.6342/NTU202504817

(Figure 4.4a–c) cases. Therefore, the forcing responsible for their differences in precipitation features may primarily originate from the lower troposphere.

In addition to the synoptic conditions discussed above, the rainfall associated with the Meiyu front may also be influenced by its baroclinicity, slope, and intensity. Since the Meiyu fronts in both cases exhibited an approximately east-west orientation over the Taiwan Strait, a north-south cross section at 121°E, extending from 24°N to 28°N (as indicated by the red line in Figure 4.5), was selected to clearly depict the complete frontal structure as well as the prefrontal environment, thereby allowing an assessment of how the slope and baroclinicity of the two fronts may affect their rainfall.

As mentioned in Section 1.1, the most pronounced differences on either side of the Meiyu front are primarily manifested in the equivalent potential temperature (θ_e) field; therefore, using vertical cross sections of θ_e is most appropriate when comparing frontal slopes between different cases. The vertical profiles of θ_e revealed that the frontal slope in the SOP1 case was generally gentle, and accordingly, the associated vertical motion was relatively weak. Nevertheless, its ascending flow covered a broader area along the sloping frontal zone and persisted for a longer period, which may have contributed to the greater accumulated rainfall in this case (Figure 4.6a–c). In contrast, the frontal slope in the IOP3 case was considerably steeper at the beginning, accompanied by more pronounced vertical motion, with clear upward transport of high-θ_e air from the boundary

doi:10.6342/NTU202504817

layer and lower troposphere, though confined to a much narrower region. Meanwhile, as the front gradually weakened over time (i.e., frontolysis, characterized by a weakening of the horizontal θ_e gradient), these features also progressively diminished and may have been unfavorable for the occurrence of substantial rainfall totals (Figure 4.7a–c).

When viewed from the perspective of vertical profiles of potential temperature (θ), signals similar to those identified in the θ_e cross sections can also be observed. Specifically, in the SOP1 case, the cold air behind the front was relatively shallow, mainly confined below the 900-hPa level (as inferred from the tilt or "jump" of the isentropes). In addition, the isentropes were more widely spaced in the north-south direction, indicating a relatively weak horizontal θ gradient along this axis and, therefore, weak overall baroclinicity (Figure 4.8a–c), consistent with the findings of Chen and Chang (1980). By contrast, during the early stage of the IOP3 case, the cold air layer was somewhat deeper, roughly extending upward to the 850-hPa level. Moreover, the isentropes were more closely packed in the north-south direction, suggesting a stronger horizontal θ gradient and thus stronger baroclinicity compared to the SOP1 case. However, as time progressed, the cold air layer behind the front in the IOP3 case gradually became shallower, and the horizontal θ gradient along the north-south axis also noticeably weakened, leading to a reduction in baroclinicity (Figure 4.9a–c). Nevertheless, the baroclinicity of the IOP3 case remained quite weak compared to that of typical

doi:10.6342/NTU202504817

midlatitude fronts even during its strongest period.

Aside from the qualitative analysis based on vertical cross sections, this study also quantitatively compared the slope and intensity of the Meiyu fronts for the two cases. At each time step, the regionally averaged frontal slope and intensity at the 975-hPa level were calculated over grid points within 119.5−122°E and 24−26.5°N that satisfied the criteria for a mature Meiyu front proposed in Section 2.3. Specifically, the horizontal θ_e gradient was used to characterize frontal intensity, whereas the frontal slope was obtained from the Margules formula:

$$\tan \phi_i = \frac{f\bar{T}}{g}\frac{\Delta U}{\Delta T} \tag{4.1}$$

Here, ϕ_i is the tilting angle of the front, f is the Coriolis parameter, $\bar{T}$ is the mean temperature across the frontal zone, g is the gravitational acceleration, while ΔU and ΔT represent the horizontal wind differences and temperature contrasts between the warm and cold air masses (defined as warm minus cold), respectively. Compared to the SOP1 case, the Meiyu front in the IOP3 case was consistently steeper (Figure 4.10a), with the initially distinct slope primarily resulting from the large horizontal wind differences across the front due to a pronounced low-level jet in the warm sector, theoretically providing a stronger lifting mechanism. Additionally, although the Meiyu front in the IOP3 case gradually weakened over time (i.e., frontolysis), it remained much more intense than that of the SOP1 case throughout the selected period (Figure 4.10b),

doi:10.6342/NTU202504817

consistent with the previous discussion.

After comparing the frontal slope and intensity between the two cases, this study conducted statistical analyses of other ERA5 variables as well as the TPW derived from satellite observations (spatial domain defined in Section 2.2). Since both Meiyu fronts were confined to the lower troposphere, with minimal influence from mid- to upper-level trough-ridge systems, the analysis primarily focused on the lower to middle troposphere. For clarity of interpretation, the results were organized into three aspects (kinematics, thermodynamics, and moisture transport) and summarized in Table 4.1.

With regard to the kinematic aspect, the statistical analysis of wind speeds at different levels showed that the synoptic winds in the IOP3 case were generally stronger than those in the SOP1 case. However, the relative strength exhibited a pronounced decrease over time, particularly at the 900-hPa level, indicating a rapid weakening of the wind speeds in the IOP3 case, consistent with the concurrent frontolysis.

With regard to the thermodynamic aspect, the statistical analysis of specific humidity at different levels and the TPW indicated that the synoptic moisture in the SOP1 case was generally higher than that in the IOP3 case. Moreover, since the values of relative strength exhibited little temporal variation, the difference in atmospheric moisture content between the two cases remained nearly constant. This suggests that, at the synoptic scale, neither case experienced any abrupt decline in moisture.

doi:10.6342/NTU202504817

Finally, in terms of moisture transport, the statistical analysis revealed that both the upstream moisture transport and local moisture flux convergence around northern Taiwan were generally stronger in the IOP3 case than in the SOP1 case. However, the initially stronger upstream moisture transport in the IOP3 case, particularly within the 900–1000 hPa (i.e., boundary layer), was primarily attributable to stronger wind speeds. Given that no sudden decrease in atmospheric moisture content was identified in either case, the weakening of moisture transport in the IOP3 case later on was mainly governed by the reduction in wind speeds. As for the local moisture flux convergence in the IOP3 case, the significant increase over time primarily reflected the approach of the Meiyu front. If calculated relative to the moving front itself, the flux convergence would still diminish substantially due to frontolysis.

In summary, at the synoptic scale, the IOP3 case exhibited advantages in frontal slope, frontal intensity, the kinematic fields, and moisture transport. However, the accumulated rainfall over northern Taiwan remained quite limited. Conversely, although the SOP1 case performed less favorably in the aforementioned aspects and was relatively stronger only in the thermodynamic fields, considerable rainfall totals over northern Taiwan were still observed. These findings suggest that frontal structure and intensity are not necessarily positively correlated with the resulting total precipitation. Instead, factors such as moisture content, local atmospheric instability, and mesoscale, convective-scale,

doi:10.6342/NTU202504817

or cloud microphysical processes appeared to play a more decisive role in controlling the ultimate accumulated rainfall during the frontal passages.

4.2 Thermodynamic Insights

Building on the synoptic-scale comparison, sounding data were further employed to examine differences in the vertical thermodynamic structures between the SOP1 and IOP3 cases. Because the most distinct differences in precipitation features occurred over northern Taiwan, especially in the coastal areas of Taoyuan City and New Taipei City (see Section 3.1 and Section 3.2), soundings from Banqiao station were first analyzed (the results shown subsequently were also consistent with those from other sounding stations and times).

Prior to the beginning of the two cases, i.e., 5/25 0000 Z (SOP1 case) and 6/06 0000 Z (IOP3 case), the following two findings can be summarized:

(1) In the SOP1 case (Figure 4.11a), a shallow frontal inversion was present around the 950-hPa level, with north-northwest winds below and southwest to west winds above, indicating that Banqiao station was situated behind the surface Meiyu front. The cold air layer behind the front was relatively shallow, in agreement with the previous synoptic analysis. Moreover, the atmosphere was highly moist (with a total precipitable water of 66.1 mm) and exhibited a moist-neutral structure, primarily

doi:10.6342/NTU202504817

because the Meiyu front had lingered near Taiwan for about one day.

(2) In the IOP3 case (Figure 4.11b), Banqiao station was still within the warm sector ahead of the Meiyu front. The mid-to-lower troposphere below the 500-hPa level was dominated by strong southwesterly winds of 10−20 m s^{-1}, consistent with both the ERA5 reanalysis and the wind profiler observations at Xinwu, Taoyuan (figures not shown). Under such conditions, northern Taiwan was influenced by downslope subsidence, which may account for the pronounced inversion observed near the 900-hPa level. Consequently, the atmosphere was relatively dry, with a total precipitable water of 52.6 mm, lower than that in the SOP1 case. Meanwhile, distinct dry layers were evident in both the middle (400−500 hPa) and lower (below 700 hPa) troposphere. The signal of the latter persisted at least until 0600 Z (figures not shown), after which the atmosphere gradually moistened.

Subsequently, at 1200 Z for the two cases, i.e., 5/25 1200 Z (SOP1 case) and 6/06 1200 Z (IOP3 case), the following two characteristics can be further identified:

(1) In the SOP1 case (Figure 4.12a), the low-level flow was dominated by northeasterlies, indicating that Banqiao station remained in the postfrontal environment. Meanwhile, the mid- to lower-troposphere was still characterized by high moisture content and a moist-neutral state, similar to that at 0000 Z.

doi:10.6342/NTU202504817

(2) In the IOP3 case (Figure 4.12b), the low-level winds shifted to west-northwesterlies, indicating that Banqiao station was also situated in the postfrontal environment. Meanwhile, the previously strong southwesterly flow below the 500-hPa level weakened, consistent with the trends suggested by the ERA5 reanalysis and the wind profiler observations at Xinwu (figures not shown), thereby diminishing the signal of subsidence inversion. With the subsidence weakening and precipitation already occurring, the dry layer below the 700-hPa level present at 0000 Z gradually moistened, resulting in the total precipitable water comparable to that in the SOP1 case.

To further examine the moistening process of the mid-to-lower troposphere below the 500-hPa level in the IOP3 case, we analyzed the temporal evolution of the difference between the saturation equivalent potential temperature (θ_{es}) and the equivalent potential temperature (θ_e), hereafter referred to as the saturation deficit (in units of Kelvin), at various pressure levels. A saturation deficit of zero indicates that the atmosphere is exactly saturated, whereas a positive value denotes an unsaturated state, with larger values corresponding to higher degrees of unsaturation. As shown in Figure 4.13, the most pronounced moistening occurred below the 700-hPa level. Given that the large-scale environment was relatively slow-evolving, it is unlikely that a region would experience a

doi:10.6342/NTU202504817

shift from dry advection to moist advection within only a few hours. Moreover, the farther a layer is from the lower boundary, the less likely it is to reach saturation without precipitation. Thus, the pronounced low-level moistening in the IOP3 case was inferred to be primarily driven by precipitation.

In the early stage of the IOP3 case, the relatively dry low-level atmosphere over northern Taiwan likely contributed to the weak surface rainfall through the evaporation of precipitation particles. However, as time progressed and the low-level dry regions gradually diminished, the impact of this mechanism also decreased. Hence, in the middle to later stages of the IOP3 case, the limited precipitation may no longer be attributed to this process. These findings will be further supported by cloud microphysical evidence in Section 4.4.5.

4.3 Kinematic Insights

After comparing the vertical thermodynamic structures of the two cases, mesoscale and convective-scale processes were further investigated. Using the SAMURAI-TERRAIN wind retrievals, we examined the physical mechanisms that led to significant rainfall totals over northern Taiwan during the SOP1 case, as well as the possible reasons for the limited precipitation in the same region during the IOP3 case, from a kinematic perspective.

doi:10.6342/NTU202504817

4.3.1 The SOP1 Case

As discussed in Section 3.2, two episodes of enhanced surface precipitation were observed over northern Taiwan during the SOP1 case (Figure 3.3c). The first episode (EP1) featured a station-averaged hourly rainfall increase starting around 0800 Z, reaching its peak between 0900 Z and 1000 Z, and then gradually weakening. In contrast, the second episode (EP2) began with a modest intensification around 1300 Z, but its peak rainfall was only about half of that in the first episode. Therefore, this study mainly focused on investigating the mechanisms responsible for EP1, while EP2 was only briefly described. Furthermore, given that similar features were observed throughout the layer from 1.5 km to 3 km (figures not shown), the 2-km level was selected for subsequent illustration.

At 0700 Z (Figure 4.14a), the 2-km wind field over northern Taiwan and the adjacent offshore region was dominated by southwesterly winds throughout most of the domain, with northwesterly winds prevailing only north of 25.3°N and west of 121.3°E. These two wind regimes converged over the northern Taiwan Strait, forming distinct yet isolated convergence zones, where new convective cells were continuously generated and advected eastward toward northern Taiwan. It should be noted that the convergence was manifested not only in wind direction but also in wind speed (i.e., the deceleration of the southwesterlies). By 0736 Z (Figure 4.14b), the convergence zones over the northern

doi:10.6342/NTU202504817

Taiwan Strait had continued to develop and were organized into banded structures that extended eastward toward the coastal areas of northern Taiwan, resulting in a marked increase in both radar reflectivity and convergence values in this region.

At 0800 Z (Figure 4.14c), the aforementioned northwesterly wind regime had clearly expanded eastward to 121.5°E. By 0836 Z (Figure 4.14d), convection over northern Taiwan had become quite vigorous, with a corresponding increase in precipitation as revealed by Figure 3.3c. Furthermore, as the northwesterly wind regime continued to shift eastward, it had almost entirely dominated the portion of the East China Sea directly north of Taiwan, while on the western edge of the analysis domain over the Taiwan Strait between 25.3°N and 25.5°N, the previous northwesterlies were gradually replaced by southwesterlies. Therefore, although convergence zones still existed over the northern Taiwan Strait at this time, they had significantly weakened compared to earlier time points.

Between 0900 Z and 1200 Z (Figure 4.15a–d), the winds northwest of Taiwan were gradually replaced by the southwesterlies, leading to a notable weakening of convergence and a slowdown in the generation of new convective cells over the region. Therefore, when the convective systems over northern Taiwan approached the final stages of their life cycles and weakened, precipitation declined accordingly. These results indicate that the evolution of the northwesterly wind regime and low-level convergence zones largely controlled the initiation, development, and decay of EP1, as the associated low-level

doi:10.6342/NTU202504817

convergence provided an important lifting mechanism necessary for the continual generation of new convective cells, which were subsequently transported eastward into northern Taiwan and produced sustained rainfall.

Subsequently, by 1336 Z (Figure 4.15e), the prevailing winds over Taiwan and the surrounding areas had entirely shifted to southwesterlies, indicating that EP2 was largely unrelated to the low-level convergence zones previously observed. In fact, this episode was mainly associated with convective systems that initially developed along the coast of central Taiwan and moved downwind under the prevailing southwesterlies (figures not shown), whereas its initiation mechanism lies beyond the scope of the present study.

4.3.2 The IOP3 Case

As discussed in Section 3.2, two episodes of enhanced surface precipitation were also observed over northern Taiwan during the IOP3 case (Figure 3.3d). The station-averaged hourly rainfall began to increase slightly from 0800 Z and 1500 Z, respectively, and gradually decreased about two hours later. However, compared to the SOP1 case, the precipitation in these episodes was minimal. For consistency with the previous discussion, the analysis here also focused on the 2-km level, although similar features were likewise observed throughout the layer from 1.5 km to 3 km (figures not shown).

During both the first (Figure 4.16a–d) and second (Figure 4.17a–d) episodes, the 2-

doi:10.6342/NTU202504817

km wind field around Taiwan was characterized by strong and relatively uniform southwesterlies. Hence, the resulting convergence zones were fewer, weaker, and less organized, preventing the continuous generation and eastward advection of convective cells toward northern Taiwan as observed in the SOP1 case. Moreover, although numerous strong convective systems initially developed over the offshore region, they exhibited a pronounced weakening during eastward propagation and became predominantly stratiform precipitation systems prior to reaching the coast (see Section 4.4.1 for cloud microphysical evidence), thereby limiting substantial precipitation over northern Taiwan.

4.4 Warm-Cloud Microphysical Insights

Given the distinct thermodynamic and kinematic features of the SOP1 and IOP3 cases, their accompanying cloud microphysical processes were expected to differ as well. Thus, various observations from the S-Pol radar were analyzed to elucidate how these processes contributed to differences in precipitation features between the two cases. All subsequent analyses in this section were conducted over the area shown in Figure 2.4.

4.4.1 Temporal Evolution of Different Precipitation Regimes

By using the convective-stratiform separation algorithm described in Section 2.7, we

doi:10.6342/NTU202504817

first analyzed how the fractions of the total convective precipitation regimes (including deep, moderate, and shallow convection), stratiform precipitation regimes, and weak-echo regions evolved with time for the SOP1 and IOP3 cases over northern Taiwan (Figure 4.18a, b). During EP1 for both cases (orange-shaded portions in Table 4.2 and Table 4.3), the stratiform precipitation accounted for the largest fraction. However, the total convective precipitation in the SOP1 case was approximately two to three times as much as that in the IOP3 case. Meanwhile, the combined fraction of stratiform precipitation and weak-echo regions in the IOP3 case exceeded 80%, higher than that in the SOP1 case. Given the limited spatial domain, the expansion of the convective precipitation regimes caused them to become the leading contributors to precipitation. Therefore, during this period, precipitation in the SOP1 case was primarily dominated by convective precipitation, reflecting the continual generation and eastward propagation of new convective cells toward northern Taiwan. In contrast, precipitation in the IOP3 case was mainly stratiform, associated with the dissipation of offshore convective systems.

As for EP2 for both cases (white-shaded portions in Table 4.2 and Table 4.3), the fraction of total convective precipitation in the SOP1 case decreased markedly relative to the first episode as the convective systems weakened, and the dominant precipitation gradually shifted to stratiform. Meanwhile, in the IOP3 case, although stratiform precipitation still accounted for a certain fraction, the proportion of the weak-echo regions

doi:10.6342/NTU202504817

increased substantially, causing a joint dominance of the two.

Next, the convective precipitation regimes were further divided into deep, moderate, and shallow convection, after which the temporal evolution of their fractions was analyzed (Figure 4.19a, b). During both EP1 (orange-shaded portions in Table 4.4 and Table 4.5) and EP2 (white-shaded portions in Table 4.4 and Table 4.5) for both cases, moderate convection dominated the convective precipitation, suggesting that the rainfall did not arise from typical deep convection. Notably, even the SOP1 case exhibited this feature, consistent with the sparse lightning activity on that day and the observations from S-Pol RHI (Range Height Indicator) of 60° azimuth (figures not shown).

Hence, the contrasting kinematic features between the two cases may result in distinct dominant precipitation regimes, which in turn became one of the key factors responsible for their marked discrepancy in accumulated rainfall.

4.4.2 Temporal Evolution of S-Pol PID and Polarimetric Parameters

Considering the differences in the dominant precipitation regime between the two cases, the associated precipitation types and hydrometeor characteristics (e.g., particle size, number concentration, and liquid water content) also varied. We then analyzed the temporal evolution of rain particle identification (PID; light, moderate, and heavy rain) and polarimetric parameters at 1.5-km height over northern Taiwan, as observed by the

doi:10.6342/NTU202504817

S-Pol radar.

For the SOP1 case, only a minor fraction of heavy rain was observed, whereas the proportion of moderate rain increased notably around 0727 Z and 1324 Z, with the former being the most pronounced, reaching approximately 50% (Figure 4.20a). This feature corresponded to convective-dominated precipitation and the period of fastest accumulated rainfall increase over northern Taiwan. Furthermore, radar reflectivity was mostly below 45 dB*Z* (Figure 4.20b), and the increase in the fraction of moderate rain aligned with the rise in reflectivity. Since radar reflectivity is controlled by both the size and number concentration of the particles, further comparison of the temporal evolution of Z_{DR} and K_{DP} helps clarify their relative contributions:

(1) Throughout the analysis period, Z_{DR} remained mostly below 2 dB (Figure 4.20c). Based on the schematic of Wakimoto and Bringi (1988), as shown in Figure 2.6, the maximum particle size can be estimated at approximately 1.75 mm. Because the typical size threshold for raindrops is around 1000 μm (i.e., 1 mm), the precipitation particles in the SOP1 case were primarily of medium to small size.

(2) Meanwhile, K_{DP} was generally below 1 °/km (Figure 4.20d). During periods of increasing radar reflectivity, Z_{DR} and K_{DP} also rose in phase, indicating that enhancements in reflectivity and precipitation were primarily driven by simultaneous increases in both particle size and liquid water content. However, their

doi:10.6342/NTU202504817

relative contributions varied over time: EP1 was dominated by increases in liquid water content, whereas EP2 was influenced more by growth in particle size. Nevertheless, the overall particle size was still small, keeping Z_{DR} below 2 dB.

Compared with the SOP1 case, the IOP3 case featured a much lower fraction of heavy rain, a moderate rain proportion peaking at only about 23%, and light rain being the predominant type overall (Figure 4.21a). This feature corresponded to stratiform-dominated precipitation during this period. Moreover, radar reflectivity was mostly below 40 dB*Z*, with a notable increase in the fraction of reflectivity values ≤ 25 dB*Z* (Figure 4.21b), reflecting its overall weaker echoes and, consequently, limiting the accumulated rainfall. A further examination of the temporal evolution of Z_{DR} and K_{DP} revealed that:

(1) Throughout the analysis period of the IOP3 case, the majority of Z_{DR} were below 2 dB (Figure 4.21c), indicating that its precipitation particles were also dominated by medium to small size, similar to the SOP1 case. A comparison of EP1 between the two cases (bounded by yellow lines in Figure 4.20c and Figure 4.21c) showed that the IOP3 case had slightly higher proportions of both $Z_{DR} > 1$ dB and $Z_{DR} < 0.5$ dB, suggesting a more diverse particle size distribution with both larger and smaller particles. Therefore, it is difficult to determine which case contained larger particles solely from Z_{DR}, and further verification is required. In contrast, during EP2

doi:10.6342/NTU202504817

(bounded by orange lines in Figure 4.20c and Figure 4.21c), the proportion of Z_{DR} < 0.5 dB was substantially higher in the IOP3 case, implying that precipitation particles were generally larger in the SOP1 case.

(2) Meanwhile, throughout the analysis period of the IOP3 case, K_{DP} was generally below 0.3 °/km (Figure 4.21d), considerably lower than that in the SOP1 case, indicating reduced liquid water content and number concentrations of particles.

Taken together, although precipitation particles in both the SOP1 and IOP3 cases were generally of medium to small size, the former exhibited markedly higher low-level liquid water content. This difference likely contributed to the substantially greater rainfall totals over northern Taiwan in the SOP1 case.

4.4.3 CFAD Analysis for EP1

To verify the hypotheses proposed in Section 4.4.2, this section employed contour frequency by altitude diagrams (CFADs; Yuter and Houze 1995) for both cases and only focused on EP1.

(1) Radar Reflectivity Factor (Z_H)

At an altitude of 1.5 km, the frequency distributions of radar reflectivity for the SOP1 case were broader and extended more toward the higher values than those in

doi:10.6342/NTU202504817

the IOP3 case, regardless of the analysis regime considered, including the entire analysis domain (Figure 4.22a, b), the convective precipitation regimes (Figure 4.22c, d), and the stratiform precipitation regimes (Figure 4.22e, f). Also, the frequency of high reflectivity values was notably greater, indicating that both the convective and stratiform precipitation systems developing over northern Taiwan during the SOP1 case were stronger.

For the convective precipitation regimes, the height of 1% 35-dB*Z* reflectivity for the SOP1 case was approximately 6.2 km, higher than the 5.8 km observed for the IOP3 case, indicating that the convective system of the former case was slightly deeper on average, although still shallower than typical deep convection. Hence, its associated precipitation did not resemble short-lived, intense rainfall.

Moreover, for the entire analysis domain, the IOP3 case exhibited a marked increase in the frequency of high reflectivity values at approximately 4.5 km (i.e., a bright band signature), whereas no such feature was observed in the SOP1 case. Since the melting layers in both cases were at similar altitudes, the presence of a clearer bright band in the IOP3 case suggests a higher proportion of stratiform precipitation in its system, consistent with the previous analysis.

(2) Differential Reflectivity (Z_{DR})

At 1.5-km altitude, the frequency distributions of Z_{DR} for both the entire

doi:10.6342/NTU202504817

analysis domain (Figure 4.23a, b) and the stratiform precipitation regimes (Figure 4.23e, f) were similar between the SOP1 and IOP3 cases, indicating no substantial differences in the diversity of particle sizes. As for the convective precipitation regimes (Figure 4.23c, d), although both the Z_{DR} distributions and mean values in the IOP3 case tended toward higher values compared to the SOP1 case, the discrepancy remained insignificant. Hence, particle size may not be a primary factor contributing to the pronounced difference in rainfall totals between the two cases.

For the entire analysis domain, Z_{DR} in the 0.5−1 dB range occurred with frequencies of 10%−15% extended up to approximately 4 km in the SOP1 case, compared to only about 2.7 km in the IOP3 case (a similar pattern was also observed in the analysis of convective precipitation regimes), suggesting that the updrafts may have been more pronounced in the SOP1 case.

Moreover, for the convective and stratiform precipitation regimes, the mean Z_{DR} in the IOP3 case exhibited a clear downward decrease between 6 and 8 km compared to the SOP1 case. According to the conceptual model of Kumjian et al. (2022), as shown in Figure 1.2, this pattern is therefore hypothesized to be associated with more pronounced riming processes above the melting layer in the IOP3 case.

(3) Specific Differential Phase (K_{DP})

At an altitude of 1.5 km, for the entire analysis domain (Figure 4.24a, b), the

doi:10.6342/NTU202504817

convective precipitation regimes (Figure 4.24c, d), and the stratiform precipitation regimes (Figure 4.24e, f), the frequency distributions of K_{DP} in the SOP1 case were broader and extended further toward higher values compared to the IOP3 case, indicating its more diverse and greater liquid water content. In contrast, the IOP3 case exhibited narrower K_{DP} distributions concentrated at smaller values, reflecting its more uniform and less liquid water content. Similarly, the mean profiles of K_{DP} also exhibited this pattern, especially in the convective precipitation regimes. Thus, liquid water content may be the key to explaining the pronounced difference in rainfall totals between the two cases.

(4) Vertical Velocity (w)

For both the entire analysis domain (Figure 4.25a, b) and the convective precipitation regimes (Figure 4.25c, d), the frequency distributions of vertical velocity in the middle troposphere (approximately 5–6 km) extended to 6 m s^{-1} in the SOP1 case, compared to only 2.5–3 m s^{-1} in the IOP3 case. That is, the most vigorous mid-level updrafts in the SOP1 case were nearly two to three times as strong as those in the IOP3 case, likely enhancing collision-coalescence (see Section 4.4.5 for further confirmation) and resulting in a continued downward increase of K_{DP} (Figure 4.24a, c, e) and liquid water content based on Figure 1.1.

Moreover, for the stratiform precipitation regimes (Figure 4.25e, f), the mean

doi:10.6342/NTU202504817

profile of vertical velocity in the SOP1 case exhibited upward motion throughout the column. In contrast, the IOP3 case featured mesoscale downdraft below the melting layer and weak updraft above it, more closely resembling the typical structure of a stratiform precipitation system (Houze 1997). Consistent with this structure, the IOP3 case possessed more fully developed stratiform precipitation regimes with clearer bright band signatures (Figure 4.22f), whereas those in the SOP1 case exhibited characteristics intermediate between convective and typical stratiform precipitation (Figure 4.22e).

4.4.4 CFAD Analysis for EP2

In this section, CFADs were also employed to analyze EP2 for both cases.

(1) Radar Reflectivity Factor (Z_H)

Regardless of the case or analysis regime, the frequency distributions and mean values of Z_H during EP2 tended toward lower values relative to EP1 (Figure 4.22 and Figure 4.26), reflecting generally weaker precipitation systems at that time. Nevertheless, the SOP1 case remained stronger than the IOP3 case. For the entire analysis domain, a pronounced bright band signature at 4.5 km was observed in the SOP1 case (Figure 4.26a), implying that the system may have been dominated by typical stratiform precipitation (see also Figure 4.26e for evidence). Meanwhile,

doi:10.6342/NTU202504817

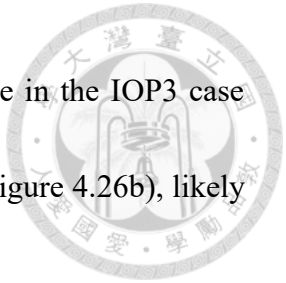

although the bright band near the melting layer was still visible in the IOP3 case during EP2, it was less distinct than in EP1 (Figure 4.22b and Figure 4.26b), likely due to an increased proportion of weak-echo regions.

(2) Differential Reflectivity (Z_{DR})

Because the frequency distributions and mean values of Z_{DR} were very similar in both cases for the convective precipitation regimes (Figure 4.27c, d), the drop size properties did not differ notably. By contrast, for the stratiform precipitation regimes (Figure 4.27e, f), particles were slightly larger in the SOP1 case than in the IOP3 case, potentially contributing to the difference in rainfall totals between the two cases. Since stratiform precipitation dominated over convective precipitation, the same feature was also evident for the entire analysis domain (Figure 4.27a, b).

(3) Specific Differential Phase (K_{DP})

Regardless of the analysis regime (Figure 4.28), the SOP1 case still exhibited higher liquid water content than the IOP3 case during EP2, as indicated by the frequency distributions of K_{DP} exceeding 0.25 °/km and its mean values. Hence, this higher liquid water content also contributed to the discrepancy in rainfall totals between the two cases.

(4) Vertical Velocity (w)

Regardless of the analysis regime (Figure 4.29), the frequency distributions of

doi:10.6342/NTU202504817

vertical velocity in the middle troposphere (approximately 5–6 km) extended to 5 m s^{-1} in the SOP1 case, compared to only 3.5 m s^{-1} in the IOP3 case. Namely, the most vigorous mid-level updrafts in the SOP1 case were about 1.4 times as strong as that in the IOP3 case (also evident in the mean profiles), potentially conducive to enhanced collision-coalescence and resulting in greater liquid water content at low levels.

4.4.5 Parameter Space Analysis

Based on the previous CFADs analysis, differences in particle size and liquid water content between the SOP1 and IOP3 cases had been identified, implying that the former case might be associated with more pronounced collision-coalescence. To verify this hypothesis, we applied the four-quadrant parameter space originally proposed by Kumjian and Prat (2014), using the vertical gradient of Z_H as the horizontal axis and that of Z_{DR} as the vertical axis, with each quadrant representing one or more warm-rain microphysical processes (see Figure 4 in Kumjian et al. 2022). In their study, the vertical gradient was defined as changes toward the ground; in the present study, it was specifically defined as the value at 1.5 km minus that at 3.5 km, with the upper level chosen to avoid the influence of the melting layer. Additionally, only grid points with a correlation coefficient (ρ_{HV}) greater than 0.98 were included to filter out mixed-phase

doi:10.6342/NTU202504817

processes. Through this framework, the dominant warm-rain microphysical processes at each time point could be clearly visualized.

First, the analysis results of EP1 for both cases are summarized as follows:

(1) For the SOP1 case, the dominant microphysical process was collision-coalescence regardless of the analysis regime (Figure 4.30a, c, e), with points in the parameter space relatively concentrated. This indicates lower temporal variability in its microphysical features, allowing the same state to persist for a longer duration; consequently, intense precipitation was more easily maintained, resulting in a higher fraction of moderate and heavy rain. Collectively, the larger proportion of convective precipitation at this time was associated with stronger updrafts, which further promoted collision-coalescence, increased the liquid water content in the lower troposphere, and thereby favored the occurrence of significant rainfall totals.

(2) For the IOP3 case, the dominant microphysical process was initially evaporation and gradually transitioned to collision-coalescence regardless of the analysis regime (Figure 4.30b, d, f). This initial evaporation highlighted that the early-stage low-level dry regions revealed in Section 4.2 were definitely one of the reasons for the weak precipitation at the beginning of the IOP3 case. Moreover, the points in the parameter space were relatively dispersed, indicating higher temporal variability in its microphysical features. Hence, intense precipitation was difficult to maintain,

doi:10.6342/NTU202504817

leading to a lower fraction of moderate and heavy rain.

(3) Although the IOP3 case exhibited stronger instantaneous collision-coalescence at certain time points, this process remained more pronounced in the SOP1 case on average (see the red crosses in Figure 4.30), consistent with the previous inference.

Next, EP2 was analyzed for both cases. In the SOP1 case, collision-coalescence remained the dominant microphysical process in both the convective (Figure 4.31c) and stratiform (Figure 4.31e) precipitation regimes. By contrast, the IOP3 case exhibited a combination of collision-coalescence and evaporation in the convective regimes (Figure 4.31d) and was dominated by evaporation, with occasional collisional breakup, in the stratiform regimes (Figure 4.31f). These results indicate that collision-coalescence was still more pronounced in the SOP1 case at this stage, also consistent with the previous inference. Moreover, for each case, the distributions of points in the parameter space for the entire analysis domain (Figure 4.31a, b) closely resembled those for the stratiform regimes, reflecting that stratiform precipitation had become dominant at this time, in agreement with earlier conclusions.

4.4.6 Low-Level Size Sorting Signature for the IOP3 Case

Previous analysis revealed that the dominant microphysical processes during the

doi:10.6342/NTU202504817

early stage of EP1 in the IOP3 case over the entire analysis domain primarily fell in the second quadrant of the parameter space, associated with evaporation and size sorting (Figure 4.30b). Although the signal clearly reflected evaporation, we further examined whether the size sorting signature was indeed absent at this time through the method described in Section 2.8.

Size sorting, the process by which precipitation particles of different sizes separate due to their distinct fall speeds, is typically manifested in dual-polarization Doppler radar observations as spatially displaced regions of enhanced Z_{DR} and K_{DP}. Larger particles tend to form localized Z_{DR} maxima near convective updrafts owing to their faster fall speeds and reduced advection by the environmental flow, while smaller particles produce K_{DP} maxima farther away due to the converse reasons. The greater the separation, the more pronounced the size sorting process, and vice versa (see Figure 17 in Tam et al. 2022 for the conceptual diagram). In general, stronger updrafts are likely to enhance the size sorting process, whereas weaker updrafts may reduce its prominence.

As shown in Figure 4.32, during EP1 of the IOP3 case, the mean separation distance between paired Z_{DR} and K_{DP} objects was generally within 3 km, except at 0812 Z. This mean distance is substantially smaller than that reported in previous analyses of intense convective systems (references listed in Section 2.8), further confirming that the size sorting signature was not pronounced during this period. Given the weak convective

doi:10.6342/NTU202504817

updrafts in the IOP3 case, this result is also physically reasonable.

It should be noted that the time series shown in Figure 4.32 exhibited considerable fluctuations, likely influenced by the complex terrain of northern Taiwan: local circulations or corner flows could limit the horizontal advection of smaller particles, thereby reducing the mean separation distance between the paired Z_{DR} and K_{DP} objects. Additionally, since the IOP3 case consisted of multiple weaker, spatially scattered systems rather than organized deep convections over northern Taiwan, it was difficult to use the angle between the line connecting the centroids of paired Z_{DR}-K_{DP} objects and the storm motion as one of the criteria for filtering out incorrect matches. This may also account for the relatively large mean separation distance observed at 0812 Z.

doi:10.6342/NTU202504817

Chapter 5 Conclusions and Future Work

5.1 Conclusions

During TAHOPE 2022, two Meiyu fronts affected Taiwan, observed first from SOP1 to IOP1 and subsequently during IOP3. Between 0700–1900 Z on 5/25 (hereafter the SOP1 case) and 0700–1900 Z on 6/06 (hereafter the IOP3 case), the average positions of the Meiyu fronts at 975 hPa over the Taiwan Strait were nearly identical, differing by less than 50 km. Nevertheless, both rain gauge observations and quantitative precipitation estimation indicated that the accumulated rainfall over northern Taiwan was substantially greater in the SOP1 case, with a mean value about 3.4 times as much as that of the IOP3 case.

Meanwhile, the synoptic-scale analysis revealed that, compared with the SOP1 case, the IOP3 case exhibited greater frontal slope and intensity, stronger low-level winds, and enhanced upstream moisture transport, but with limited accumulated rainfall over northern Taiwan. By contrast, the SOP1 case was only more favorable in terms of specific humidity and total precipitable water, yet the produced rainfall totals were still considerable. From the above findings, it can be inferred that the structure and intensity of the front are not necessarily positively correlated with the resulting total rainfall. Factors such as moisture content, local atmospheric instability, and mesoscale, convective-scale, or cloud microphysical processes are likely more important.

doi:10.6342/NTU202504817

Hence, this study further examined the potential impacts of these factors on total rainfall. First, analysis of the thermodynamic fields based on sounding data revealed that the lower to mid-troposphere below 500 hPa was quite moist during the SOP1 case. This moisture-rich environment reduced raindrop evaporation and likely enhanced cloud-microphysics precipitation efficiency. On the other hand, the IOP3 case initially featured pronounced low-level dry regions, particularly below 700 hPa. These dry regions may have caused precipitation particles to evaporate before reaching the surface, thereby limiting rainfall during its early stage.

Next, SAMURAI-TERRAIN wind retrievals revealed contrasting kinematic features between the two cases. In the SOP1 case, persistent low-level convergence zones between northwesterlies and southwesterlies over the offshore region northwest of Taiwan continuously generated new convective cells that propagated onshore. Conversely, in the IOP3 case, the low-level wind field featured strong, uniform southwesterlies, yielding fewer and weaker convergence zones; thus, a small number of new convective systems developed, most of which were already decaying upon reaching northern Taiwan.

Accordingly, pronounced differences in rainfall categories and vertical motion were observed over northern Taiwan between the two cases. In the SOP1 case, convective precipitation dominated the early stage, followed by stratiform precipitation after the convective systems dissipated, resulting in a higher proportion of moderate rain and

doi:10.6342/NTU202504817

stronger updrafts overall. In contrast, the IOP3 case was initially dominated by stratiform precipitation, with stratiform and weak-echo regions jointly dominating in the later stage, leading to a lower proportion of moderate rain and weaker updrafts overall.

Finally, regarding warm-cloud microphysical processes, as indicated by S-Pol radar data, the stronger updrafts in the SOP1 case enhanced collision-coalescence, whereas in the IOP3 case, evaporation initially dominated, followed by weaker collision-coalescence, and then a combination of evaporation and weak collision-coalescence. These contrasts further shaped their hydrometeor characteristics: although both cases featured medium- to small-sized drops (as indicated by Z_{DR}), the more pronounced collision-coalescence in the SOP1 case led to substantially higher low-level liquid water content / raindrop number concentration (as inferred from K_{DP}), primarily driving the discrepancies in accumulated rainfall between the two cases, with drop size only playing a secondary role.

In conclusion, although the SOP1 case exhibited a gentler frontal slope and weaker frontal intensity, more favorable thermodynamic conditions, more organized mesoscale-to-convective-scale kinematic features, greater low-level liquid water content, and potentially higher cloud-microphysics precipitation efficiency collectively enabled significant accumulated rainfall over northern Taiwan. Conversely, the IOP3 case lacked these advantages; thus, despite its stronger front, it still failed to produce rainfall totals comparable to those of the SOP1 case (see Table 5.1 for a summary of the key findings).

doi:10.6342/NTU202504817

5.2 Future Work

In this study, we primarily compared particle sizes between the SOP1 and IOP3 cases using dual-polarization radar parameters (i.e., Z_{DR}). Because disdrometer observations are also included in TAHOPE, future analysis of these data could provide the actual drop size distribution over northern Taiwan and verify the current conclusions. Moreover, since the present study relies solely on observational data, the exploration of the fundamental physical mechanisms underlying the differences in the development and activity of convection between the two cases has not yet been fully understood. Therefore, future work could combine thermodynamic retrievals with high-resolution Weather Research and Forecasting (WRF) numerical simulations to calculate potential temperature perturbations and pressure perturbations, which would not only help locate the Meiyu front but also enable a more detailed investigation of the dynamical mechanisms and their impacts on the observed cloud microphysical features and processes. Finally, future diagnosis of the secondary circulation associated with the Meiyu front could clarify whether frontolysis in the IOP3 case contributed to the suppressed accumulated rainfall over northern Taiwan.

doi:10.6342/NTU202504817

References

Akiyama, T., 1973: The large-scale aspects of the characteristic features of the Baiu front. *Pap. Meteor. Geophys*, **24,** 157-188.

Akiyama, T., 1990: Large, Synoptic and Meso Scale Variations of the Baiu Front, during July 1982 Part II: Frontal Structure and Disturbances. *J. Meteor. Soc. Japan*, **68,** 557-574, https://doi.org/10.2151/jmsj1965.68.5_557.

Bell, M. M., M. T. Montgomery, and K. A. Emanuel, 2012: Air–Sea Enthalpy and Momentum Exchange at Major Hurricane Wind Speeds Observed during CBLAST. *J. Atmos. Sci.*, **69,** 3197-3222, https://doi.org/10.1175/jas-d-11-0276.1.

Bringi, V. N., and V. Chandrasekar, 2001: *Polarimetric Doppler weather radar: principles and applications.* Cambridge university press, 636 pp.

Cha, T.-Y., and M. M. Bell, 2023: Three-Dimensional Variational Multi-Doppler Wind Retrieval over Complex Terrain. *J. Atmos. Oceanic Technol.*, **40,** 1381-1405, https://doi.org/10.1175/jtech-d-23-0019.1.

Chang, P.-L., and Coauthors, 2021: An Operational Multi-Radar Multi-Sensor QPE System in Taiwan. *Bull. Amer. Meteor. Soc.*, **102,** E555-E577, https://doi.org/10.1175/bams-d-20-0043.1.

Chen, G. T.-J., 1983: Observational Aspects of the Mei-Yu Phenomenon in Subtropical China. *J. Meteor. Soc. Japan*, **61,** 306-312, https://doi.org/10.2151/jmsj1965.61.2_306.

Chen, G. T.-J., C.-C. Wang, and D. T.-W. Lin, 2005: Characteristics of Low-Level Jets over Northern Taiwan in Mei-Yu Season and Their Relationship to Heavy Rain Events. *Mon. Wea. Rev.*, **133,** 20-43, https://doi.org/10.1175/MWR-2813.1.

Chen, Q., 1982: The Instability of the Gravity-inertia Wave and its Relation to Low-level Jet and Heavy Rainfall. *J. Meteor. Soc. Japan*, **60,** 1041-1057, https://doi.org/10.2151/jmsj1965.60.5_1041.

Chen, S.-J., Y.-H. Kuo, W. Wang, Z.-Y. Tao, and B. Cui, 1998: A Modeling Case Study of Heavy Rainstorms along the Mei-Yu Front. *Mon. Wea. Rev.*, **126,** 2330-2351, https://doi.org/10.1175/1520-0493(1998)126%3C2330:AMCSOH%3E2.0.CO;2.

Chen, T.-J. G., and C.-P. Chang, 1980: The Structure and Vorticity Budget of an Early

doi:10.6342/NTU202504817

Summer Monsoon Trough (Mei-Yu) over Southeastern China and Japan. *Mon. Wea. Rev.*, **108,** 942-953, https://doi.org/10.1175/1520-0493(1980)108%3C0942:TSAVBO%3E2.0.CO;2.

Chen, Y.-L., C.-K. Wang, C.-C. Tu, F. Hsiao, and P.-L. Lin, 2022: Revisiting a Mei-Yu Front Associated with Heavy Rainfall over Taiwan during 6–7 June 2003. *Atmosphere*, **13**, https://doi.org/10.3390/atmos13050644.

Cornejo, I. C., A. K. Rowe, K. L. Rasmussen, and J. C. DeHart, 2024: Orographic Controls on Extreme Precipitation Associated with a Mei-Yu Front. *Mon. Wea. Rev.*, **152,** 531-551, https://doi.org/10.1175/mwr-d-23-0170.1.

DeHart, J. C., and M. M. Bell, 2020: A Comparison of the Polarimetric Radar Characteristics of Heavy Rainfall From Hurricanes Harvey (2017) and Florence (2018). *J. Geophys. Res.*, **125**, https://doi.org/10.1029/2019jd032212.

Didlake, A. C., and R. A. Houze, 2009: Convective-Scale Downdrafts in the Principal Rainband of Hurricane Katrina (2005). *Mon. Wea. Rev.*, **137,** 3269-3293, https://doi.org/10.1175/2009MWR2827.1.

Ding, Y., 1992: Summer Monsoon Rainfalls in China. *J. Meteor. Soc. Japan*, **70,** 373-396, https://doi.org/10.2151/jmsj1965.70.1B_373.

Foerster, A. M., M. M. Bell, P. A. Harr, and S. C. Jones, 2014: Observations of the Eyewall Structure of Typhoon Sinlaku (2008) during the Transformation Stage of Extratropical Transition. *Mon. Wea. Rev.*, **142,** 3372-3392, https://doi.org/10.1175/mwr-d-13-00313.1.

Fritz, C., Z. Wang, S. W. Nesbitt, and T. J. Dunkerton, 2016: Vertical structure and contribution of different types of precipitation during Atlantic tropical cyclone formation as revealed by TRMM PR. *Geophys. Res. Lett.*, **43,** 894-901, https://doi.org/10.1002/2015gl067122.

Gorgucci, E., and L. Baldini, 2015: Influence of Beam Broadening on the Accuracy of Radar Polarimetric Rainfall Estimation. *J. Hydrometeor.*, **16,** 1356-1371, https://doi.org/10.1175/jhm-d-14-0084.1.

Hersbach, H., and Coauthors, 2020: The ERA5 global reanalysis. *Quart. J. Roy. Meteor. Soc.*, **146,** 1999-2049, https://doi.org/10.1002/qj.3803.

Hersbach, H., and Coauthors, 2023: ERA5 hourly data on pressure levels from 1940 to

doi:10.6342/NTU202504817

present. *Copernicus climate change service (c3s) climate data store (cds)*, **10,** 24381, https://doi.org/10.24381/cds.bd0915c6.

Hou, J.-P., C.-Y. Chen, and P.-D. Jeng, 2025: A Case Study Simulation of the Heavy Rainfall Event in Southwestern Taiwan during the Mei-Yu Front on May 22, 2020. *Asia-Pacific Journal of Atmospheric Sciences*, **61**, https://doi.org/10.1007/s13143-025-00404-9.

Houze, R. A., 1997: Stratiform Precipitation in Regions of Convection: A Meteorological Paradox? *Bull. Amer. Meteor. Soc.*, **78,** 2179-2196, https://doi.org/10.1175/1520-0477(1997)078%3C2179:SPIROC%3E2.0.CO;2.

Houze, R. A., 2014: *Cloud Dynamics.* Vol. 104, Academic press, 432 pp.

Hu, Y., Y. Deng, Y. Lin, Z. Zhou, C. Cui, and X. Dong, 2021: Dynamics of the spatiotemporal morphology of Mei-yu fronts: an initial survey. *Climate Dyn.*, **56,** 2715-2728, https://doi.org/10.1007/s00382-020-05619-2.

Jameson, A., and E. Mueller, 1985: Estimation of Propagation-Differential Phase Shift from Sequential Orthogonal Linear Polarization Radar Measurements. *J. Atmos. Oceanic Technol.*, **2,** 133-137, https://doi.org/10.1175/1520-0426(1985)002%3C0133:EOPDPS%3E2.0.CO;2.

Jeong, J. H., D. I. Lee, C. C. Wang, S. M. Jang, C. H. You, and M. Jang, 2012: Environment and morphology of mesoscale convective systems associated with the Changma front during 9–10 July 2007. *Ann. Geophys.*, **30,** 1235-1248, https://doi.org/10.5194/angeo-30-1235-2012.

Jou, B. J.-D., W.-C. Lee, and R. H. Johnson, 2011: An Overview of SoWMEX/TiMREX. *The Global Monsoon System*, 2nd ed., C.-P. Chang, Ed., World Scientific, 303-318.

Kumjian, M. R., and O. P. Prat, 2014: The Impact of Raindrop Collisional Processes on the Polarimetric Radar Variables. *J. Atmos. Sci.*, **71,** 3052-3067, https://doi.org/10.1175/jas-d-13-0357.1.

Kumjian, M. R., O. P. Prat, K. J. Reimel, M. van Lier-Walqui, and H. C. Morrison, 2022: Dual-Polarization Radar Fingerprints of Precipitation Physics: A Review. *Remote Sensing*, **14**, https://doi.org/10.3390/rs14153706.

Kuo, Y.-H., and G. T.-J. Chen, 1990: The Taiwan Area Mesoscale Experiment (TAMEX):

doi:10.6342/NTU202504817

An Overview. *Bull. Amer. Meteor. Soc.*, **71,** 488-503, https://doi.org/10.1175/1520-0477(1990)071%3C0488:TTAMEA%3E2.0.CO;2.

Loeffler, S. D., and M. R. Kumjian, 2018: Quantifying the Separation of Enhanced ZDR and KDP Regions in Nonsupercell Tornadic Storms. *Wea. Forecasting*, **33,** 1143-1157, https://doi.org/10.1175/waf-d-18-0011.1.

Loeffler, S. D., M. R. Kumjian, M. Jurewicz, and M. M. French, 2020: Differentiating Between Tornadic and Nontornadic Supercells Using Polarimetric Radar Signatures of Hydrometeor Size Sorting. *Geophys. Res. Lett.*, **47,** e2020GL088242, https://doi.org/10.1029/2020gl088242.

Matsumoto, S., S. Yoshizumi, and M. Takeuchi, 1970: On the Structure of the "Baiu Front" and the Associated Intermediate-scale Disturbances in the Lower Atmosphere. *J. Meteor. Soc. Japan*, **48,** 479-491, https://doi.org/10.2151/jmsj1965.48.6_479.

Matsumoto, S., K. Ninomiya, and S. Yoshizumi, 1971: Characteristic Features of "Baiu" Front Associated with Heavy Rainfall. *J. Meteor. Soc. Japan*, **49,** 267-281, https://doi.org/10.2151/jmsj1965.49.4_267.

Ninomiya, K., 1984: Characteristics of Baiu Front as a Predominant Subtropical Front in the Summer Northern Hemisphere. *J. Meteor. Soc. Japan*, **62,** 880-894, https://doi.org/10.2151/jmsj1965.62.6_880.

Rogers, R. F., P. D. Reasor, J. A. Zawislak, and L. T. Nguyen, 2020: Precipitation Processes and Vortex Alignment during the Intensification of a Weak Tropical Cyclone in Moderate Vertical Shear. *Mon. Wea. Rev.*, **148,** 1899-1929, https://doi.org/10.1175/mwr-d-19-0315.1.

Ryzhkov, A. V., 2007: The Impact of Beam Broadening on the Quality of Radar Polarimetric Data. *J. Atmos. Oceanic Technol.*, **24,** 729-744, https://doi.org/10.1175/jtech2003.1.

Seliga, T. A., and V. Bringi, 1976: Potential Use of Radar Differential Reflectivity Measurements at Orthogonal Polarizations for Measuring Precipitation. *J. Appl. Meteor. Climatol.*, **15,** 69-76, https://doi.org/10.1175/1520-0450(1976)015%3C0069:PUORDR%3E2.0.CO;2.

Steiner, M., R. A. Houze Jr, and S. E. Yuter, 1995: Climatological Characterization of Three-Dimensional Storm Structure from Operational Radar and Rain Gauge Data. *J. Appl. Meteor. Climatol.*, **34,** 1978-2007, https://doi.org/10.1175/1520-

doi:10.6342/NTU202504817

0450(1995)034%3C1978:CCOTDS%3E2.0.CO;2.

Tam, F. I. H., M. J. Yang, and W. C. Lee, 2022: Polarimetric Size Sorting Signatures in the Convective Regions of Mesoscale Convective Systems in PECAN: Implications on Kinematics, Thermodynamics, and Precipitation Pathways. *J. Geophys. Res.*, **127,** e2021JD035822, https://doi.org/10.1029/2021jd035822.

Tao, C., and H. Jiang, 2015: Distributions of Shallow to Very Deep Precipitation–Convection in Rapidly Intensifying Tropical Cyclones. *J. Climate*, **28,** 8791-8824, https://doi.org/10.1175/jcli-d-14-00448.1.

Tu, C.-C., Y.-L. Chen, P.-L. Lin, and P.-H. Lin, 2020: The relationship between the boundary layer moisture transport from the South China Sea and heavy rainfall over Taiwan. *Terrestrial, Atmospheric and Oceanic Sciences*, **31,** 159-176, https://doi.org/10.3319/tao.2019.07.01.01.

Wakimoto, R., and V. Bringi, 1988: Dual-Polarization Observations of Microbursts Associated with Intense Convection: The 20 July Storm during the MIST Project. *Mon. Wea. Rev.*, **116,** 1521-1539.

Wang, C.-C., J. Chieh-Sheng Hsu, G. Tai-Jen Chen, and D.-I. Lee, 2014: A Study of Two Propagating Heavy-Rainfall Episodes near Taiwan during SoWMEX/TiMREX IOP-8 in June 2008. Part I: Synoptic Evolution, Episode Propagation, and Model Control Simulation. *Mon. Wea. Rev.*, **142,** 2619-2643, https://doi.org/10.1175/mwr-d-13-00331.1.

Wimmers, A. J., and C. S. Velden, 2011: Seamless Advective Blending of Total Precipitable Water Retrievals from Polar-Orbiting Satellites. *J. Appl. Meteor. Climatol.*, **50,** 1024-1036, https://doi.org/10.1175/2010jamc2589.1.

Wu, Y.-C., M.-J. Yang, and R. F. Rogers, 2022: Examining Terrain Effects on the Evolution of Precipitation and Vorticity of Typhoon Fanapi (2010) after Departing the Central Mountain Range of Taiwan. *Mon. Wea. Rev.*, **150,** 1517-1540, https://doi.org/10.1175/MWR-D-21-0205.1.

Yang, S.-C., S.-H. Chen, L. J.-Y. Liu, H.-L. Yeh, W.-Y. Chang, K.-S. Chung, P.-L. Chang, and W.-C. Lee, 2024: Investigating the Mechanisms of an Intense Coastal Rainfall Event during TAHOPE/PRECIP-IOP3 Using a Multiscale Radar Ensemble Data Assimilation System. *Mon. Wea. Rev.*, **152,** 2545-2567, https://doi.org/10.1175/mwr-d-24-0049.1.

doi:10.6342/NTU202504817

Yuter, S. E., and R. A. Houze, 1995: Three-Dimensional Kinematic and Microphysical Evolution of Florida Cumulonimbus. Part II: Frequency Distributions of Vertical Velocity, Reflectivity, and Differential Reflectivity. *Mon. Wea. Rev.*, **123,** 1941-1963, https://doi.org/10.1175/1520-0493(1995)123%3C1941:TDKAME%3E2.0.CO;2.

Yuter, S. E., and R. A. Houze, 1997: Measurements of Raindrop Size Distributions over the Pacific Warm Pool and Implications for Z–R Relations. *Journal of Applied Meteorology*, **36,** 847-867, https://doi.org/10.1175/1520-0450(1997)036%3C0847:MORSDO%3E2.0.CO;2.

Zhou, Y., S. Gao, and S. S. Shen, 2004: A Diagnostic Study of Formation and Structures of the Meiyu Front System over East Asia. *J. Meteor. Soc. Japan*, **82,** 1565-1576, https://doi.org/10.2151/jmsj.82.1565.

楊明仁、鄭明典、黃清勇、林沛練、林博雄、李清勝、王重傑、劉清煌、呂國臣、張保亮、黃椿喜、侯昭平、鍾高陞、張偉裕、林品芳，2023：臺灣區域豪雨觀測暨預報實驗(TAHOPE)簡介。*中華民國氣象學會會刊*，**64**，50-67。

doi:10.6342/NTU202504817

Tables

Table 1.1 List of IOPs and SOPs during TAHOPE 2022. (adapted from 楊明仁等，2023)

	Period	Dominant Weather Events and Observation Targets
SOP1	5/25 00Z – 5/26 00Z	Meiyu front and MCSs
IOP1	5/26 00Z – 5/28 00Z	Meiyu front and MCSs (Back-building MCS on 5/26)
IOP2	5/31 00Z – 5/31 12Z	Afternoon thunderstorm (Thunderstorms with deep echo top of 16-km over Yilan)
IOP3	6/06 06Z – 6/12 12Z	Quasi-stationary Meiyu front over Taiwan (Back-building MCS over Miaoli; a squall line approaching northern Taiwan on 6/10)
IOP4	6/15 00Z – 6/16 00Z	Prefrontal southwesterly associated with a weakening Meiyu front (Low-level dry air intrusion over northern Taiwan)
SOP2	6/23 00Z – 6/24 00Z	Afternoon thunderstorm
SOP3	6/24 00Z – 6/25 00Z	Afternoon thunderstorm with hail in Taipei Basin
IOP5	6/25 00Z – 6/25 15Z	Afternoon thunderstorm (Intense thunderstorms over Taipei, Taoyuan, and Miaoli)
SOP4	6/29 00Z – 6/30 00Z	Afternoon thunderstorm
IOP6	7/01 00Z – 7/04 00Z	Rainfall associated with TC Chaba and TC Aere (Heavy rainfall over eastern and southern Taiwan)
IOP7	7/05 00Z – 7/05 04Z	Typhoon Aere approaching Kyushu, Japan, with dropsonde observations (Heavy rainfall over Kyushu and Honshu, Japan)
SOP5	7/05 00Z – 7/06 00Z	Afternoon thunderstorm in Taipei Basin
SOP6	7/06 00Z – 7/07 00Z	Afternoon thunderstorm in Taipei Basin
IOP8	7/13 06Z – 7/16 06Z	Rainfall associated with TD 90W (Heavy rainfall over eastern and southern Taiwan)
SOP7	7/19 00Z – 7/20 00Z	Afternoon thunderstorm in Taipei Basin

doi:10.6342/NTU202504817

SOP8	7/20 00Z – 7/21 00Z	Afternoon thunderstorm in Taipei Basin
IOP9	7/29 00Z – 7/29 12Z	Moisture transport by low pressure system; occurrence of afternoon thunderstorm (Heavy rainfall in the evening; thunderstorms and lightning over northern Taiwan)
IOP10	8/01 00Z – 8/03 18Z	Moisture transport by low pressure system (Heavy rainfall in Taipei Basin, central Taiwan, and southern Taiwan)
IOP11	8/04 00Z – 8/04 12Z	Afternoon thunderstorm in Taipei Basin

Table 2.1 Descriptions for ERA5 reanalysis data.

Attributes	Descriptions
Data Type	Gridded
Projection	Regular latitude-longitude grid
Horizontal Coverage	Global
Horizontal Grid Spacing	0.25° × 0.25° (≈ 27 km × 27 km)
Vertical Coverage	from 1000 hPa to 1 hPa
Vertical Grid Spacing	37 fixed pressure levels
Temporal Coverage	from 1940 to present
Time Interval	Hourly

Table 2.2 Descriptions for CWB QPESUMS product in Taiwan.

Attributes	Descriptions
Data Type	Gridded
Horizontal Coverage	118°E – 123.5°E; 20°N – 27°N
Horizontal Grid Spacing	0.0125° × 0.0125° (≈ 1.4 km × 1.4 km)
Time Interval	10-minute

doi:10.6342/NTU202504817

Table 2.3 Basic specifications of the S-Pol, RCWF, and RCSL radars. In the following table, PPI stands for Plan Position Indicator, and RHI stands for Range Height Indicator.

Radar Name	S-Pol	RCWF	RCSL
Latitude (°N)	24.819088	25.073055	25.003888
Longitude (°E)	120.907463	121.773056	121.400555
Altitude	10 m	765 m	298 m
Wavelength	10 cm (S-band)	10 cm (S-band)	5 cm (C-band)
Radar Gate Spacing	150 m	250 m	250 m
Maximum Scanning Distance	300 km	460 km	148 km
Nyquist Velocity	33.34 m/s	26.56 – 33.62 m/s	39.85 m/s
Scanning Strategy	PPI & RHI	PPI	PPI
Scanning Interval for Complete PPI	12 min	6 min	7 min
Scanning Interval for Fixed RHI	12 min	---	---
Scanning Elevation Angle for PPI	0.5°, 1°, 1.5°, 2°, 3°, 4°, 5°, 7°, 9°, 11°	0.5°, 0.9°, 1.3°, 1.8°, 2.4°, 3.1°, 4.0°, 5.1°, 6.4°, 8.0°, 10.0°, 12.0°, 14.0°, 16.7°, 19.5°	1°, 2°, 3°, 4°, 5°, 6°, 9.9°, 14.6°, 19.5°, 24.5°, 29.9°
Scanning Azimuth Angle for Fixed RHI	0°, 30°, 45°, 60°, 75°, 85°, 90°, 101°, 137°, 183°, 225°, 270°, 281°, 315°	---	---

doi:10.6342/NTU202504817

Table 2.4 Summary of the classification criteria for different precipitation regimes based on radar reflectivity at 2-km height and the height of 20-dBZ echo top.

Precipitation Regimes	Classification Criteria
Convective Regimes	**Within the convective radius of each convective center** ● Convective center: Z > 42 or $(Z_{bg} + \Delta Z_{cc})$ dBZ ● Convective radius: $R = \begin{cases} 0.5, & Z_{bg} < 20 \\ 0.5 + 3.5\left(\frac{Z_{bg} - 20}{15}\right), & 20 \le Z_{bg} < 35 \\ 4, & Z_{bg} \ge 35 \end{cases}$ (Z_{bg}: background reflectivity; ΔZ_{cc}: convective center criterion)
Deep Convection (DC)	➢ Convective regimes ➢ Height of 20-dBZ echo top > 10 km
Moderate Convection (MC)	➢ Convective regimes ➢ 4 km < height of 20-dBZ echo top < 10 km
Shallow Convection (SC)	➢ Convective regimes ➢ Height of 20-dBZ echo top < 4 km
Stratiform Regimes (ST)	● Non-convective regimes ● Z > 20 dBZ at 2-km height
Weak-Echo Regions (WE)	● Non-convective regimes ● Z < 20 dBZ at 2-km height
No-Echo Regions (NE)	● Non-convective regimes ● Z = 0 or NaN at 2-km height

doi:10.6342/NTU202504817

Table 4.1 Summary of the synoptic-scale statistical analysis for the SOP1 and IOP3 cases. Values in parentheses indicate the relative strength of the stronger case compared to the weaker case, expressed as percentages. The cross (✕), ballot box with check (☑), and ordinary check mark (✓) denote the weaker case, the stronger case with relative strength ≥ 10%, and the stronger case with relative strength < 10%, respectively.

Categories	Factors	0000 – 0600 Z		0600 – 1200 Z	
		5/25 (SOP1)	6/06 (IOP3)	5/25 (SOP1)	6/06 (IOP3)
Kinematic	925-mb Wind (MBLJ)	✕	☑ (48.1%)	✕	☑ (37.9%)
	900-mb Wind (BJ)	✕	☑ (390.7%)	✕	☑ (189.6%)
	850-mb Wind (SLLJ)	✕	☑ (19.6%)	✕	✓ (9.9%)
	700-mb Wind (SLLJ)	✓ (5.3%)	✕	✕	☑ (13.5%)
Thermodynamic	925-mb Specific Humidity	✕	✓ (0.3%)	✓ (3.4%)	✕
	850-mb Specific Humidity	✓ (7.3%)	✕	✓ (7.5%)	✕
	700-mb Specific Humidity	☑ (42.0%)	✕	☑ (36.5%)	✕
	Total Precipitable Water	☑ (19.2%)	✕	☑ (15.8%)	✕
Moisture Transport	900–1000-mb IVT	✕	☑ (56.2%)	✕	☑ (42.8%)
	900–1000-mb IVT Divergence	✕	☑ (68.2%)	✕	☑ (178.3%)
	700–900-mb IVT	✓ (1.7%)	✕	✓ (1.1%)	✕
	700–900-mb IVT Divergence	☑ (22.3%)	✕	✕	☑ (40.7%)

doi:10.6342/NTU202504817

Table 4.2 Hourly fractions (%) of the total convective precipitation regimes (including deep, moderate, and shallow convection), stratiform precipitation regimes, and weak-echo regions for the SOP1 case. The orange- and white-shaded portions denote the first and second episodes of enhanced surface precipitation, respectively.

SOP1 Case (5/25 0700 – 1900 Z)			
Time (UTC)	**Total Convection (DC + MC + SC, %)**	**Stratiform (ST, %)**	**Weak Echo (WE, %)**
08:05	29.3	45.5	17.7
09:01	38.0	57.2	4.6
10:00	23.1	68.8	7.9
11:00	20.6	76.8	2.7
12:00	15.8	76.3	8.0
13:00	11.8	68.7	19.4
14:00	10.4	88.7	0.9
15:00	10.6	86.8	2.6
16:00	12.2	64.6	23.1

Table 4.3 As in Table 4.2, but for the IOP3 case.

IOP3 Case (6/06 0700 – 1900 Z)			
Time (UTC)	**Total Convection (DC + MC + SC, %)**	**Stratiform (ST, %)**	**Weak Echo (WE, %)**
08:00	12.6	52.6	28.3
09:00	11.8	84.4	3.7
10:00	9.1	81.0	9.9
11:00	9.7	56.3	28.3
15:00	7.4	49.4	39.5
16:00	12.1	40.6	47.0
17:00	14.4	74.4	10.5
18:00	11.0	12.7	55.5

doi:10.6342/NTU202504817

Table 4.4 Hourly fractions (%) of the deep convection, moderate convection, and shallow convection for the SOP1 case. The orange- and white-shaded portions denote the first and second episodes of enhanced surface precipitation, respectively.

SOP1 Case (5/25 0700 – 1900 Z)			
Time (UTC)	**Deep Convection (%)**	**Moderate Convection (%)**	**Shallow Convection (%)**
08:05	0.1	27.7	1.5
09:01	0.1	37.3	0.6
10:00	0	23.0	0.1
11:00	0	20.6	0
12:00	0	15.3	0.5
13:00	0	11.4	0.5
14:00	0.1	10.4	0
15:00	0	10.5	0.1
16:00	0	11.6	0.6

Table 4.5 As in Table 4.4, but for the IOP3 case.

IOP3 Case (6/06 0700 – 1900 Z)			
Time (UTC)	**Deep Convection (%)**	**Moderate Convection (%)**	**Shallow Convection (%)**
08:00	0.1	12.5	0
09:00	0	11.8	0
10:00	0	8.7	0.4
11:00	0	8.4	1.3
15:00	0	7.4	0
16:00	0	12.1	0
17:00	0	14.2	0.2
18:00	0	7.2	3.8

doi:10.6342/NTU202504817

Table 5.1 Summary of the key findings in this study. "Collision-coalescence" is abbreviated as "Collision".

Categories	Factors	SOP1 Case (5/25 0700 – 1900 Z)	IOP3 Case (6/06 0700 – 1900 Z)
Precipitation Feature	12-hr Accumulated Rainfall	Greater	Less
Synoptic Insights	Frontal Slope	Gentler	Steeper
	Frontal Intensity	Weaker	Stronger
	Wind Speed / Specific Humidity / Moisture Transport	Only superior in specific humidity and TPW	Superior in wind speed and moisture transport
Thermodynamic Insights	Vertical Profile of Humidity	Very humid throughout mid- to low-levels	Clear mid- to low-level dry regions at the beginning
Kinematic Insights	Low-Level Convergence Zones	Persistent low-level convergence zones offshore	Fewer distinct low-level convergence zones offshore
Cloud Microphysical Insights	Precipitation-Contributing Regimes	Convective ↓ Stratiform	Stratiform ↓ Stratiform & Weak echo
	Moderate & Heavy Rain Fraction	Higher	Lower
	Overall Updraft Strength	Stronger	Weaker
	Dominant Warm-Rain Microphysical Processes	Pronounced collision	Evaporation ↓ Weak collision ↓ Evaporation & Weak collision
	Raindrop Size (Z_{DR})	Mid- to small-sized drops dominant	Mid- to small-sized drops dominant
	Liquid Water Content / Raindrop Number Concentration (K_{DP})	Greater	Less

doi:10.6342/NTU202504817

Figures

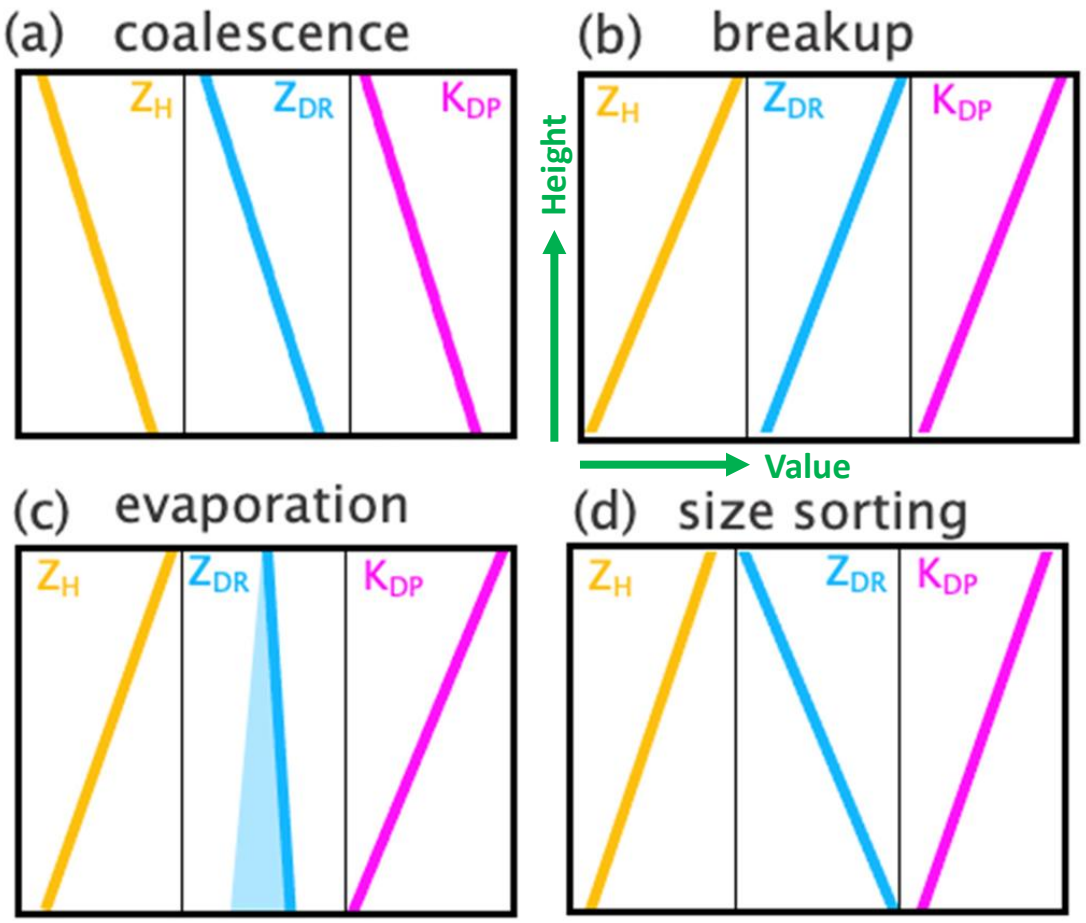

Figure 1.1 Different microphysical fingerprints for liquid-phase precipitation, including (a) coalescence, (b) breakup, (c) evaporation, and (d) size sorting. The lighter cyan shading in (c) indicates a range of possible fingerprints for Z_{DR}. The value of each polarimetric parameter is on the horizontal axis, increasing rightward, whereas height is on the vertical axis, increasing upward. (Kumjian et al. 2022)

doi:10.6342/NTU202504817

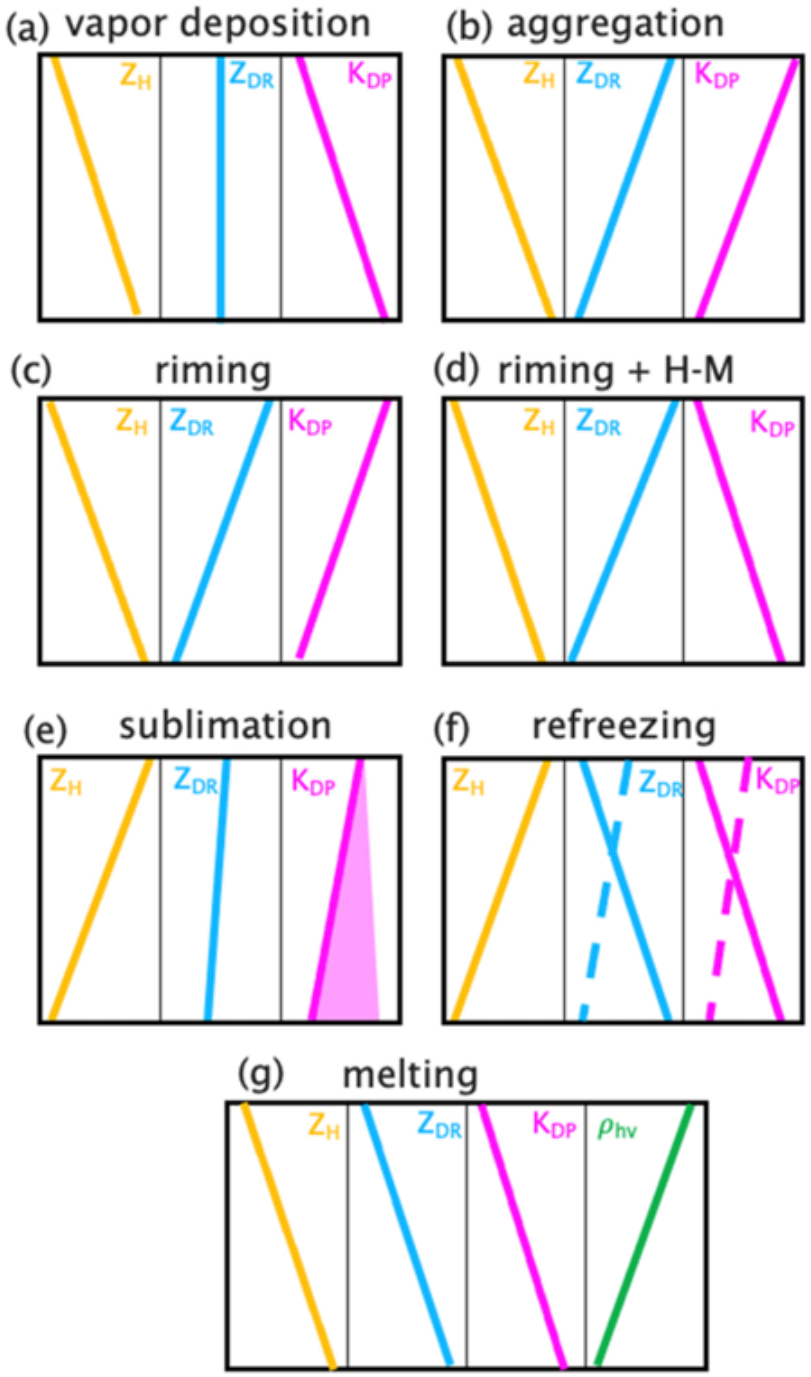

Figure 1.2 As in Figure 1.1, but for ice-phase precipitation including (a) vapor depositional growth of ice crystals, (b) aggregation, (c) riming, (d) riming with the Hallett-Mossop rime splintering process occurring, (e) sublimation, (f) refreezing, and (g) melting. The purple shading in (e) indicates a range of possible fingerprints for K_{DP}. The dashed and solid lines in (f) show the refreezing of partially and fully melted hydrometeors, respectively. (Kumjian et al. 2022)

doi:10.6342/NTU202504817

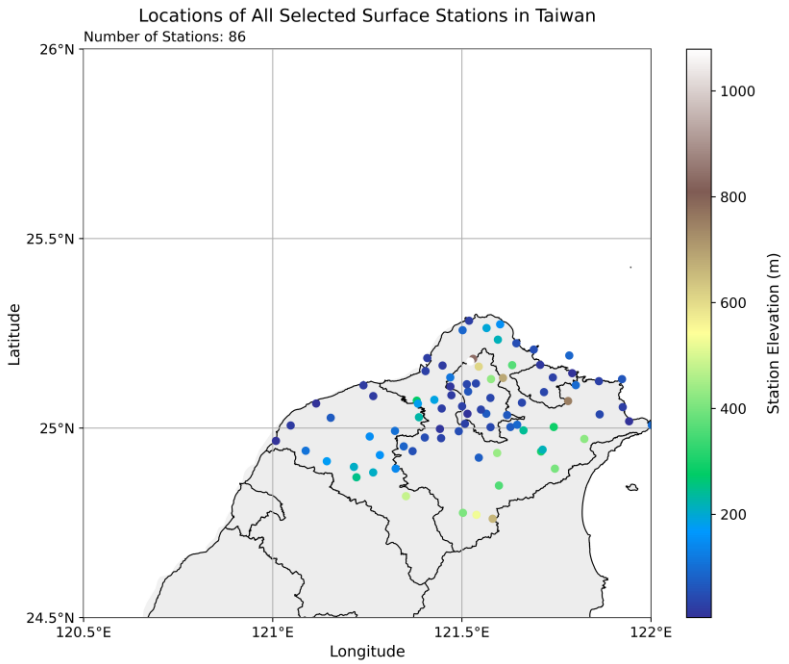

Figure 2.1 Locations of the 86 surface stations used to analyze precipitation features in the two Meiyu front cases. Dot color indicates station elevation.

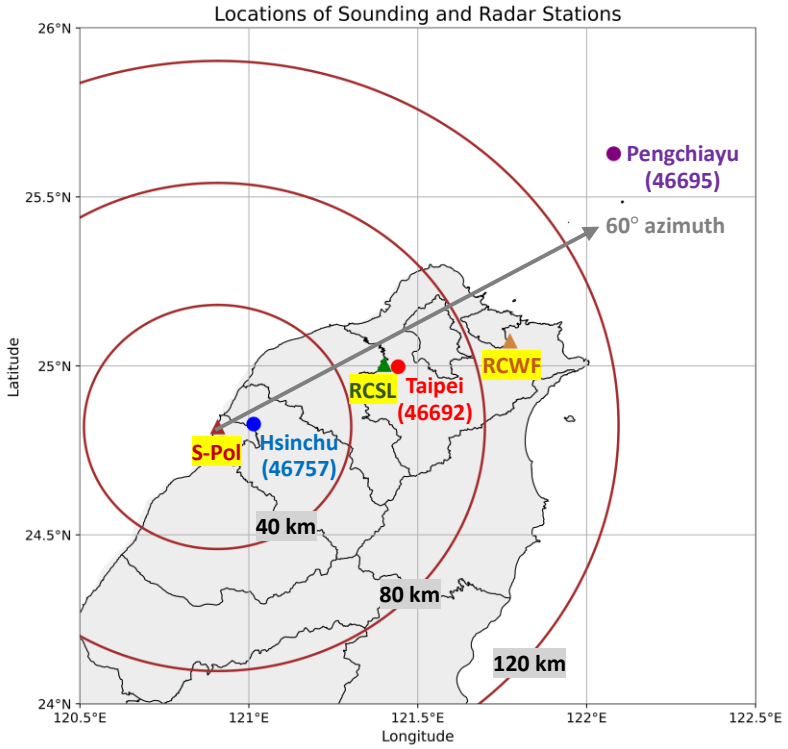

Figure 2.2 Locations of sounding and radar stations. Azimuth is measured following the meteorological convention, with 0° denoting true north and increasing clockwise.

doi:10.6342/NTU202504817

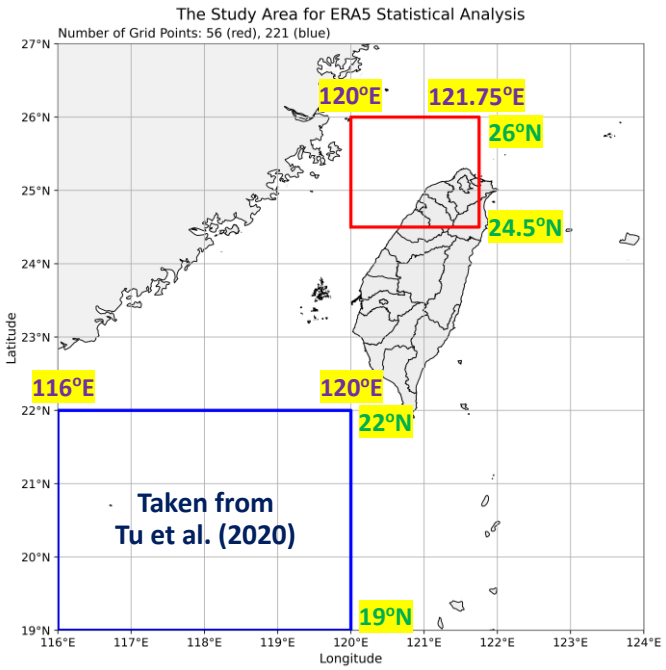

Figure 2.3 The study area for statistical analysis of the synoptic environment. The red rectangle indicates the region used for analyzing the barrier jet and integrated vapor transport (IVT) divergence, while the blue rectangle denotes the region where other thermodynamic and kinematic parameters are examined.

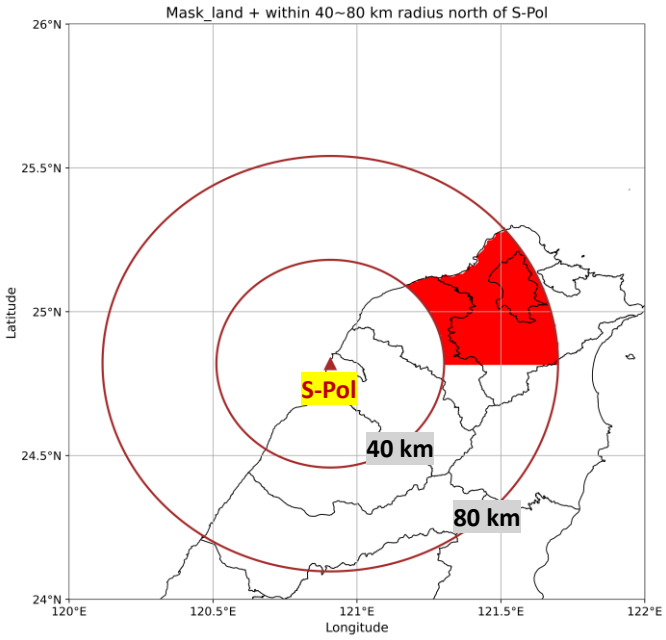

Figure 2.4 The study area for the analysis of cloud microphysical characteristics (indicated by the red color shading).

doi:10.6342/NTU202504817

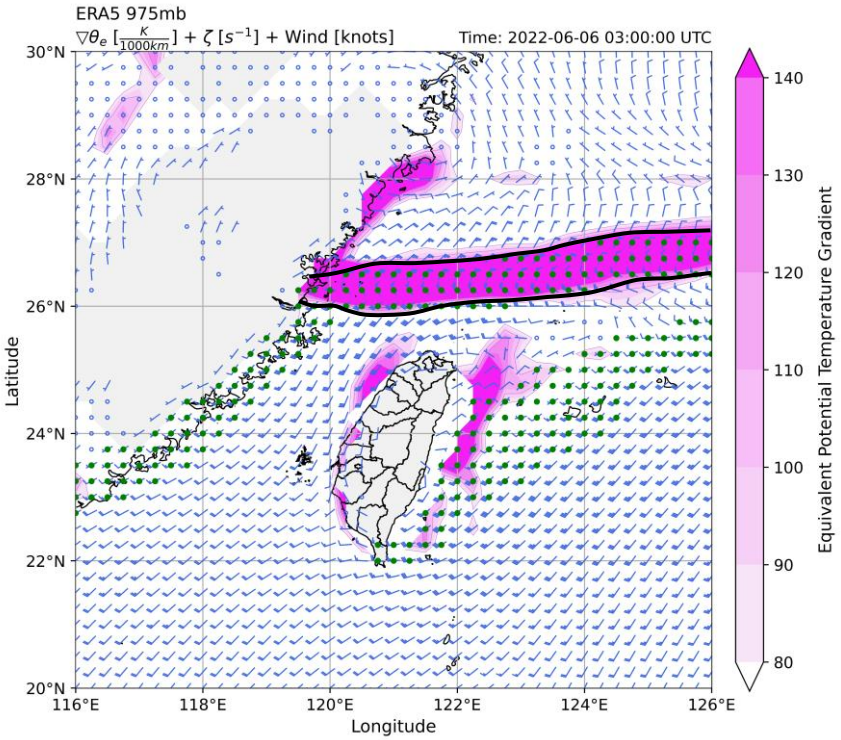

Figure 2.5 Schematic of 975-hPa Meiyu front identification based on adopted criteria, shown for 6/06 0300 Z. Only the region enclosed by the two black lines is identified as the Meiyu front. Color shading indicates horizontal θ_e gradient (K/1000 km), and green dots mark locations with relative vorticity > 5×10^{-5} s^{-1}.

doi:10.6342/NTU202504817

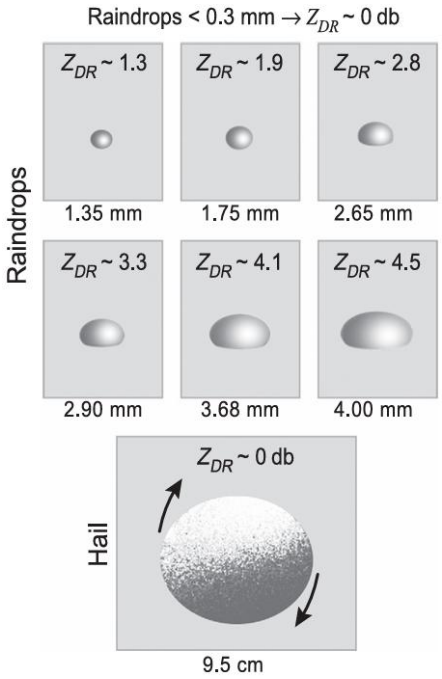

Figure 2.6 Typical Z_{DR} values for raindrops of various sizes and hail. Black arrows beside the hail particle represent spinning and tumbling motions. (Wakimoto and Bringi 1988; Houze 2014)

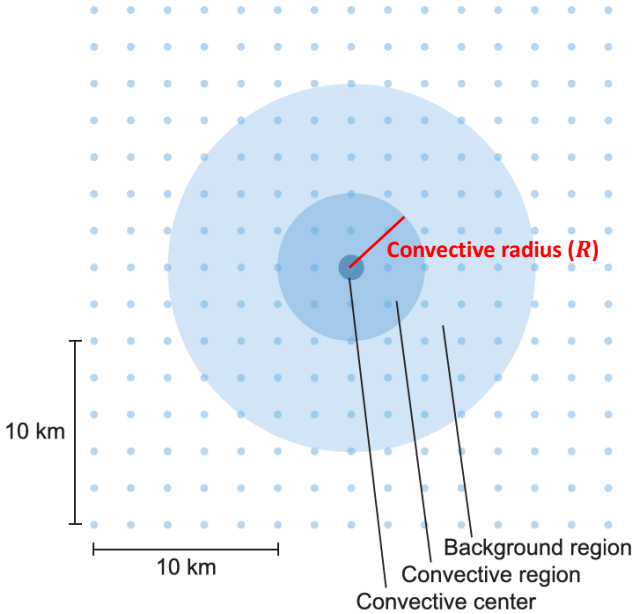

Figure 2.7 Schematic illustration of the spatial relationship among a convective center, its background region, and the resulting convective precipitation regime. (Steiner et al. 1995; Houze 2014)

doi:10.6342/NTU202504817

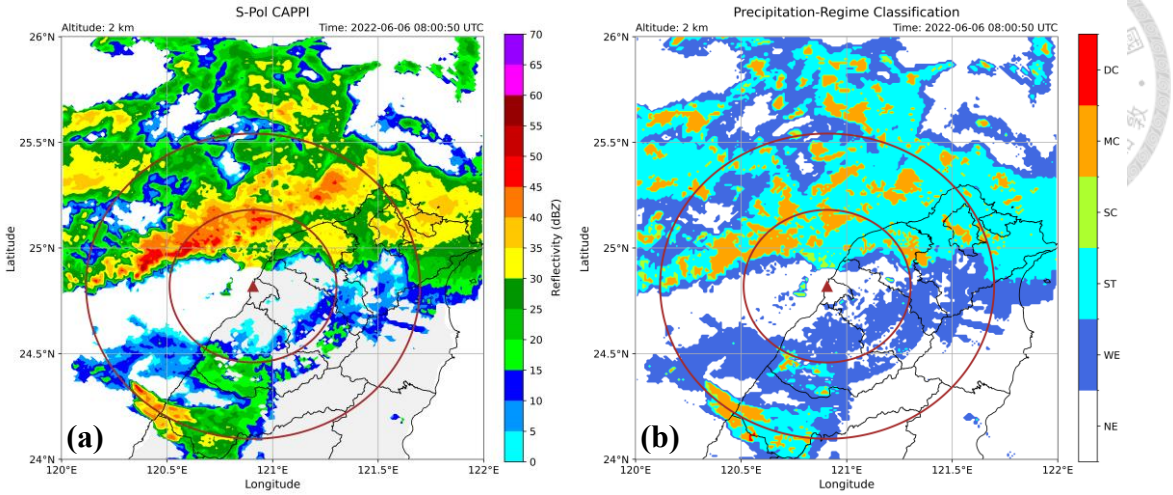

Figure 2.8 An example of the output from the convective-stratiform separation algorithm at 6/06 0800 Z. (a) S-Pol radar reflectivity at 2-km height. (b) Corresponding classification result.

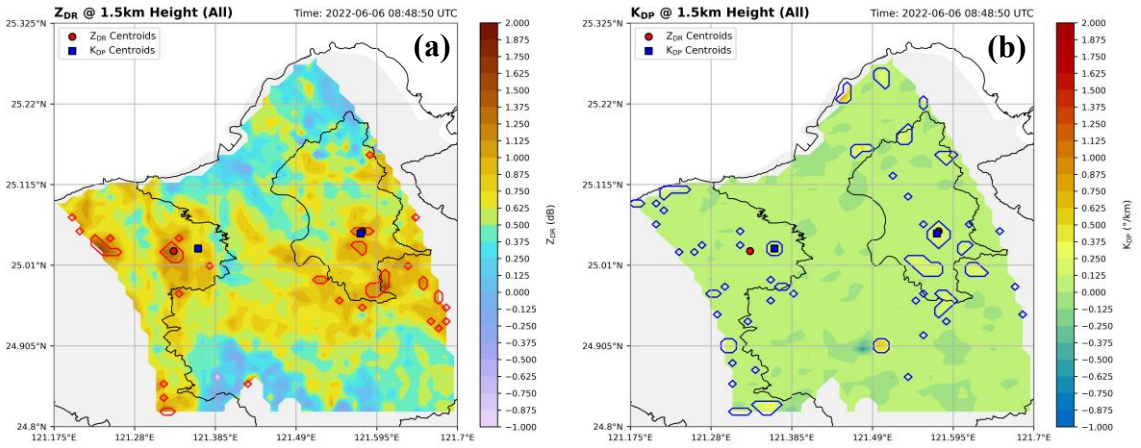

Figure 2.9 An example of size sorting object identification at 6/06 0848 Z. Background colors show radar observations of (a) Z_{DR} and (b) K_{DP} at 1.5-km height. Red and blue contours indicate regions where Z_{DR} and K_{DP} values exceed the magnitude thresholds, respectively. For contour objects that also satisfy the size thresholds and are considered valid pairings, the centroids of Z_{DR} and K_{DP} objects are marked with red circles and blue squares, respectively.

doi:10.6342/NTU202504817

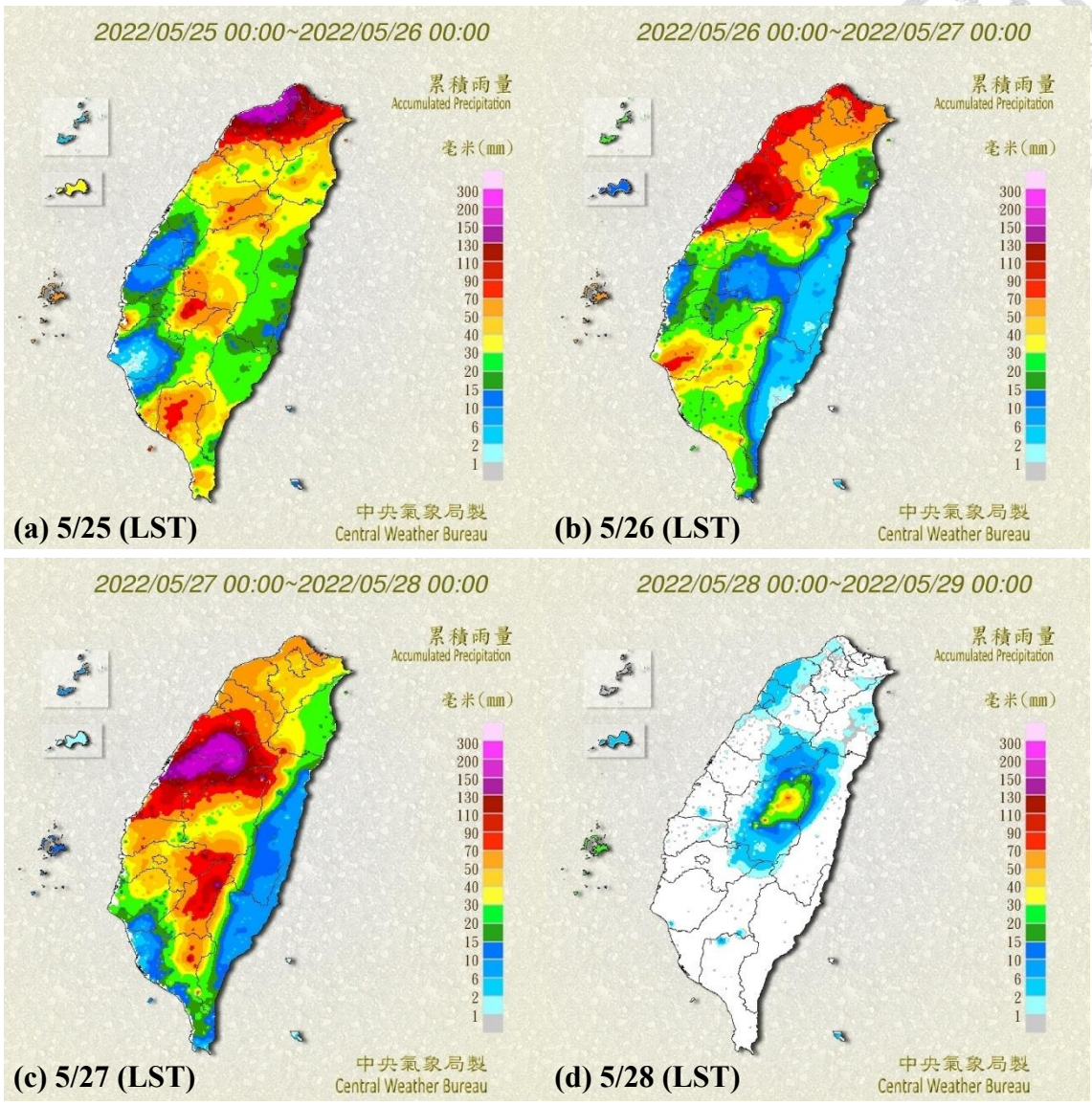

Figure 3.1 CWB daily accumulated rainfall maps for (a) 5/25 LST, (b) 5/26 LST, (c) 5/27 LST, and (d) 5/28 LST. Source: Central Weather Bureau (CWB).

doi:10.6342/NTU202504817

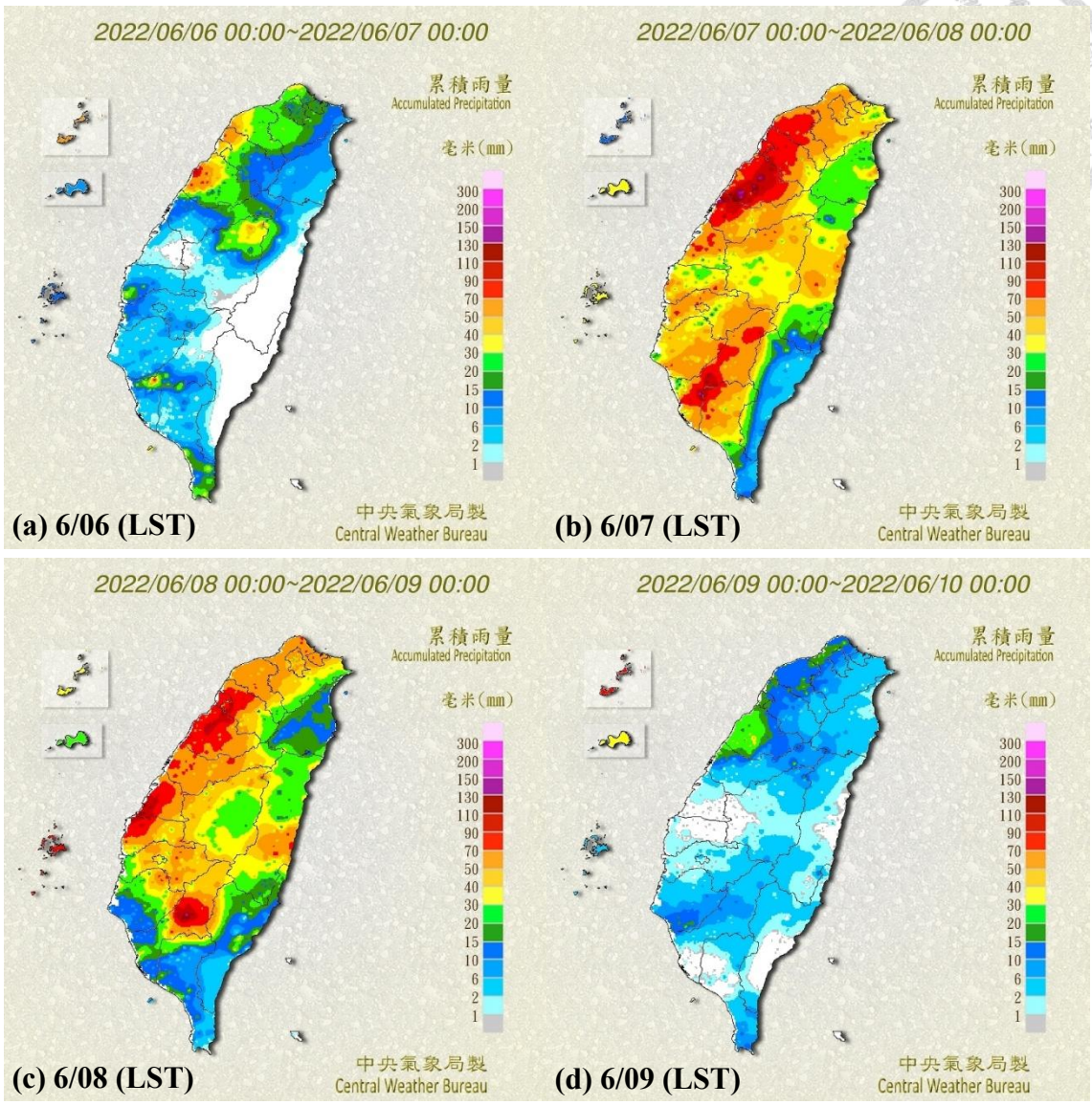

Figure 3.2 As in Figure 3.1, but for (a) 6/06 LST, (b) 6/07 LST, (c) 6/08 LST, and (d) 6/09 LST. Source: Central Weather Bureau (CWB).

doi:10.6342/NTU202504817

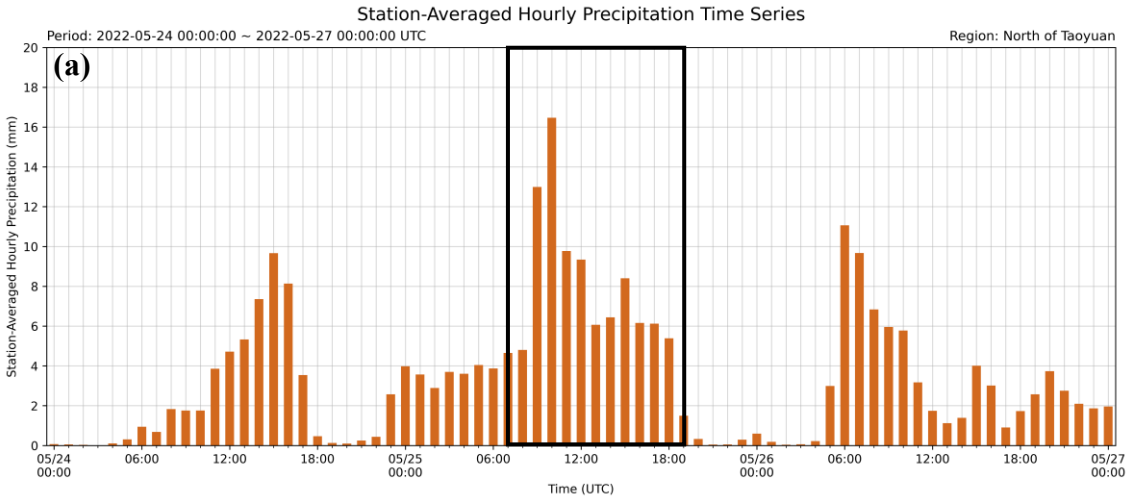

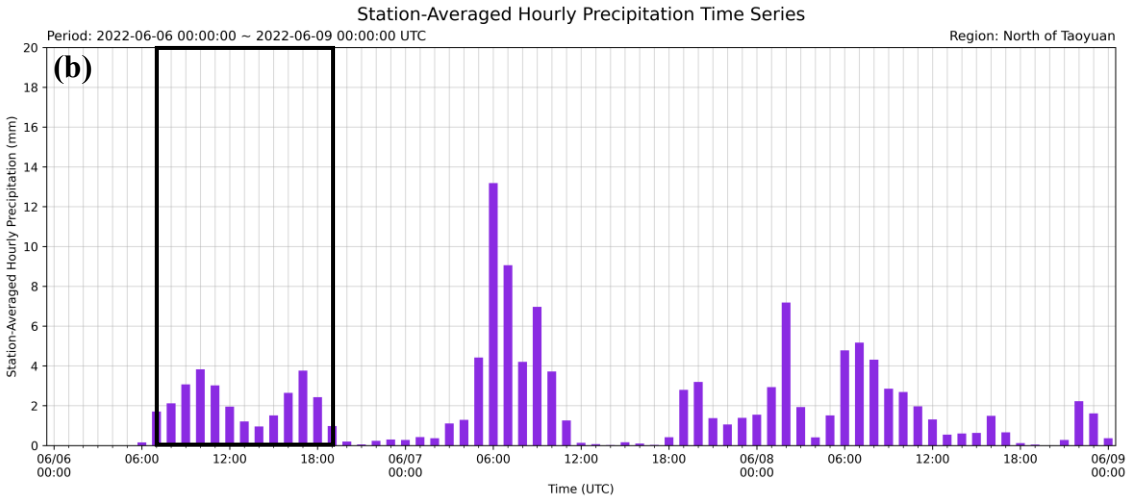

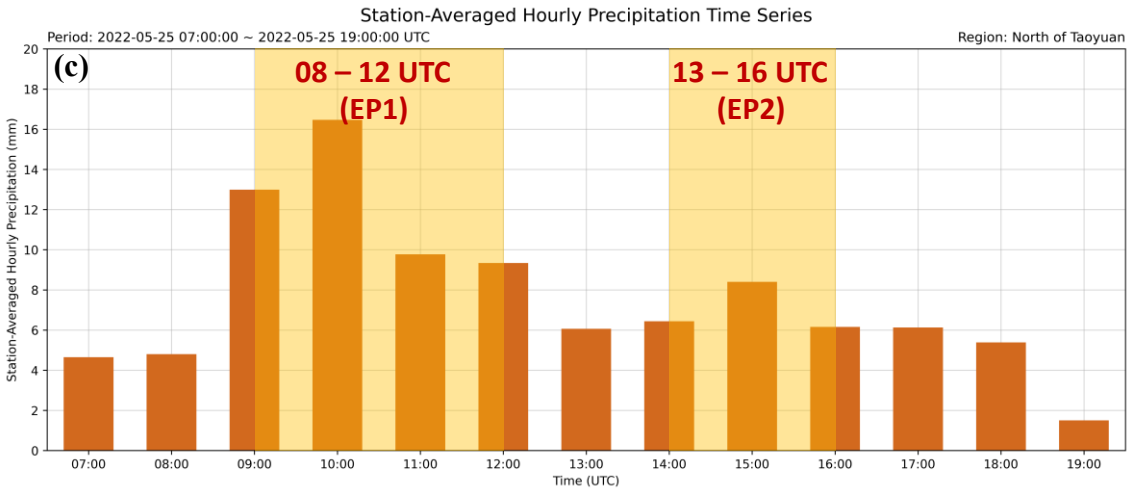

doi:10.6342/NTU202504817

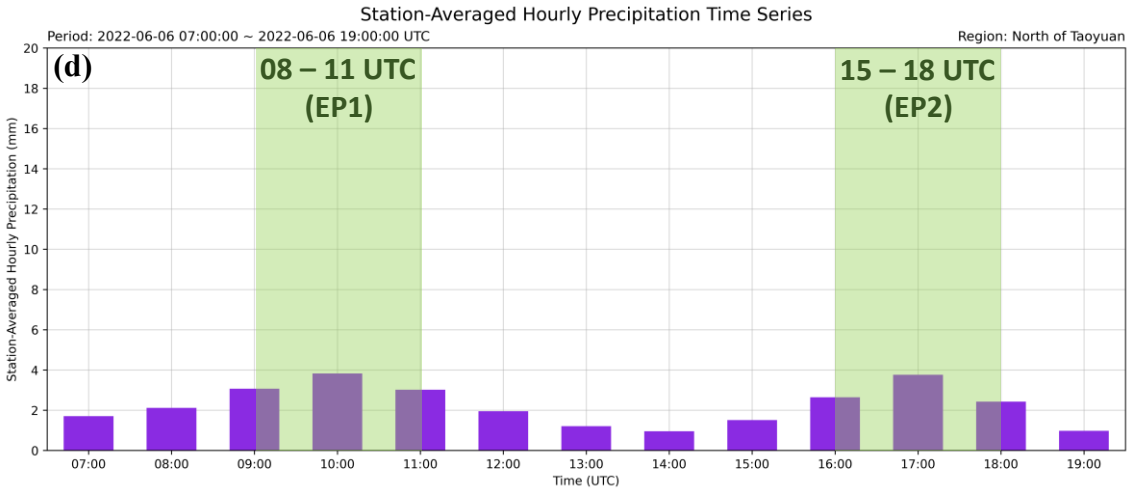

Figure 3.3 Hourly accumulated precipitation averaged over the 86 surface stations located in and north of Taoyuan during (a) 5/24 0000 Z–5/27 0000 Z, (b) 6/06 0000 Z–6/09 0000 Z, (c) 5/25 0700–1900 Z, and (d) 6/06 0700–1900 Z. Black boxes in (a) and (b) mark the two 12-hour periods analyzed, whose time series are shown in (c) and (d), with color shading highlighting two episodes of enhanced surface precipitation.

(a) 5/25 0700–1900 Z **(b) 6/06 0700–1900 Z**

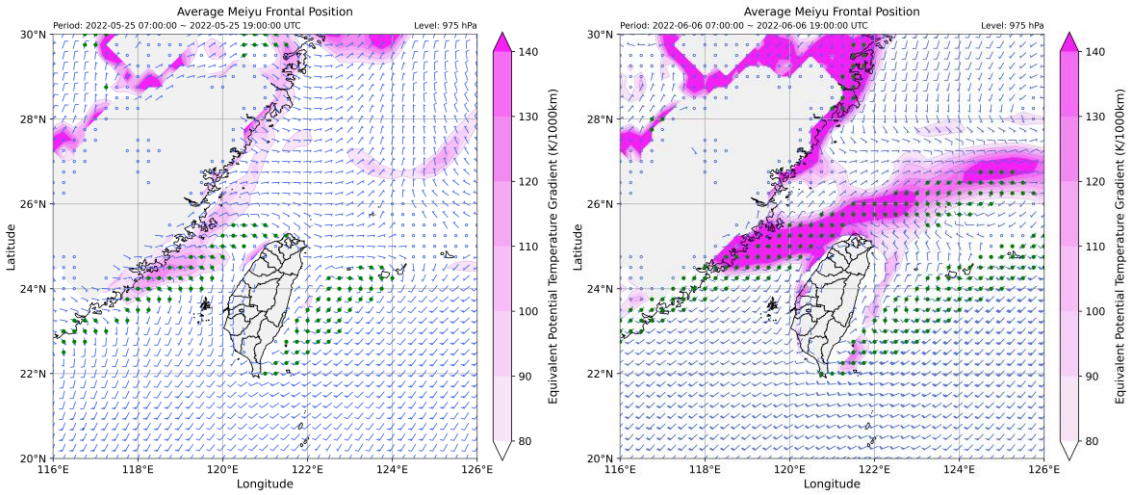

Figure 3.4 The average position of the Meiyu front at the 975-hPa level during (a) 5/25 0700–1900 Z (SOP1 case) and (b) 6/06 0700–1900 Z (IOP3 case). Color shading indicates horizontal θ_e gradient (K/1000 km), and green dots mark locations with relative vorticity > 5×10^{-5} s^{-1}.

doi:10.6342/NTU202504817

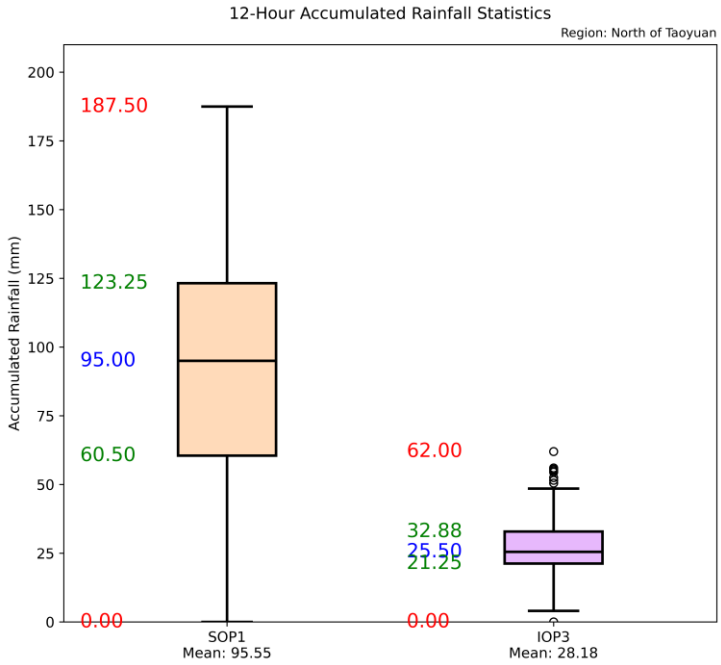

Figure 3.5 12-hour accumulated rainfall statistics over the 86 surface stations in and north of Taoyuan during 5/25 0700–1900 Z (SOP1 case) and 6/06 0700–1900 Z (IOP3 case). For each boxplot, the five numbers from bottom to top on the left-hand side correspond to the minimum, first quartile, median (second quartile), third quartile, and maximum.

(a) 5/25 0700–1900 Z **(b) 6/06 0700–1900 Z**

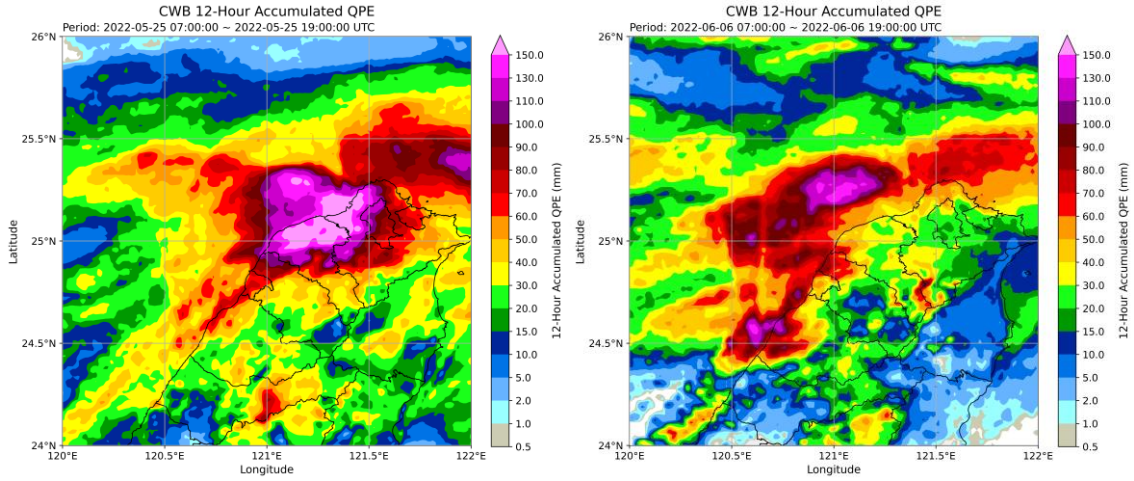

Figure 3.6 12-hour accumulated quantitative precipitation estimation (QPE) during (a) 5/25 0700–1900 Z (SOP1 case) and (b) 6/06 0700–1900 Z (IOP3 case).

doi:10.6342/NTU202504817

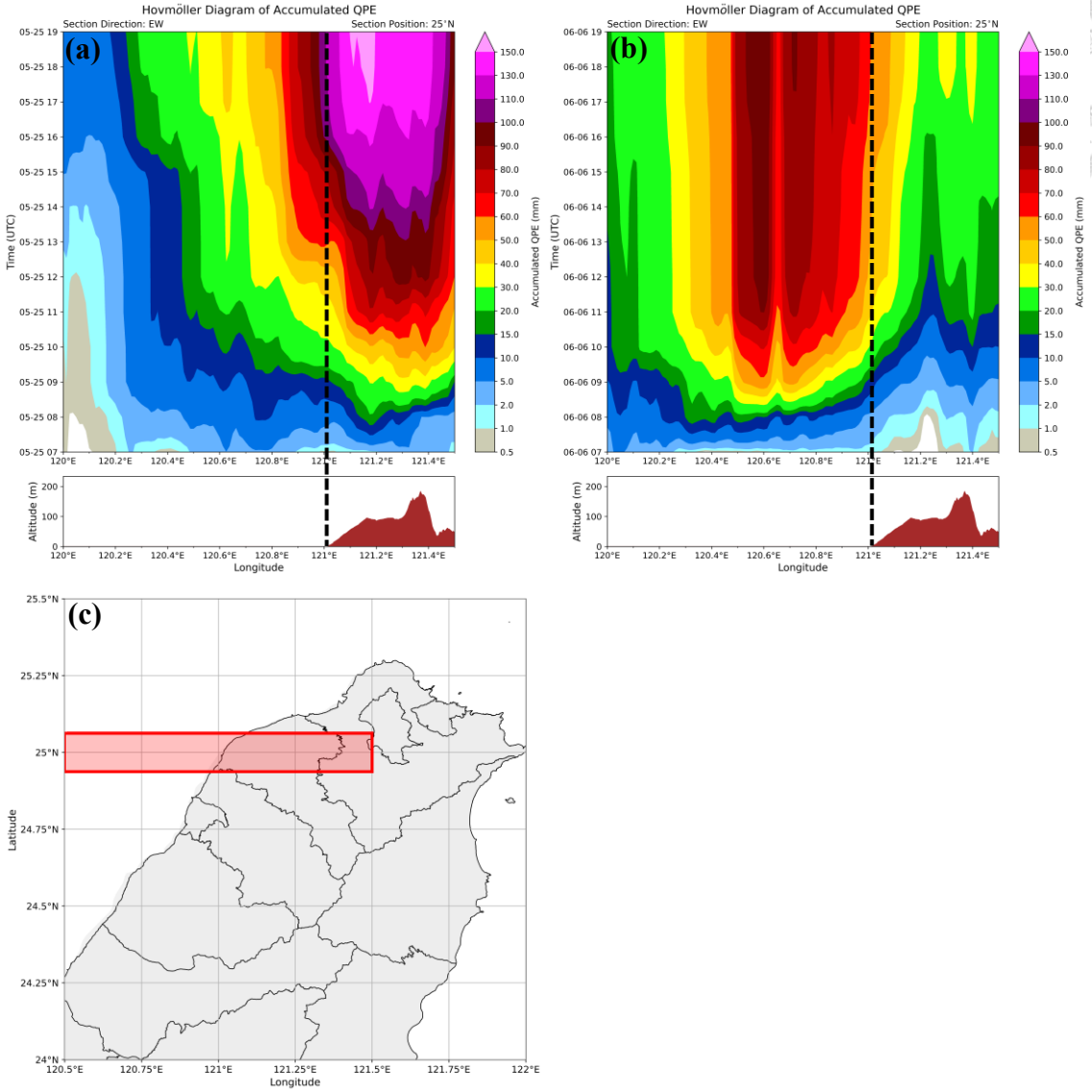

Figure 3.7 The Hovmöller diagrams of 12-hour accumulated QPE along the east-west cross-section at 25°N for (a) 5/25 0700–1900 Z (SOP1 case) and (b) 6/06 0700–1900 Z (IOP3 case). In each panel, the values were averaged over a 0.0625° (≈15 km) meridional band, indicated by the red box in (c). Furthermore, the thick black dashed lines in (a) and (b) represent the location of the coast, with the terrain profile displayed at the bottom of both panels.

doi:10.6342/NTU202504817

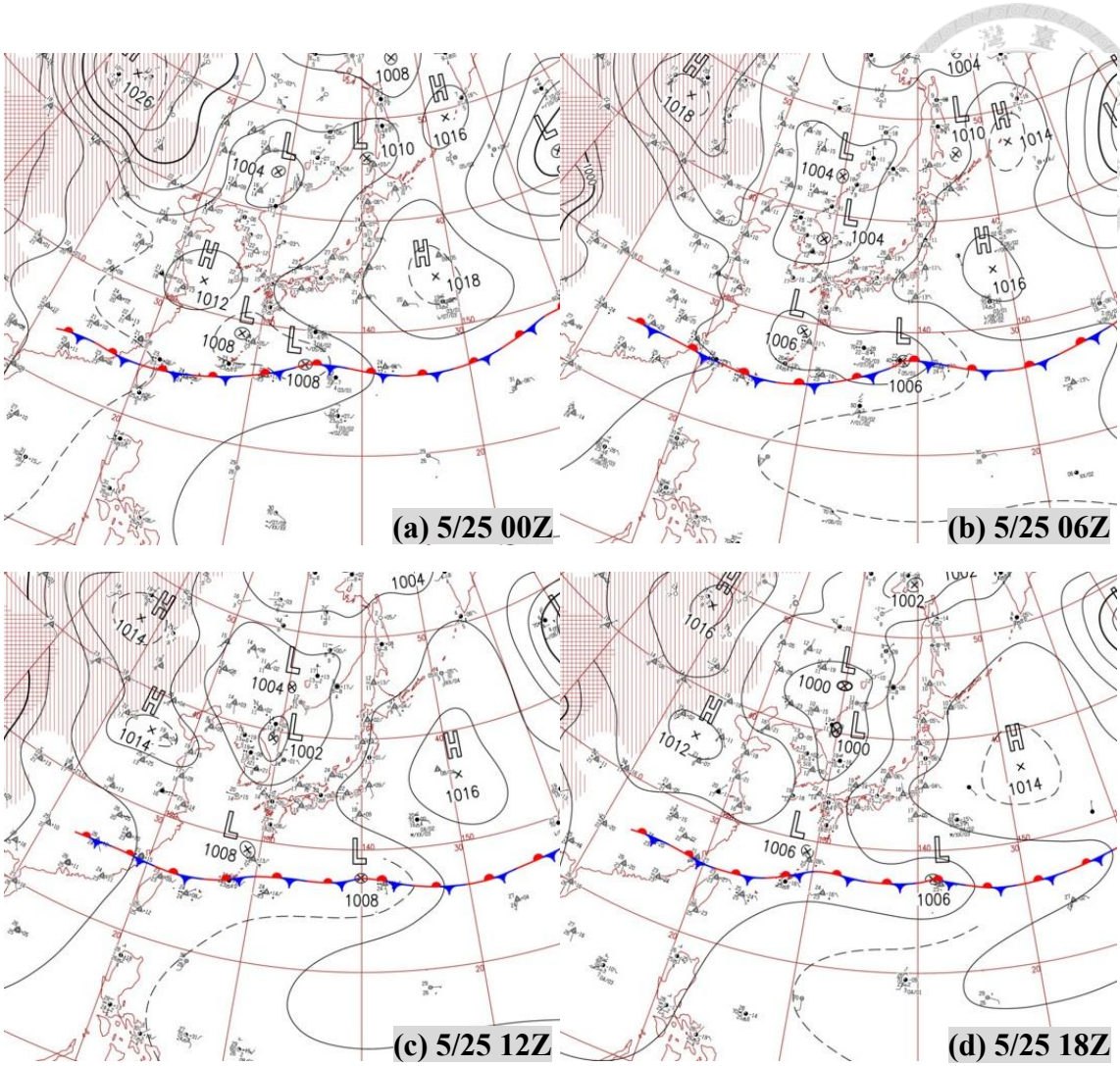

Figure 4.1 JMA surface weather charts for (a) 5/25 0000 Z, (b) 5/25 0600 Z, (c) 5/25 1200 Z, and (d) 5/25 1800 Z. Source: Japan Meteorological Agency (JMA).

doi:10.6342/NTU202504817

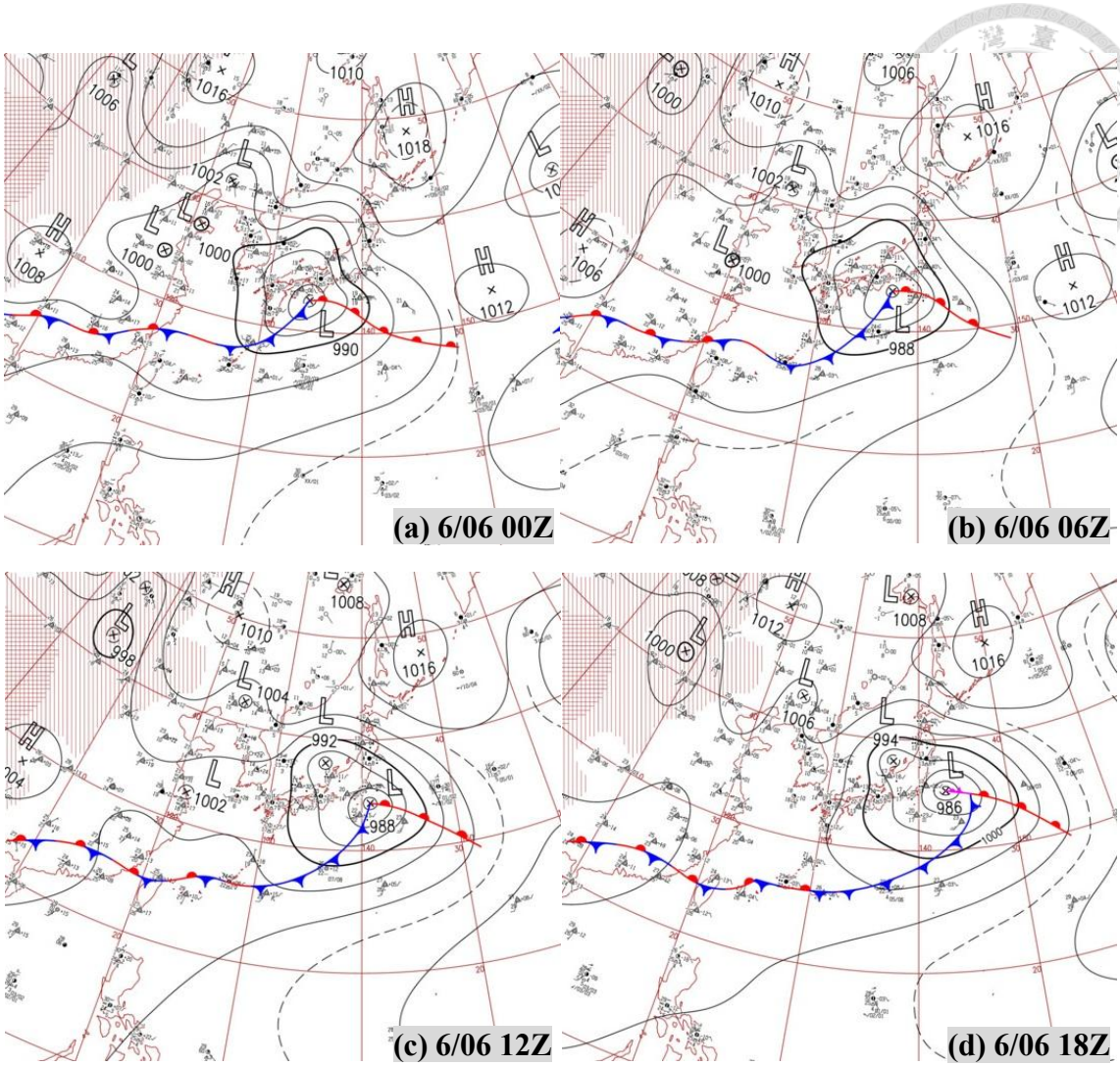

Figure 4.2 As in Figure 4.1, but for (a) 6/06 0000 Z, (b) 6/06 0600 Z, (c) 6/06 1200 Z, and (d) 6/06 1800 Z. Source: Japan Meteorological Agency (JMA).

doi:10.6342/NTU202504817

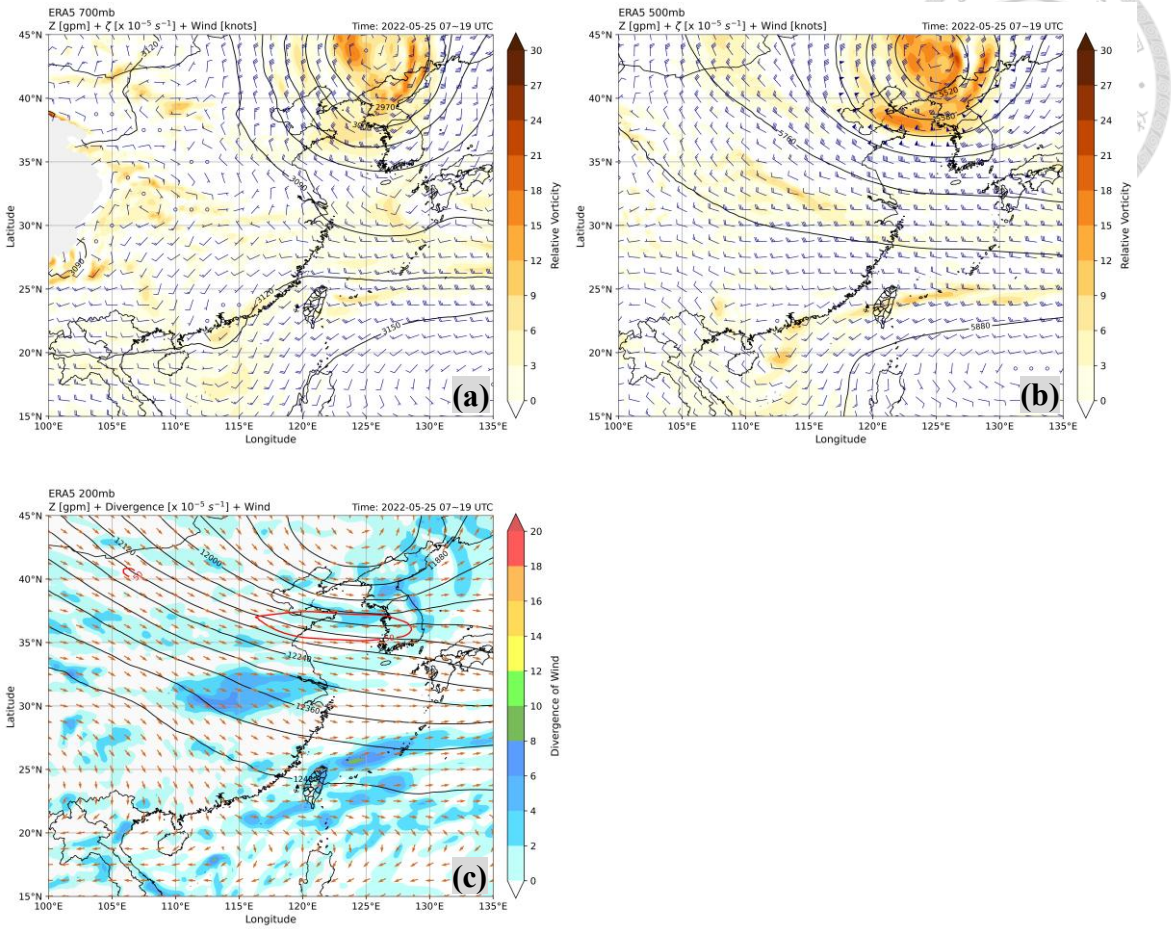

Figure 4.3 12-hour averaged weather charts at (a) 700 hPa, (b) 500 hPa, and (c) 200 hPa for the SOP1 case. Black contours denote geopotential height (gpm). In panels (a) and (b), color shading indicates relative vorticity (10^{-5} s^{-1}) and wind barbs show horizontal winds (knots). In panel (c), color shading represents divergence (10^{-5} s^{-1}), arrows denote horizontal wind direction, and red contours mark the isotach of 50 m s^{-1}, highlighting the approximate location of the upper-level jet stream.

doi:10.6342/NTU202504817

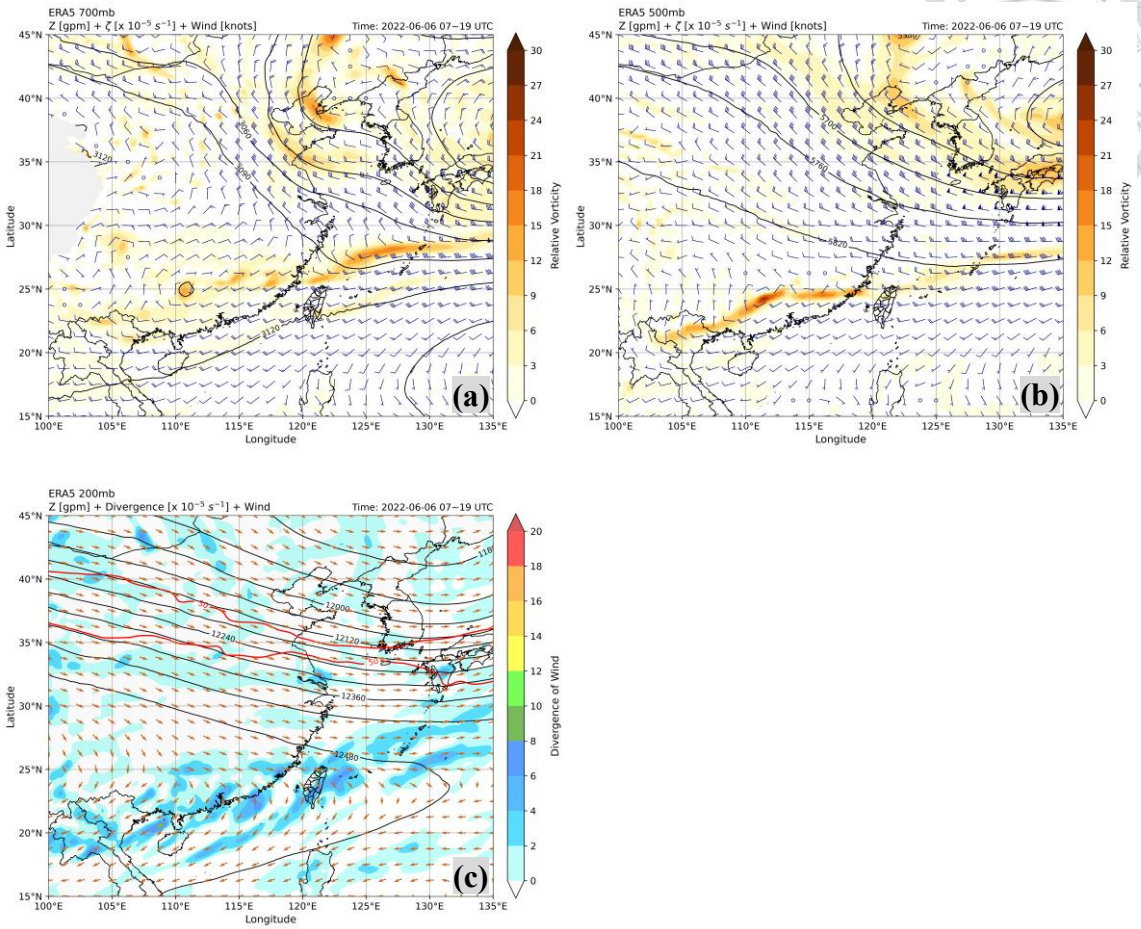

Figure 4.4 As in Figure 4.3, but for the IOP3 case.

doi:10.6342/NTU202504817

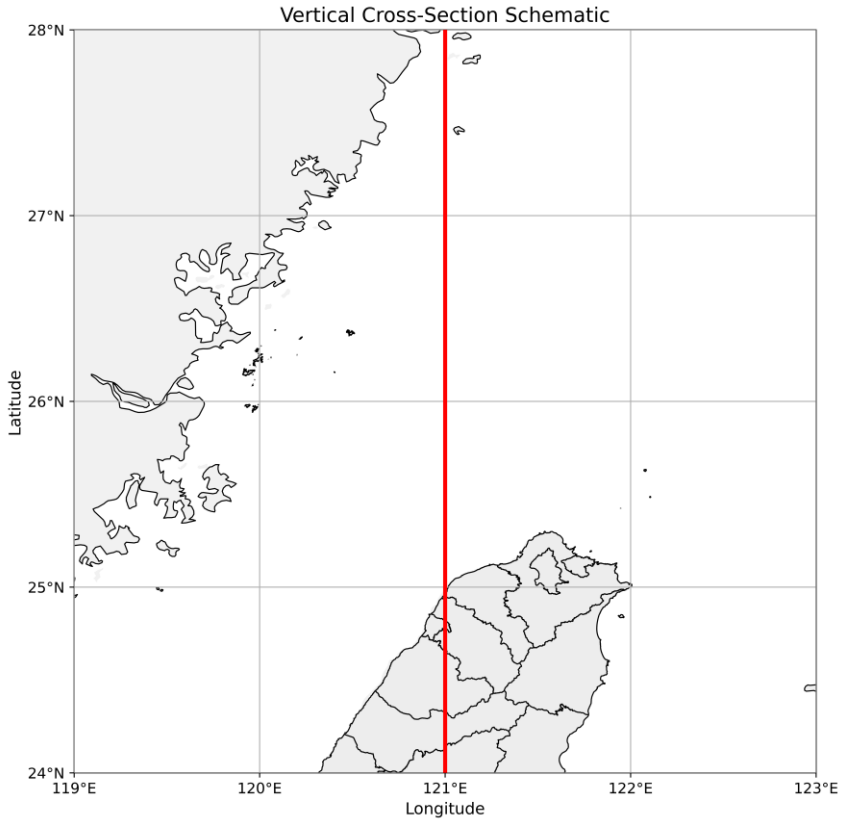

Figure 4.5 Schematic of the north-south cross section at 121°E, extending from 24°N to 28°N (red line).

doi:10.6342/NTU202504817

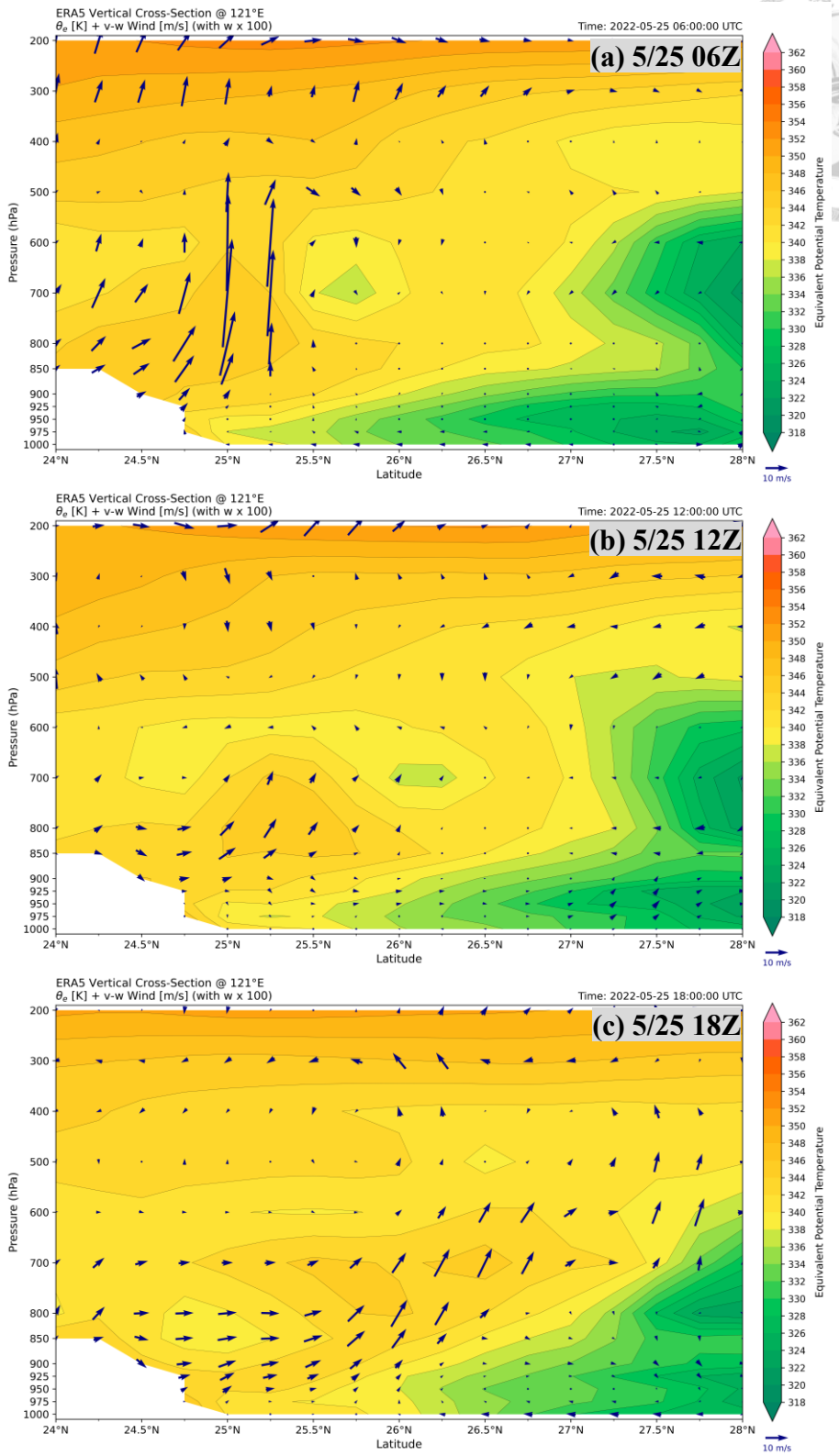

Figure 4.6 Vertical cross-section of θ_e (color shading; K) and v-w wind (arrows; m s^{-1}, with vertical velocity multiplied by 100) along the north-south section shown in Figure 4.5, for the SOP1 case at (a) 0600 Z, (b) 1200 Z, and (c) 1800 Z.

doi:10.6342/NTU202504817

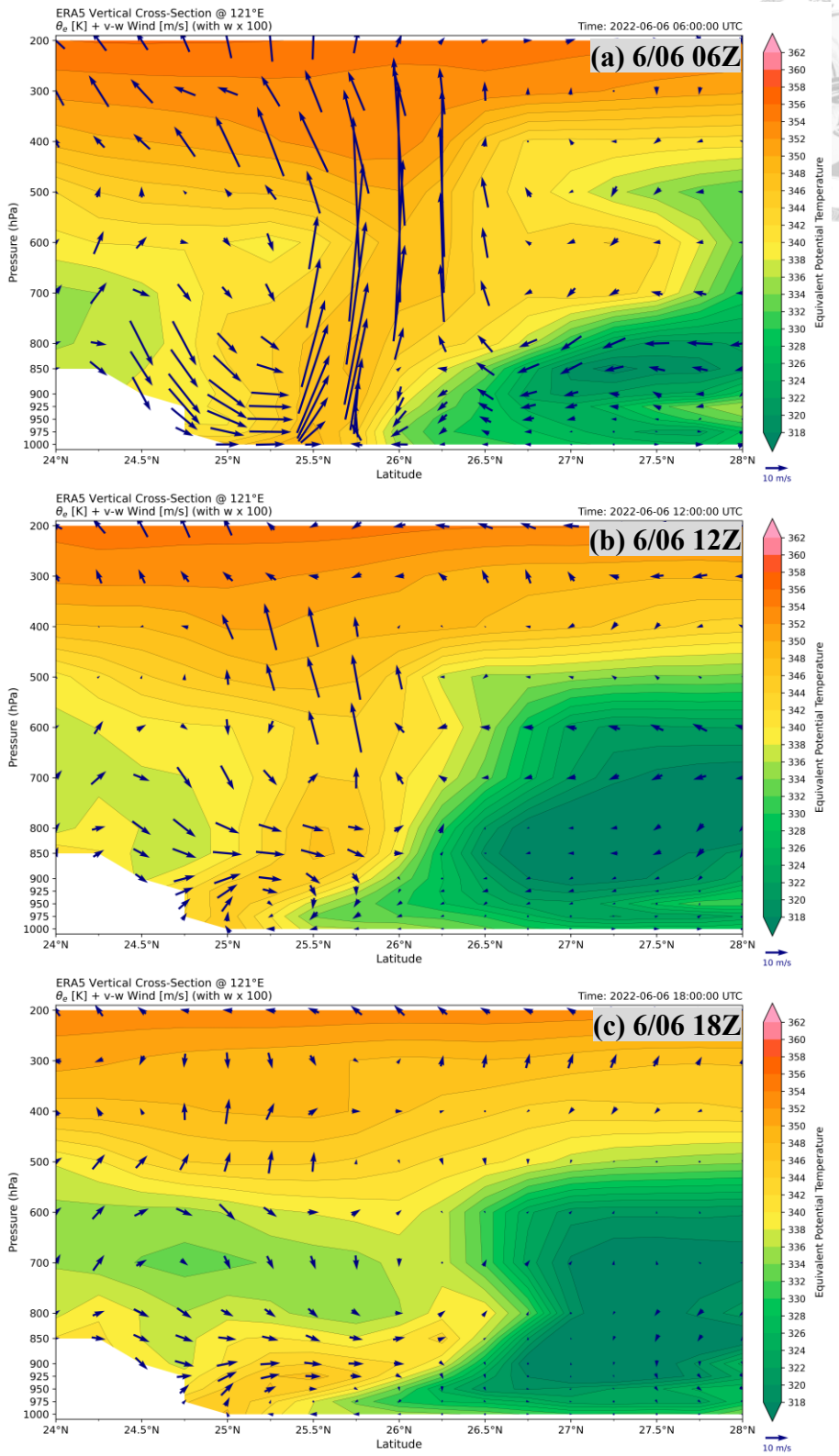

Figure 4.7 As in Figure 4.6, but for the IOP3 case at (a) 0600 Z, (b) 1200 Z, and (c) 1800 Z.

doi:10.6342/NTU202504817

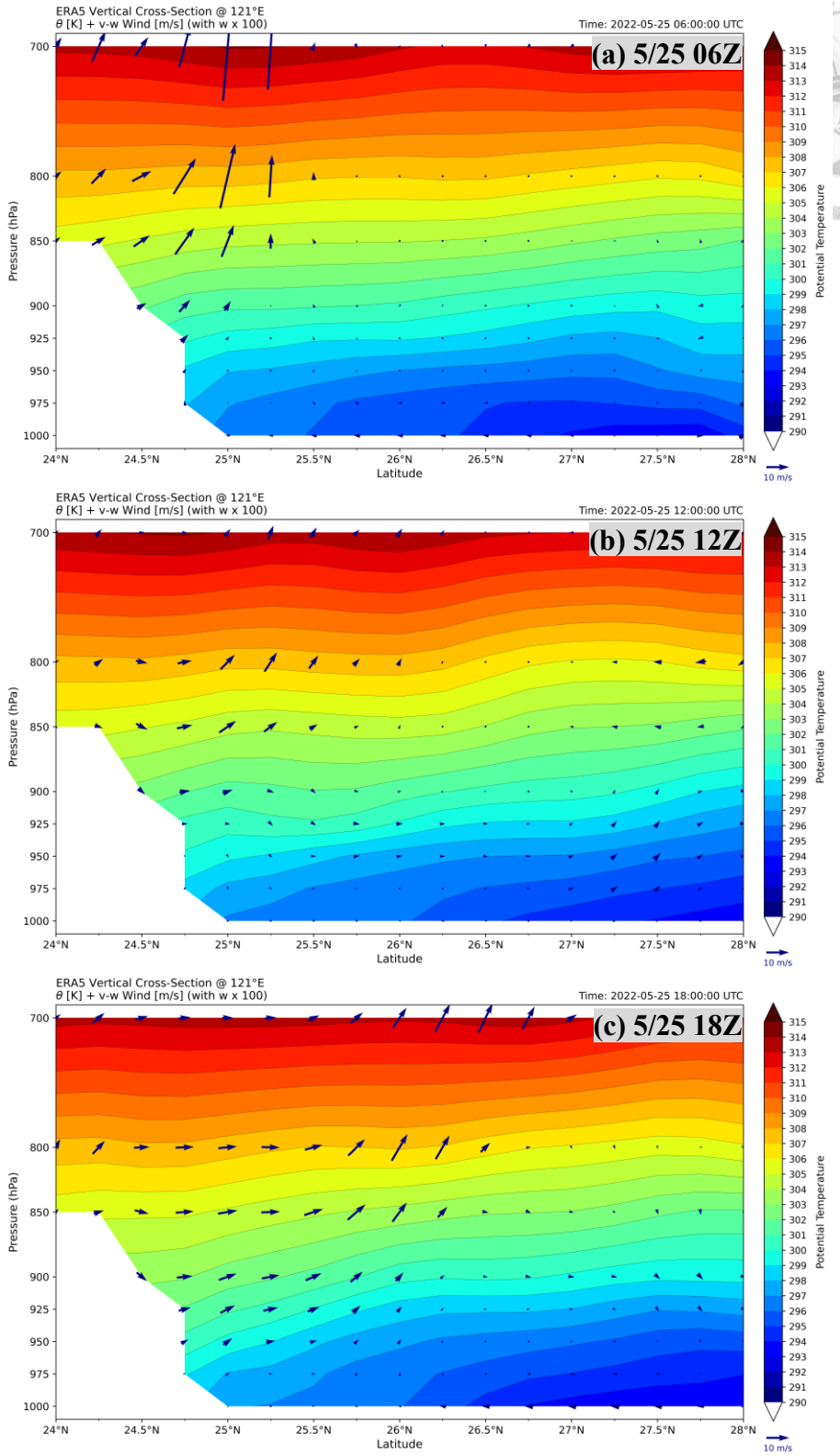

Figure 4.8 Vertical cross-section of θ (color shading; K) and v-w wind (arrows; m s^{-1}, with vertical velocity multiplied by 100) along the north-south section shown in Figure 4.5, for the SOP1 case at (a) 0600 Z, (b) 1200 Z, and (c) 1800 Z.

doi:10.6342/NTU202504817

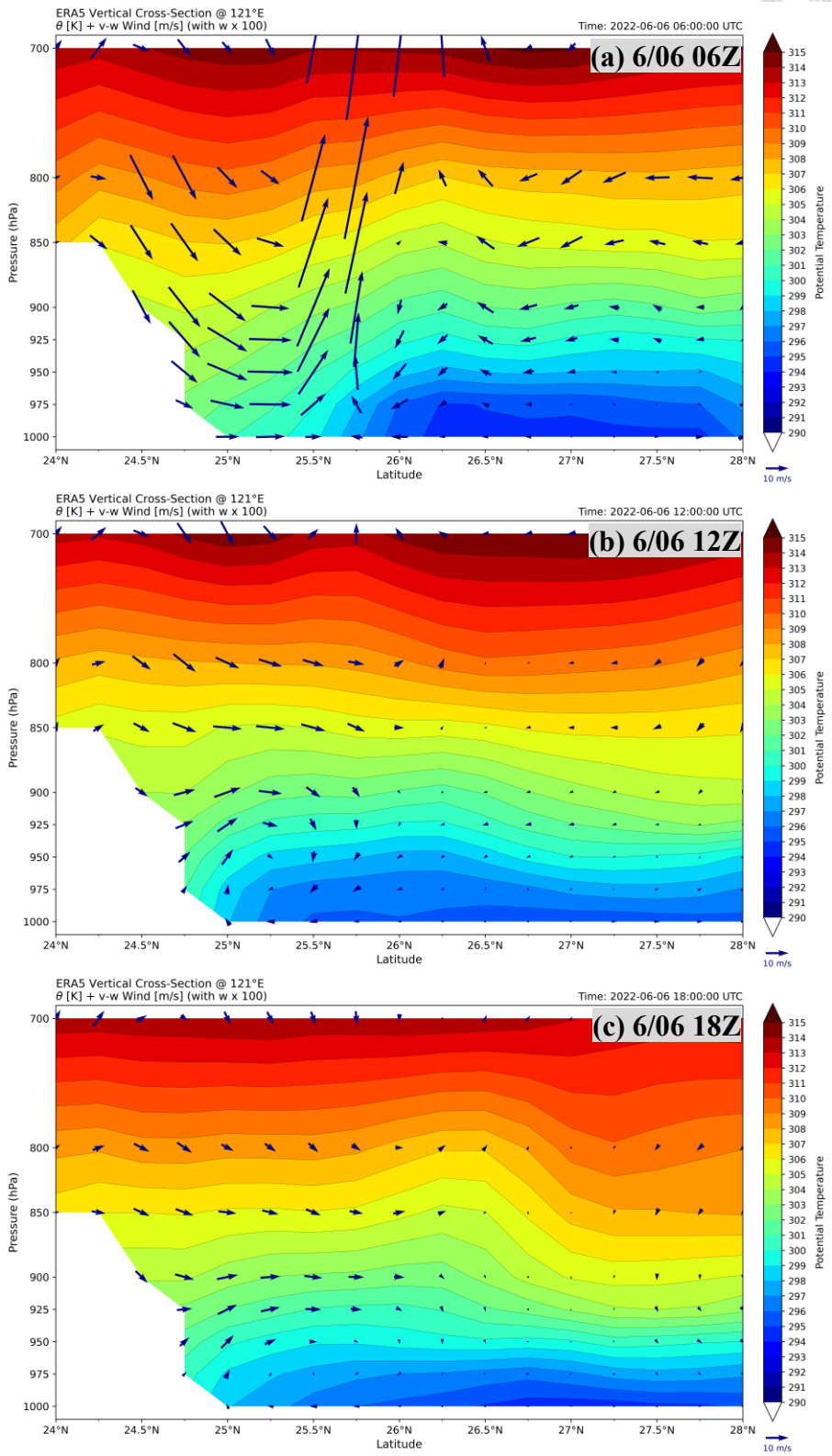

Figure 4.9 As in Figure 4.8, but for the IOP3 case at (a) 0600 Z, (b) 1200 Z, and (c) 1800 Z.

doi:10.6342/NTU202504817

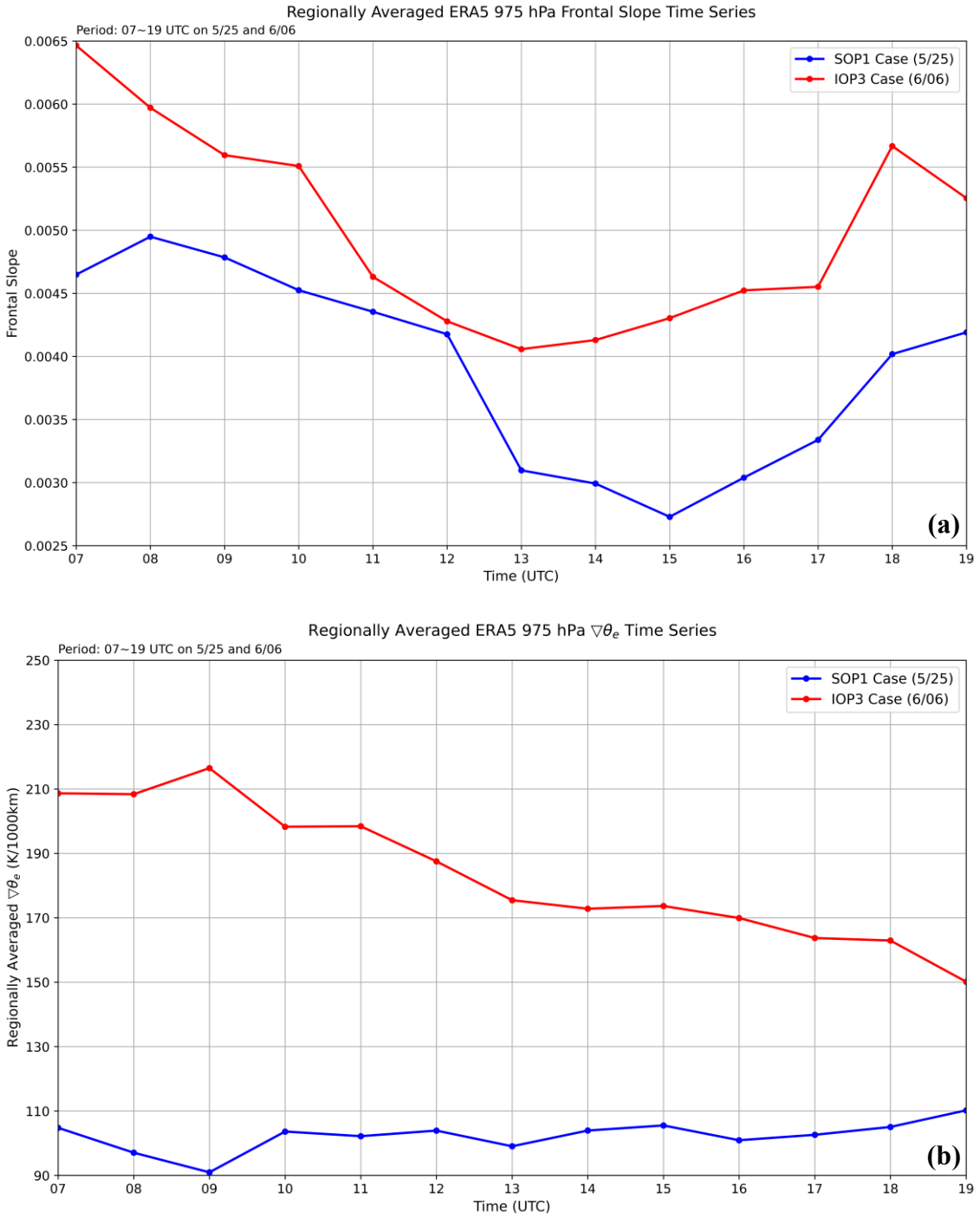

Figure 4.10 Time series of the regionally averaged (a) frontal slope and (b) horizontal θ_e gradient (K/1000km; indicator of frontal intensity) at the 975-hPa level for the SOP1 case (blue line) and the IOP3 case (red line).

doi:10.6342/NTU202504817

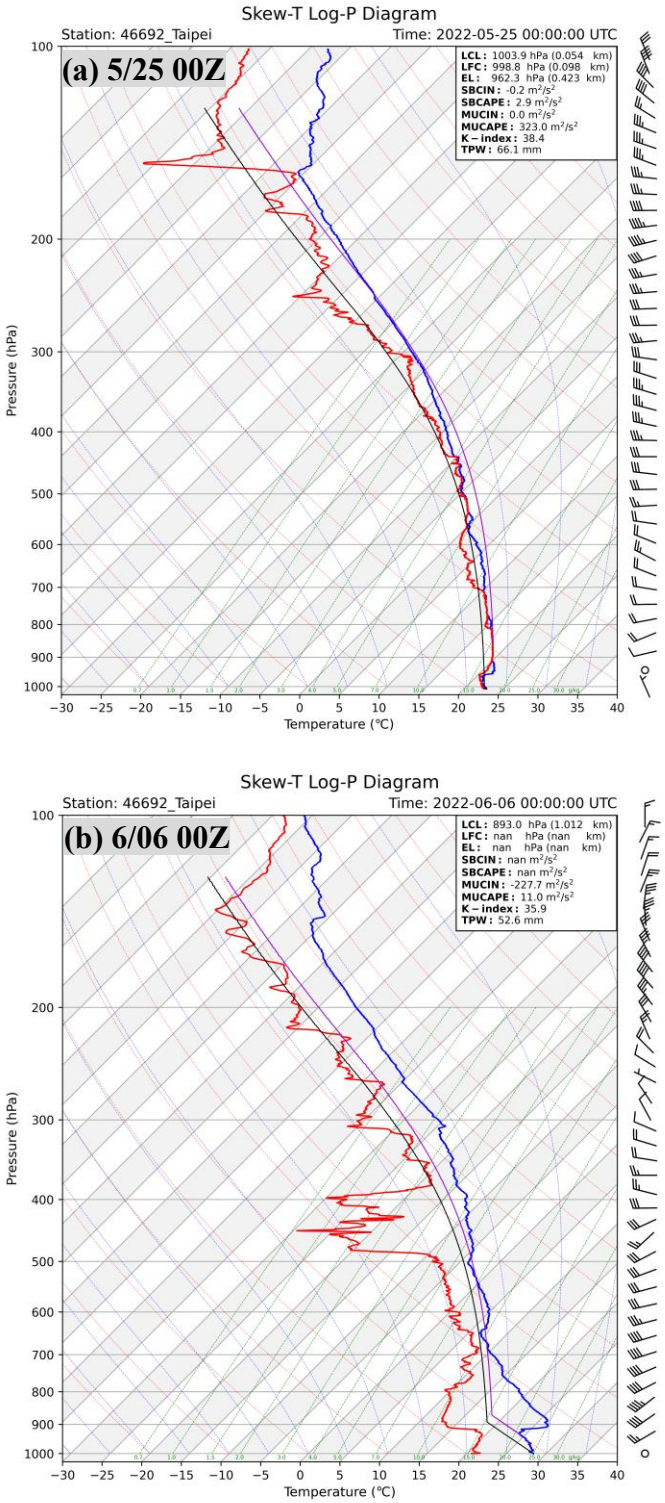

Figure 4.11 Sounding observations at Banqiao station for (a) 5/25 0000 Z (SOP1 case) and (b) 6/06 0000 Z (IOP3 case), with the temperature profile in blue and the dewpoint profile in red.

doi:10.6342/NTU202504817

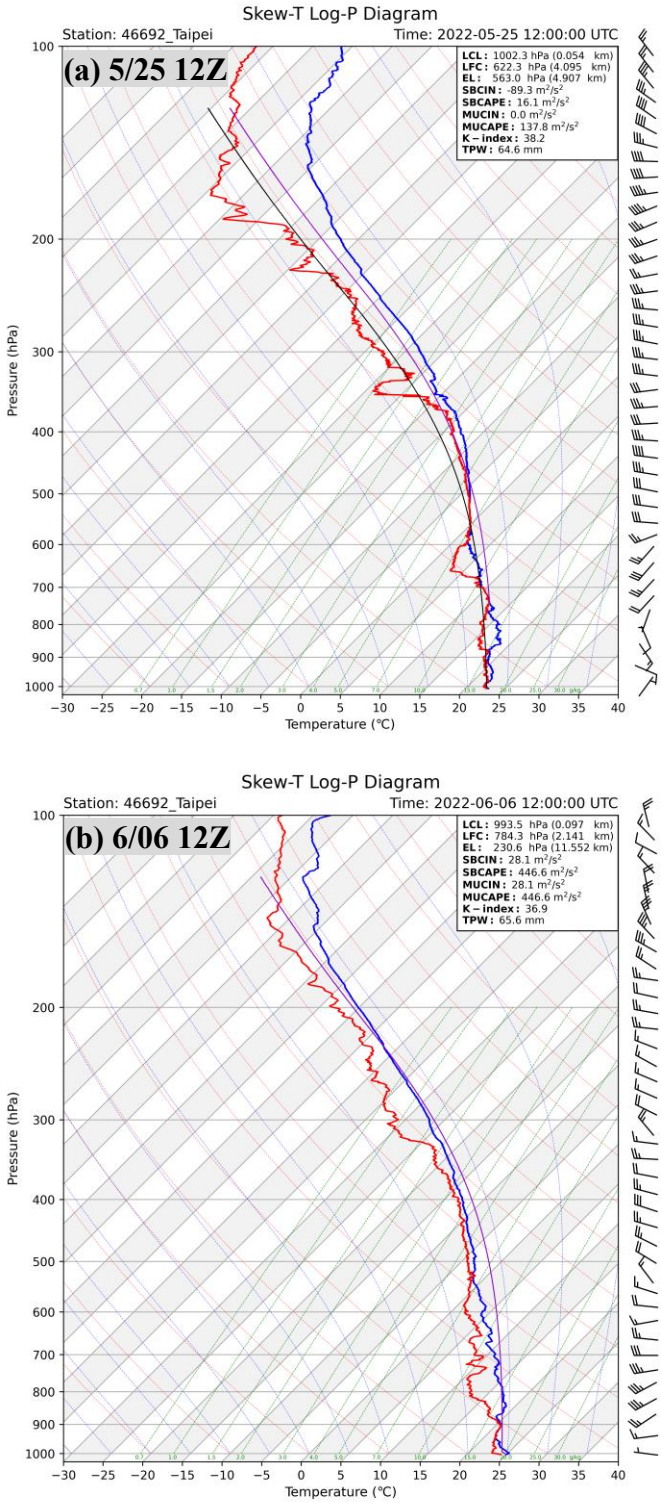

Figure 4.12 As in Figure 4.11, but for (a) 5/25 1200 Z (SOP1 case) and (b) 6/06 1200 Z (IOP3 case).

doi:10.6342/NTU202504817

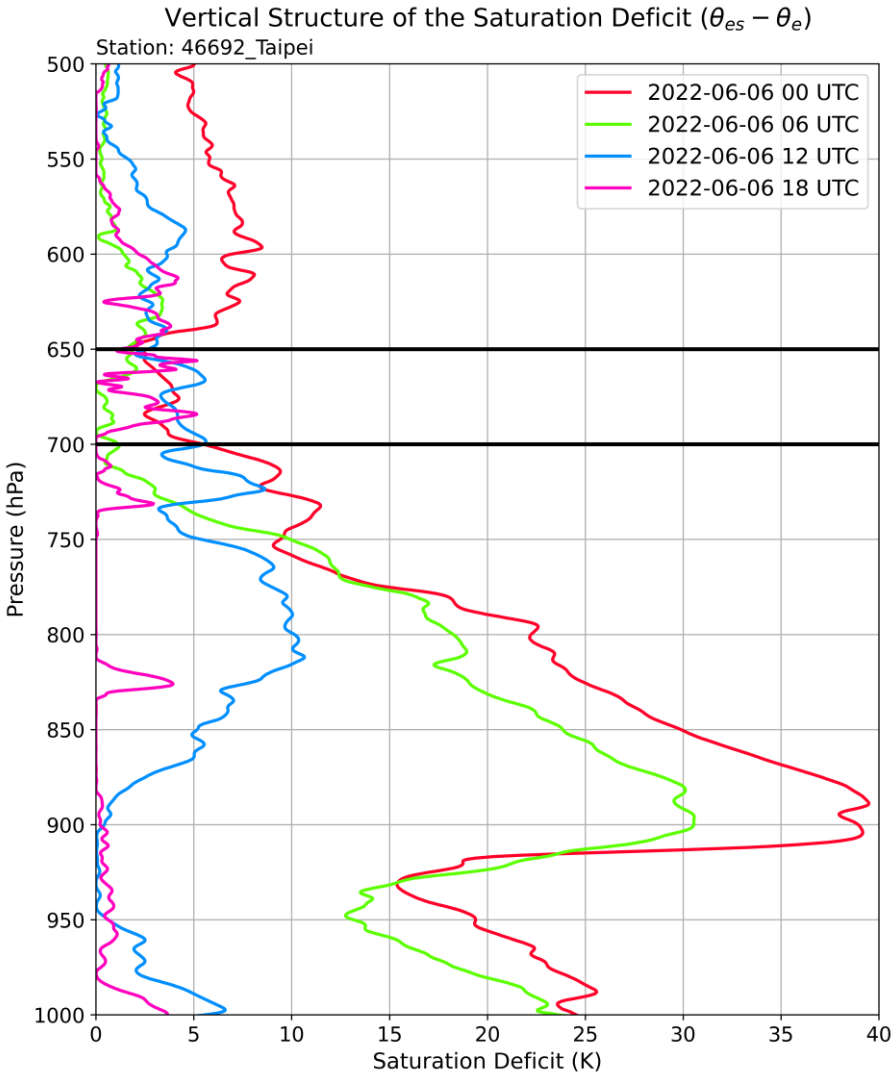

Figure 4.13 The temporal evolution of the difference between the saturation equivalent potential temperature (θ_{es}) and the equivalent potential temperature (θ_e), i.e., the saturation deficit, at Banqiao station for the IOP3 case at 0000 Z (red line), 0600 Z (green line), 1200 Z (blue line), and 1800 Z (pink line).

doi:10.6342/NTU202504817

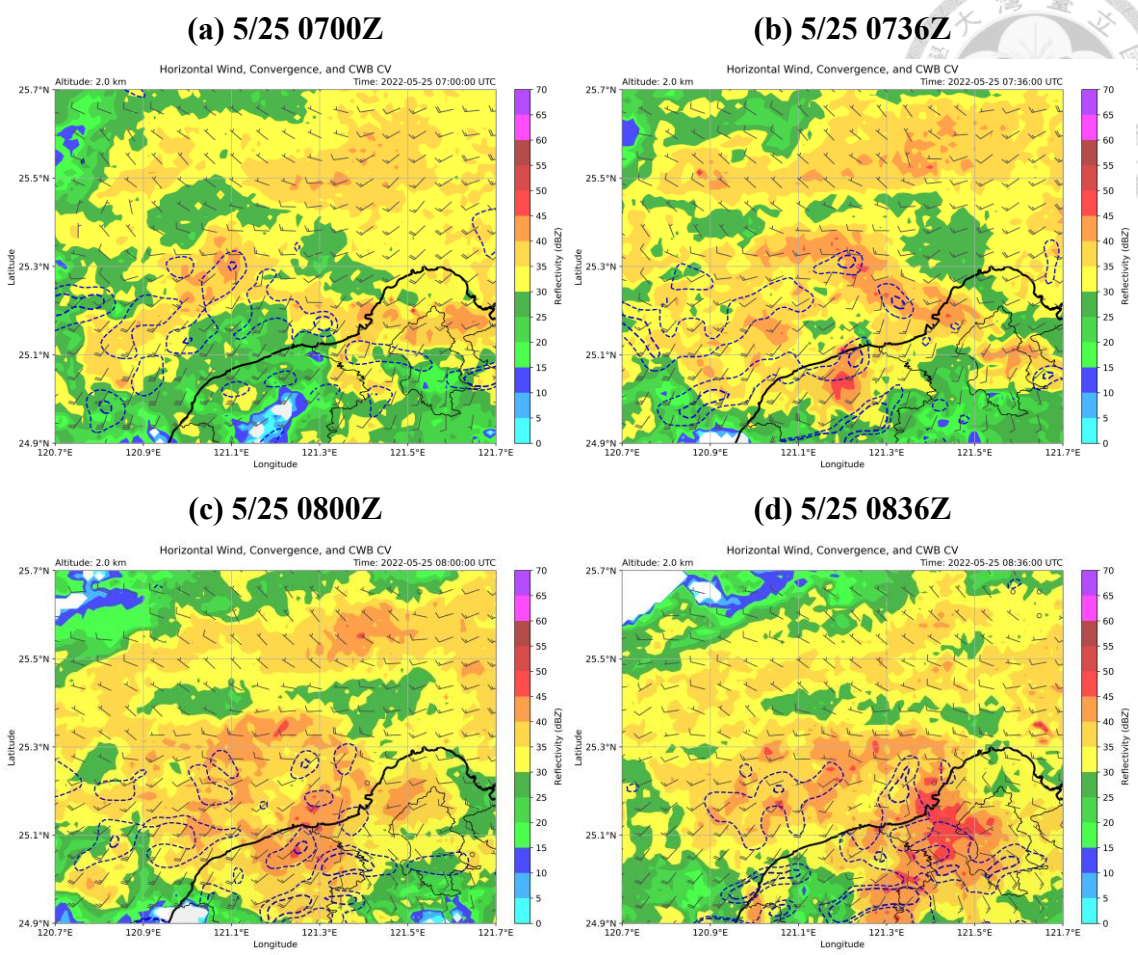

Figure 4.14 Horizontal winds at 2-km height retrieved from SAMURAI-TERRAIN (barbs; knots), convergence (blue dashed contours; s^{-1}, thick and thin contours denote -10 × 10^{-4} s^{-1} and -5 × 10^{-4} s^{-1}, respectively), and CWB composite reflectivity (color shading; dB*Z*) for the SOP1 case at (a) 0700 Z, (b) 0736 Z, (c) 0800 Z, and (d) 0836 Z.

doi:10.6342/NTU202504817

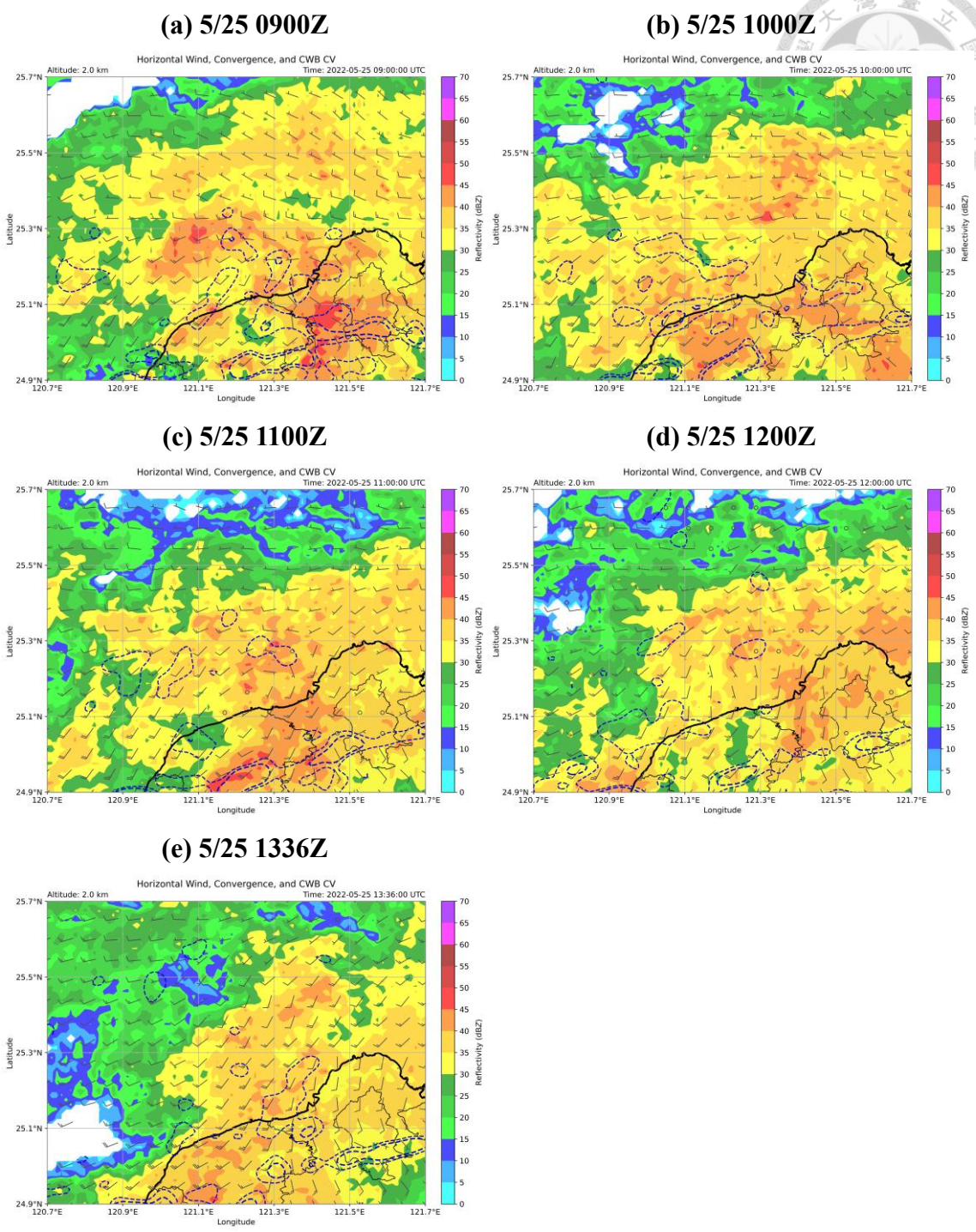

Figure 4.15 As in Figure 4.14, but for the SOP1 case at (a) 0900 Z, (b) 1000 Z, (c) 1100 Z, (d) 1200 Z, and (e) 1336 Z.

doi:10.6342/NTU202504817

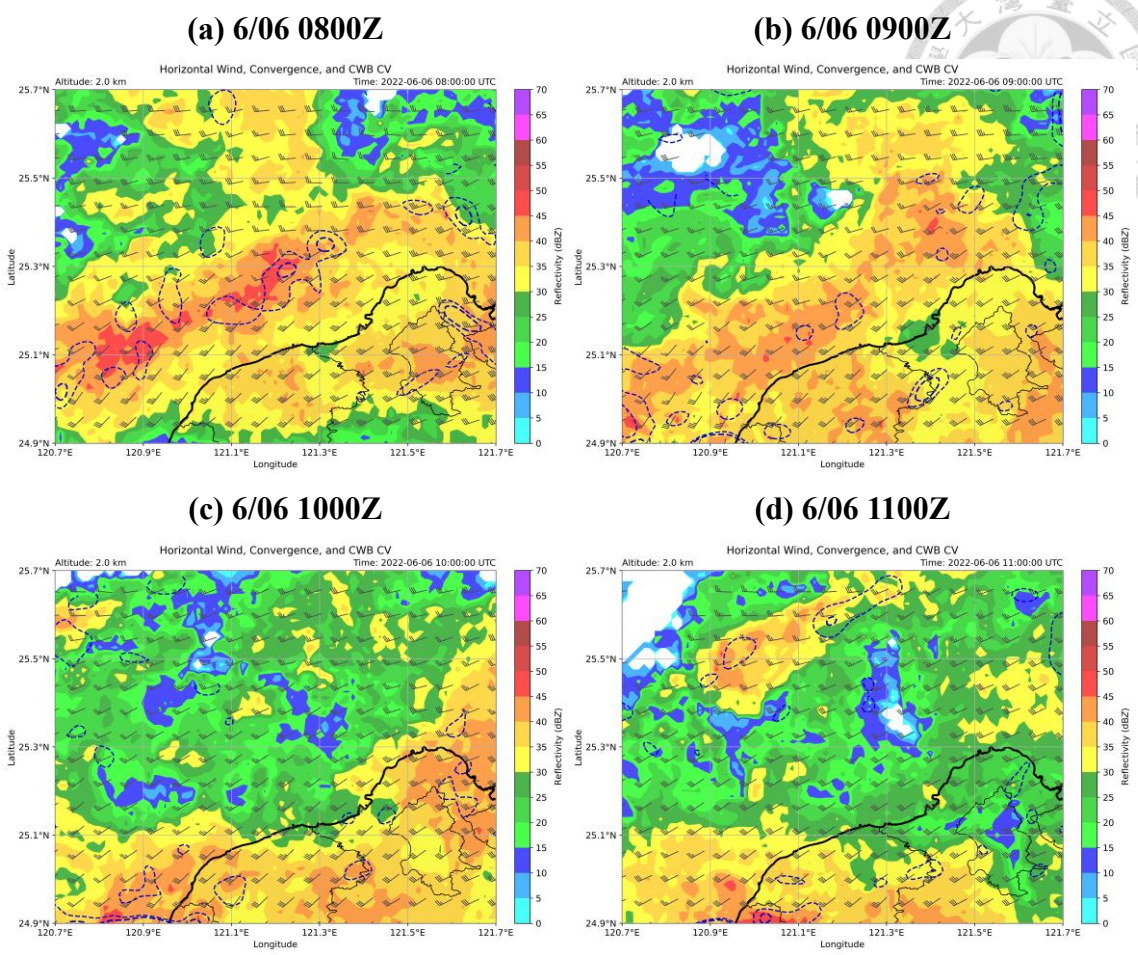

Figure 4.16 As in Figure 4.14, but for the IOP3 case at (a) 0800 Z, (b) 0900 Z, (c) 1000 Z, and (d) 1100 Z.

doi:10.6342/NTU202504817

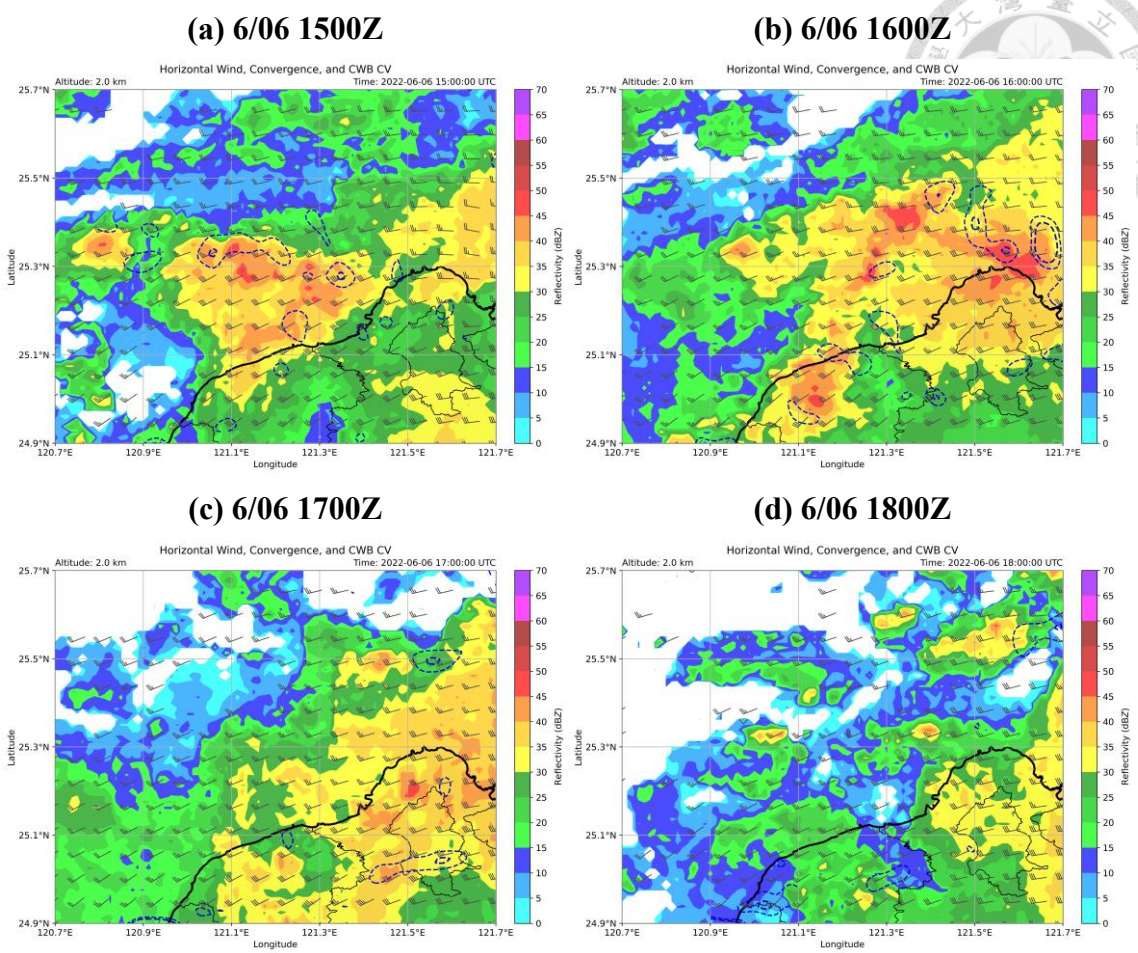

Figure 4.17 As in Figure 4.14, but for the IOP3 case at (a) 1500 Z, (b) 1600 Z, (c) 1700 Z, and (d) 1800 Z.

doi:10.6342/NTU202504817

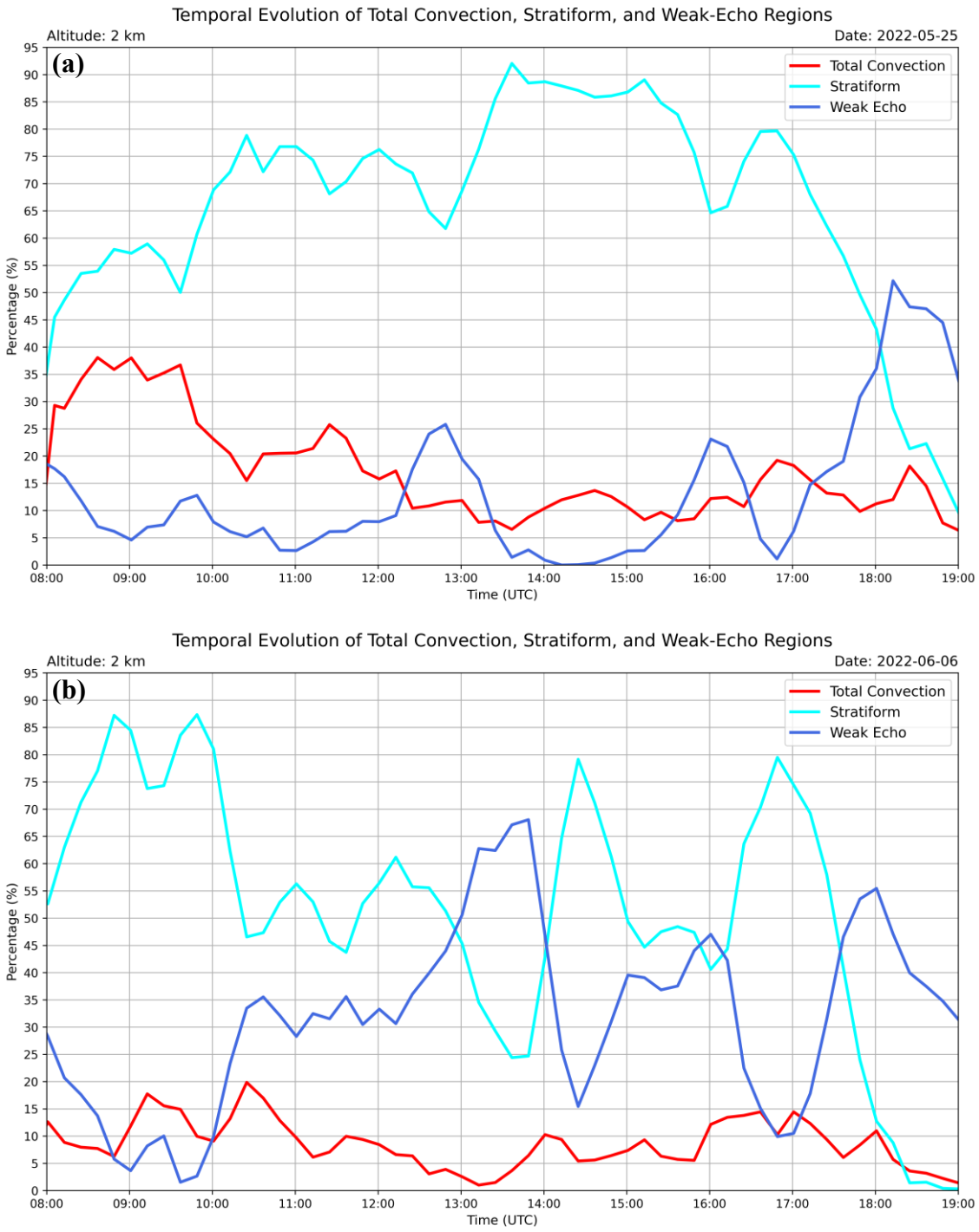

Figure 4.18 Temporal evolution of the total convective precipitation regimes (red line; including deep, moderate, and shallow convection), stratiform precipitation regimes (cyan line), and weak-echo regions (blue line) for (a) 5/25 0800–1900 Z and (b) 6/06 0800–1900 Z.

doi:10.6342/NTU202504817

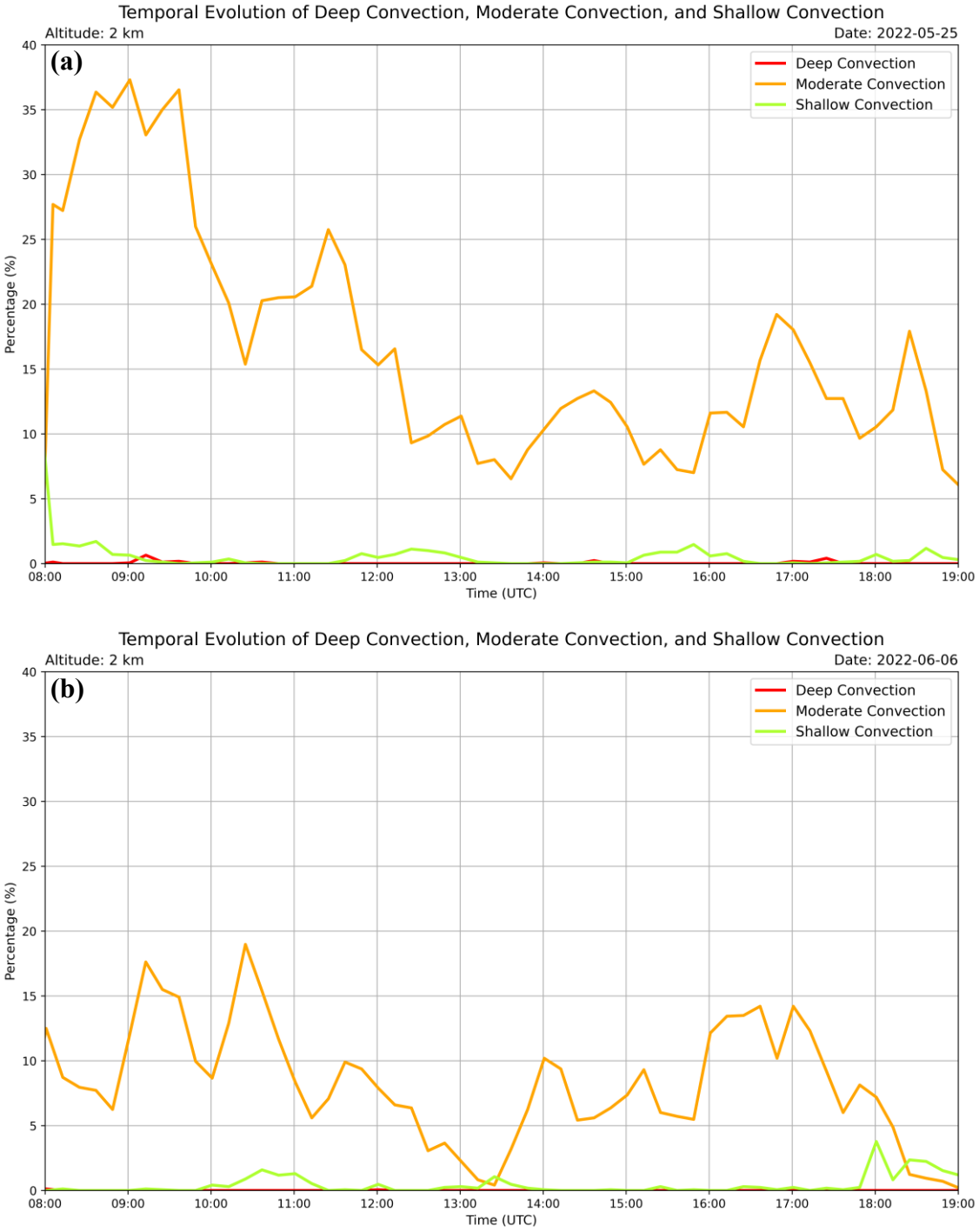

Figure 4.19 Temporal evolution of deep convection (red line), moderate convection (orange line), and shallow convection (green line) for (a) 5/25 0800–1900 Z and (b) 6/06 0800–1900 Z.

doi:10.6342/NTU202504817

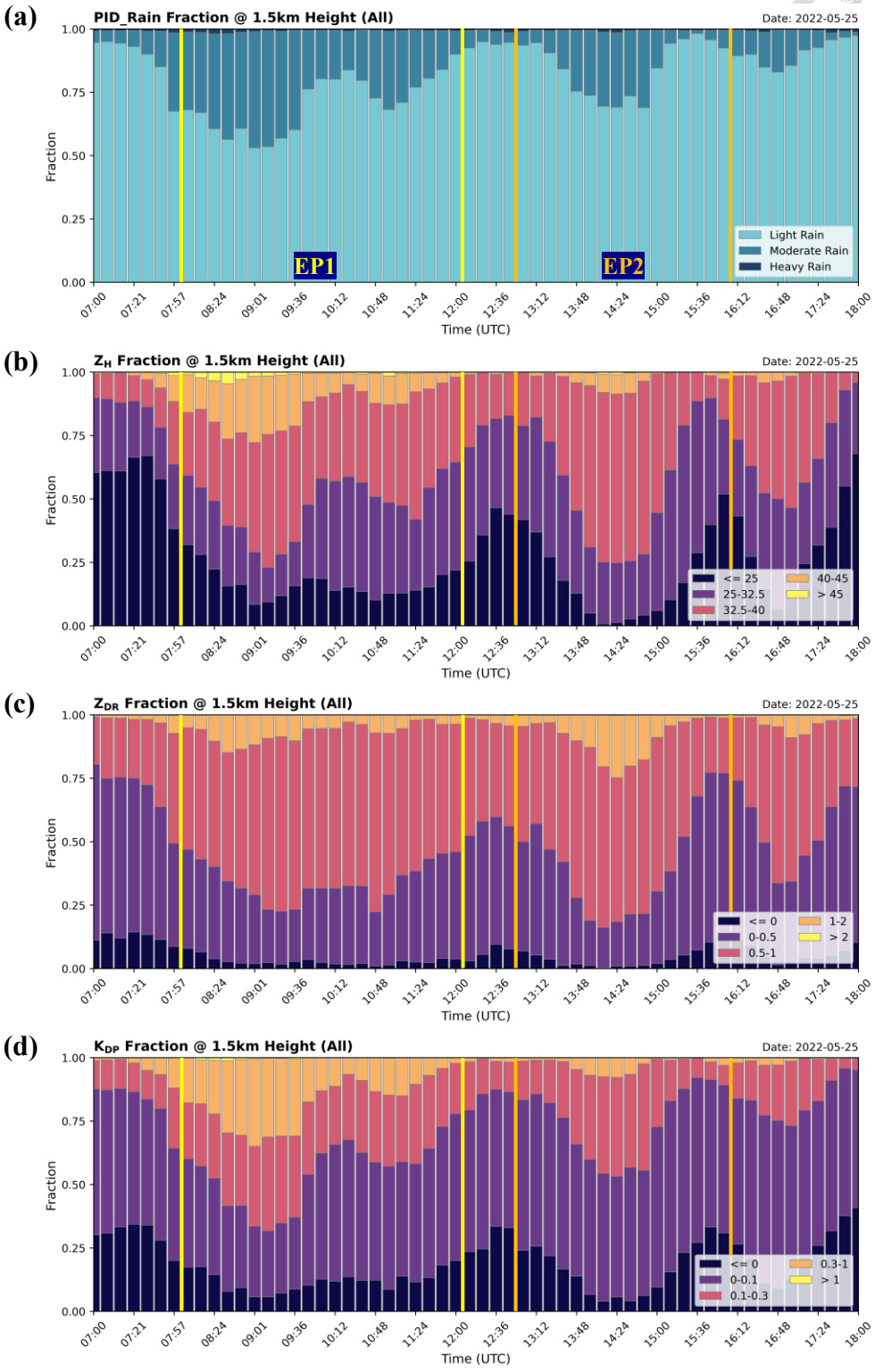

Figure 4.20 Temporal evolution of the fractions of S-Pol rain PID (light, moderate, and heavy rain) and polarimetric parameters at 1.5-km height for the SOP1 case: (a) rain PID, (b) Z_H, (c) Z_{DR}, and (d) K_{DP}. The first and second episodes of enhanced surface precipitation are bounded by yellow and orange lines, respectively.

doi:10.6342/NTU202504817

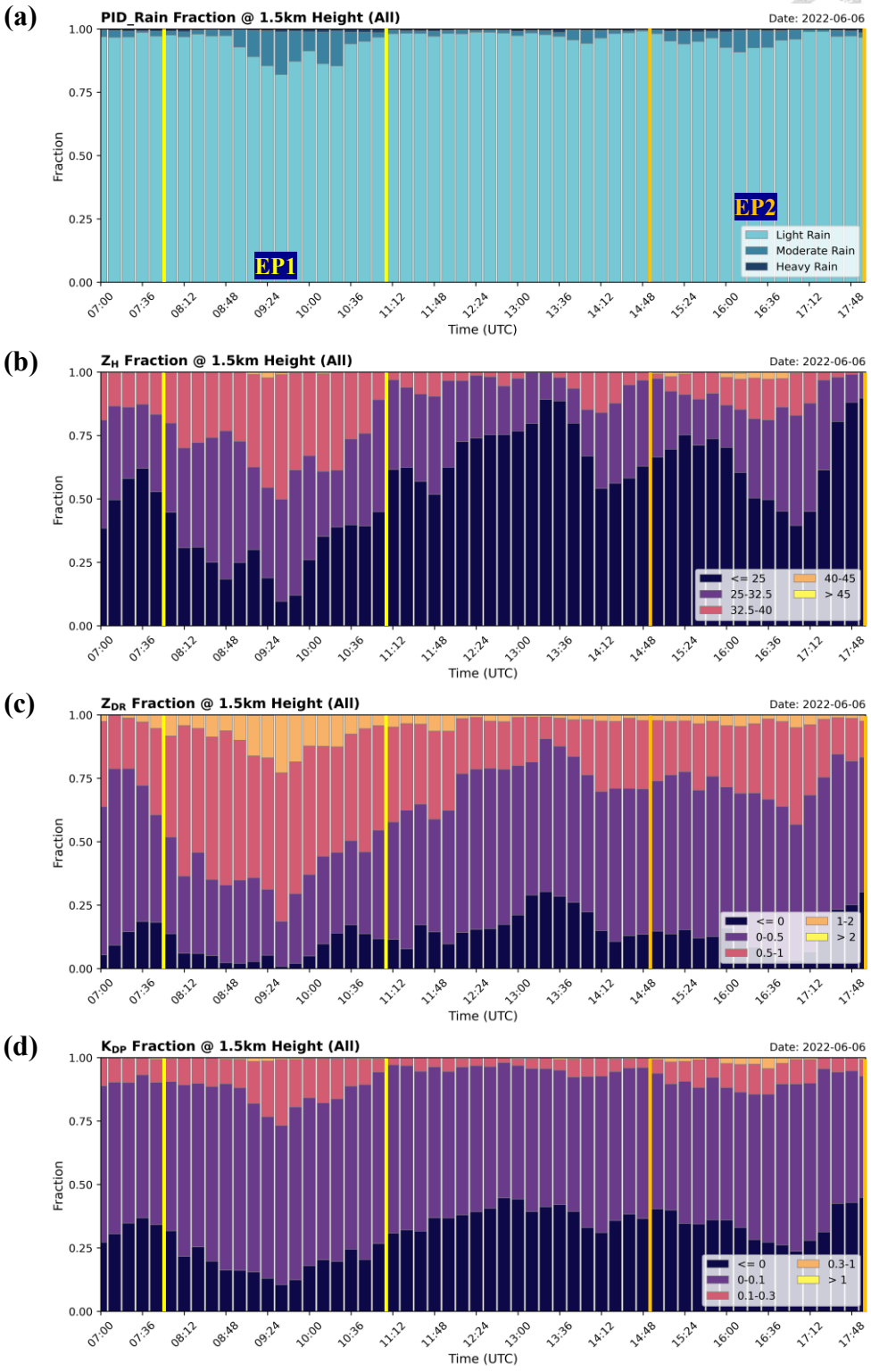

Figure 4.21 As in Figure 4.20, but for the IOP3 case.

doi:10.6342/NTU202504817

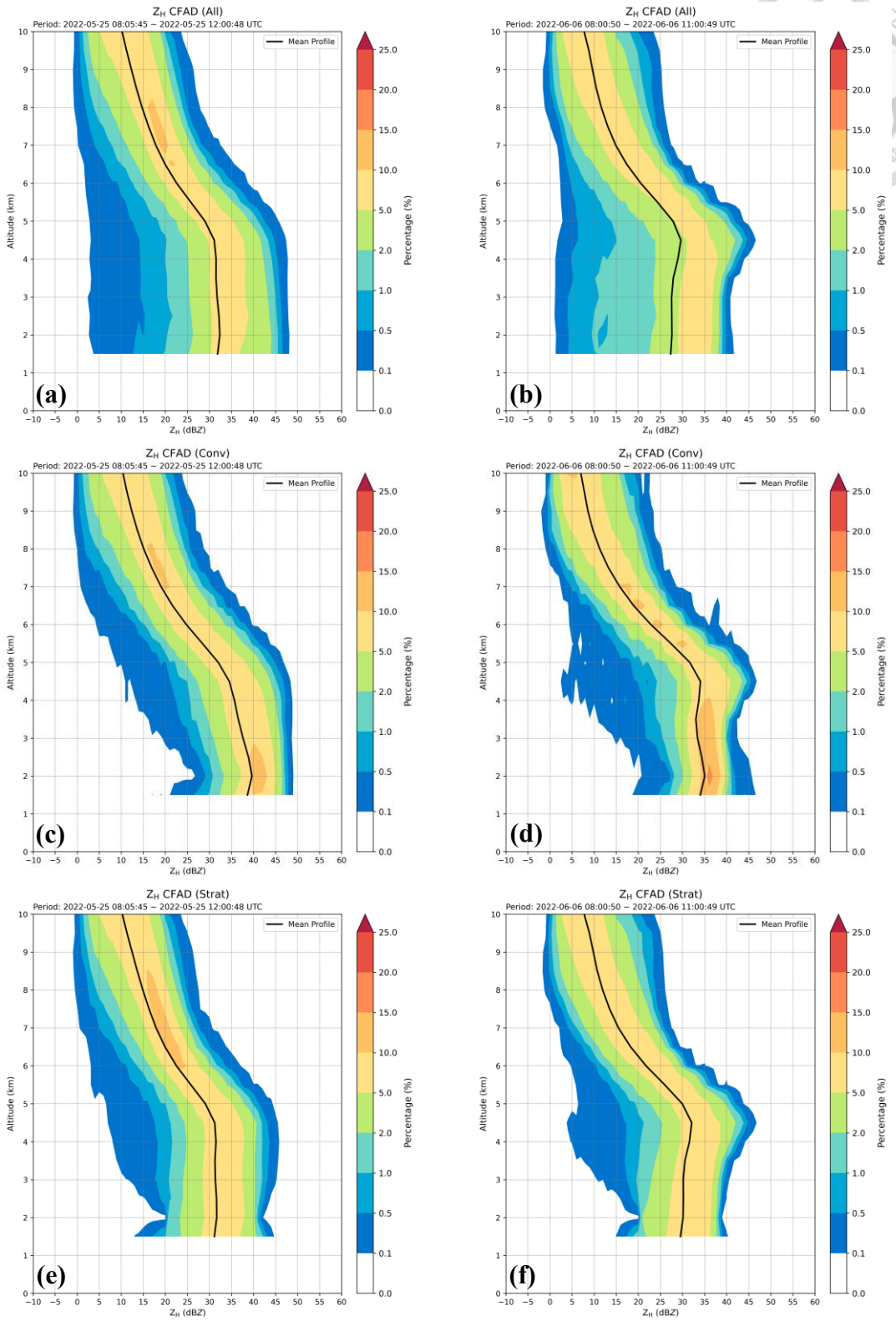

Figure 4.22 CFADs (%) of Z_H for EP1. (a),(c),(e) correspond to the SOP1 case, and (b),(d),(f) to the IOP3 case, with panels arranged by row as entire domain, convective, and stratiform precipitation regimes. The black line in each panel indicates mean profile.

doi:10.6342/NTU202504817

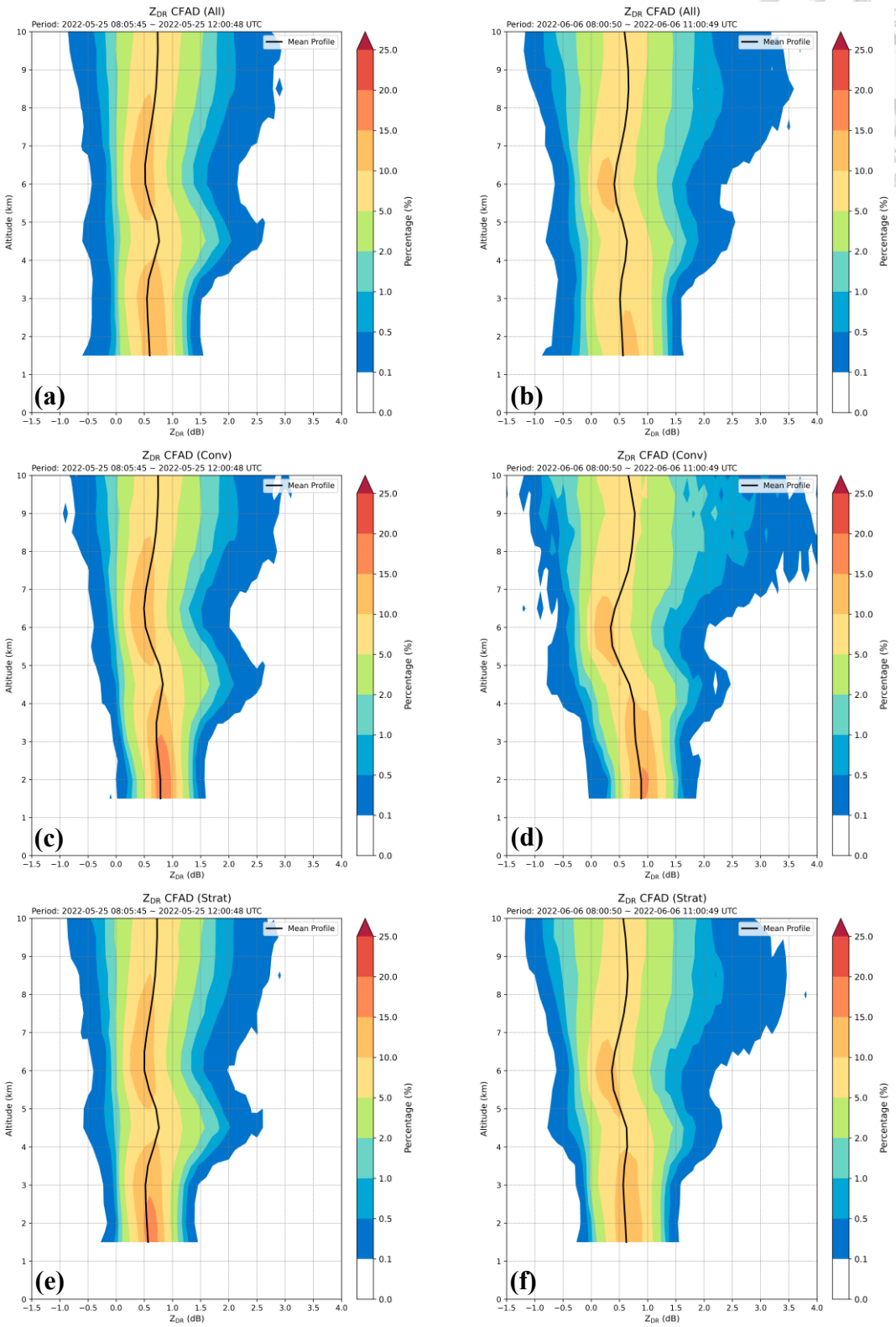

Figure 4.23 As in Figure 4.22, but for CFADs (%) of Z_{DR}.

doi:10.6342/NTU202504817

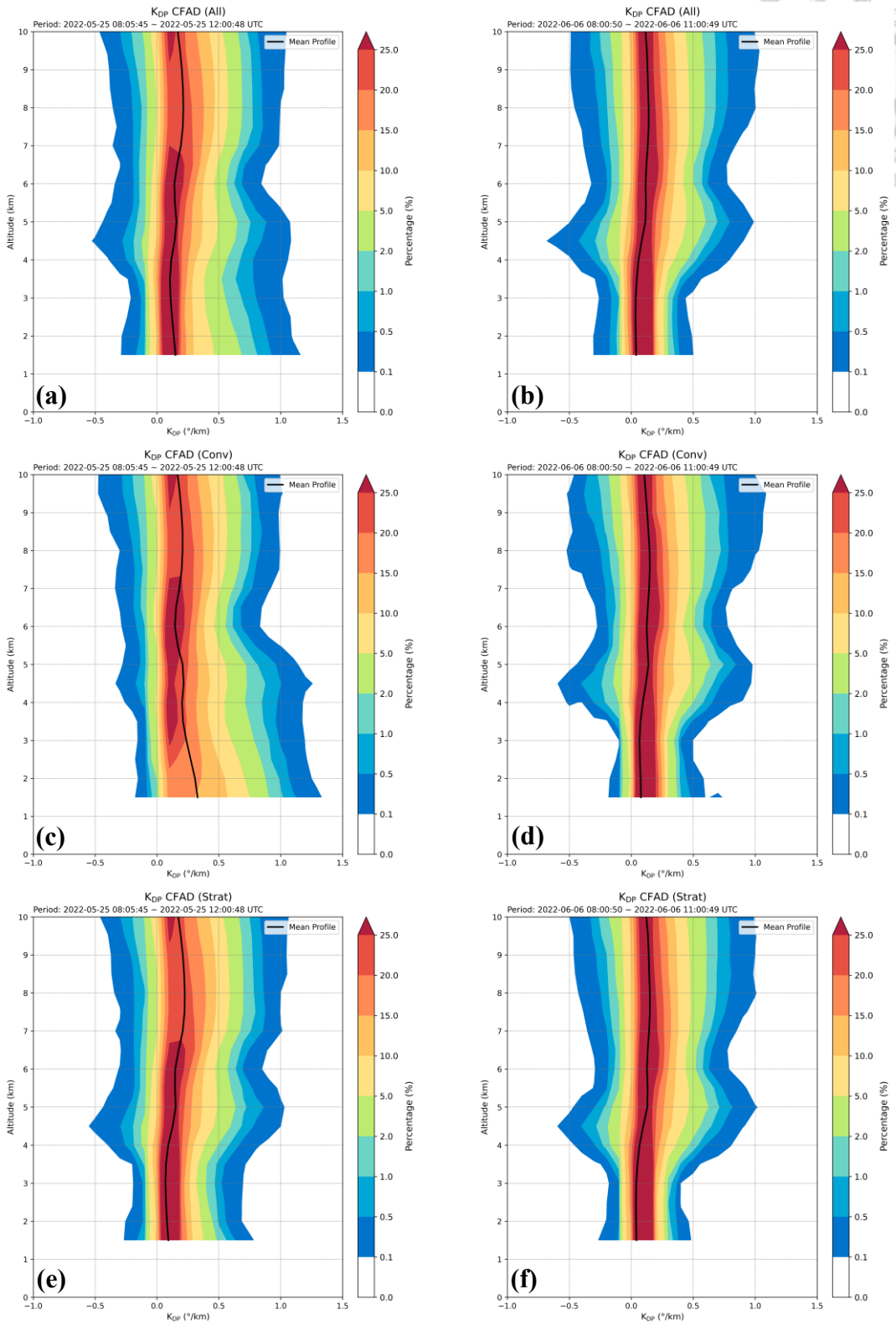

Figure 4.24 As in Figure 4.22, but for CFADs (%) of K_{DP}.

doi:10.6342/NTU202504817

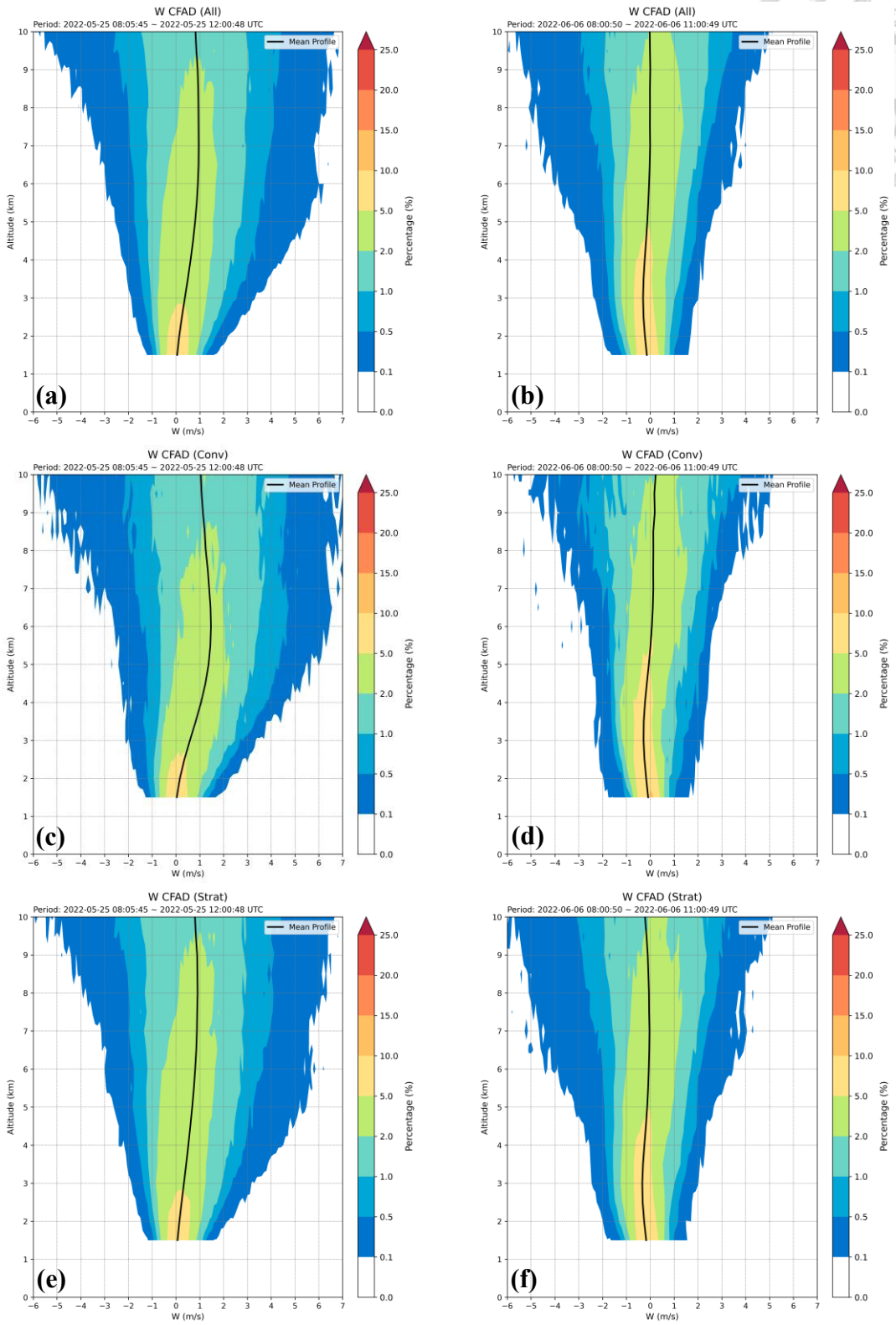

Figure 4.25 As in Figure 4.22, but for CFADs (%) of vertical velocity.

doi:10.6342/NTU202504817

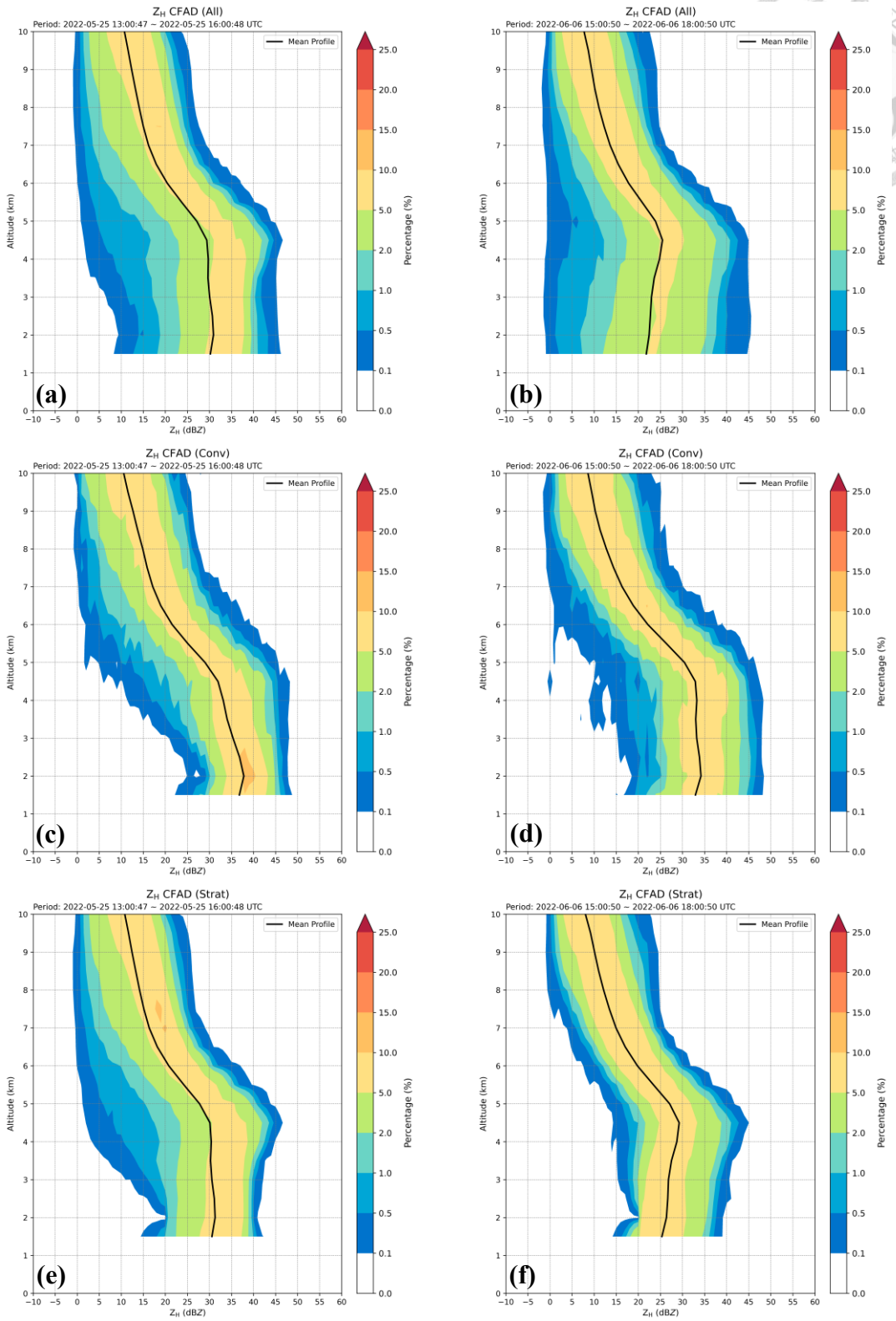

Figure 4.26 CFADs (%) of Z_H for EP2. (a),(c),(e) correspond to the SOP1 case, and (b),(d),(f) to the IOP3 case, with panels arranged by row as entire domain, convective, and stratiform precipitation regimes. The black line in each panel indicates mean profile.

doi:10.6342/NTU202504817

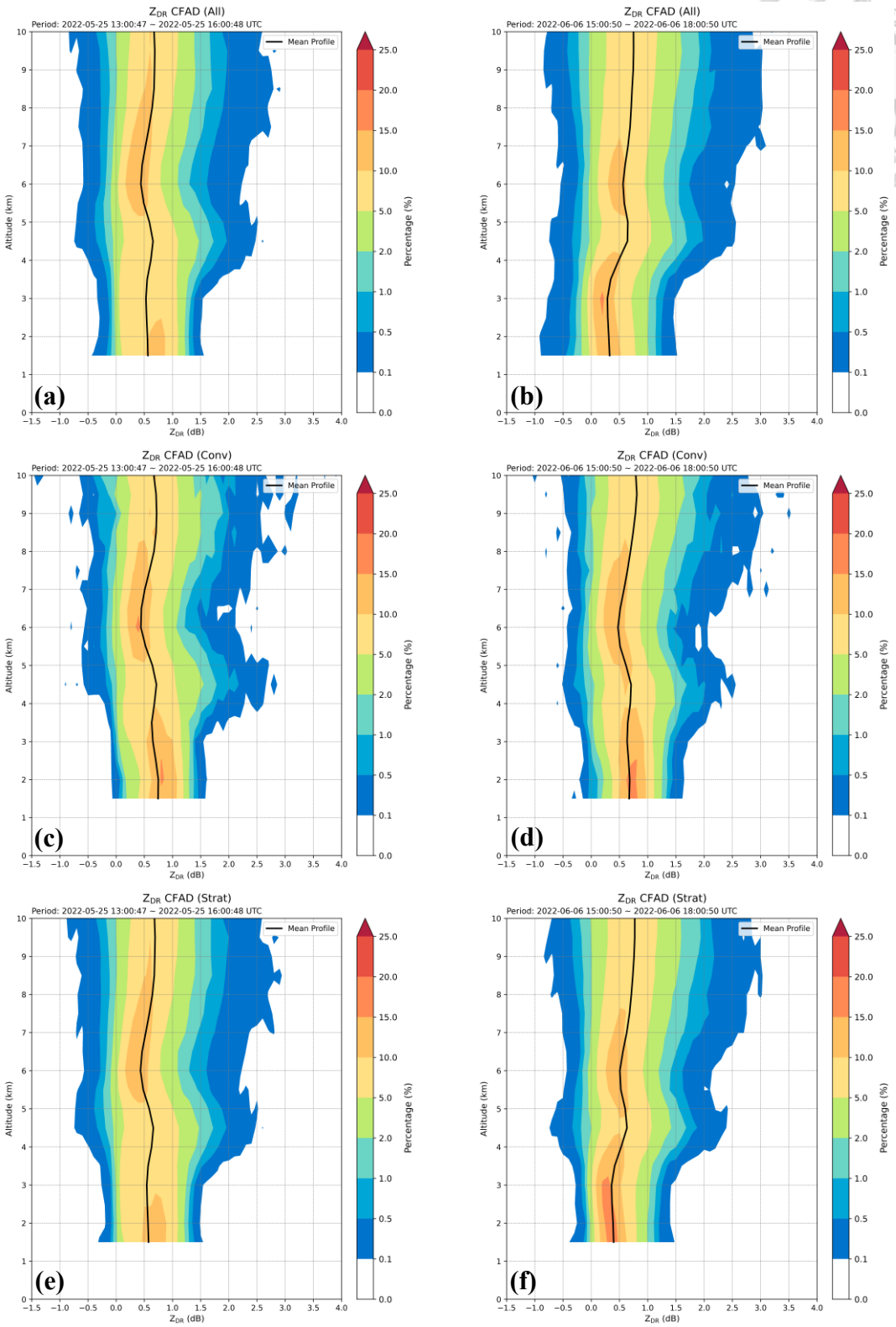

Figure 4.27 As in Figure 4.26, but for CFADs (%) of Z_{DR}.

doi:10.6342/NTU202504817

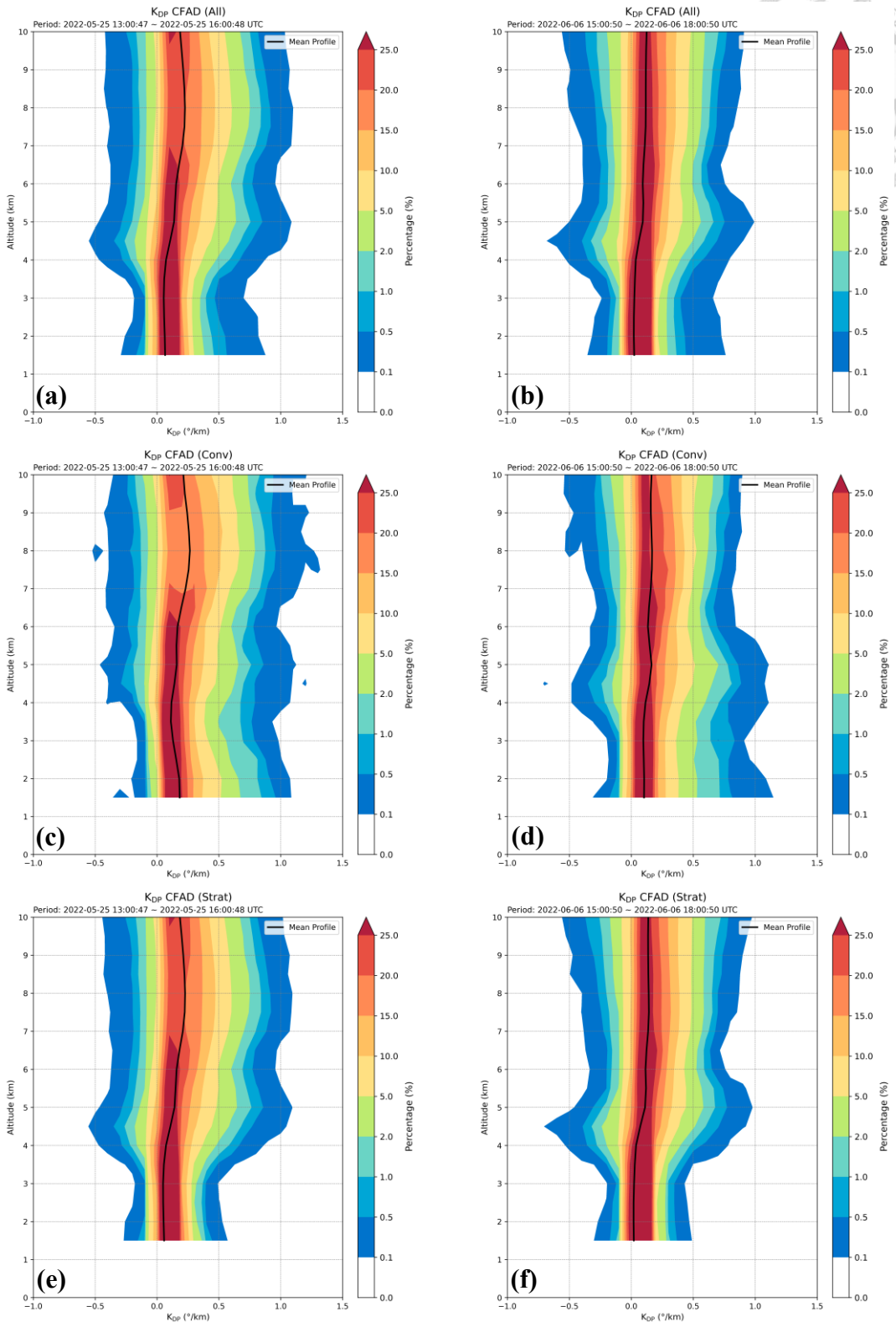

Figure 4.28 As in Figure 4.26, but for CFADs (%) of K_{DP}.

doi:10.6342/NTU202504817

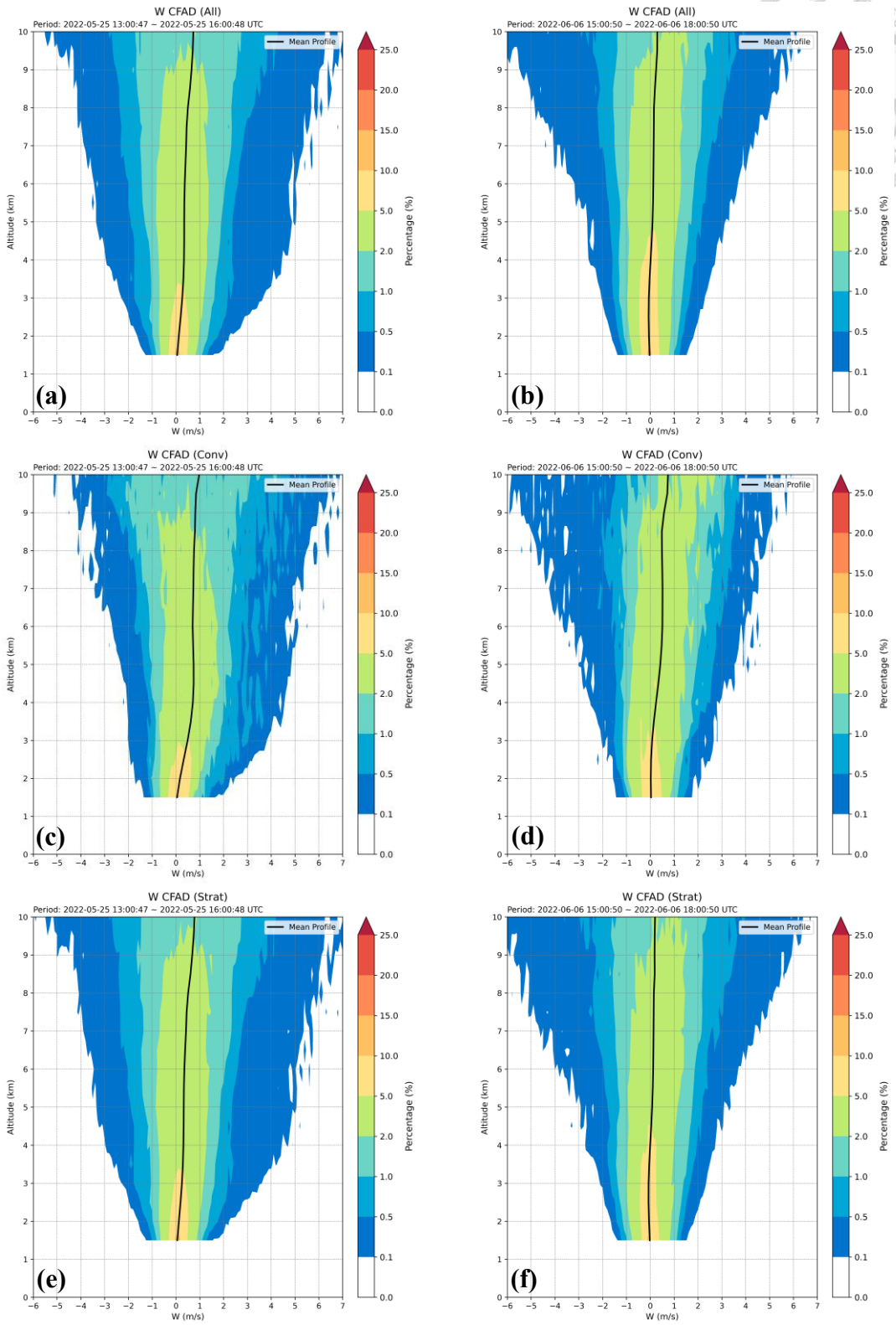

Figure 4.29 As in Figure 4.26, but for CFADs (%) of vertical velocity.

doi:10.6342/NTU202504817

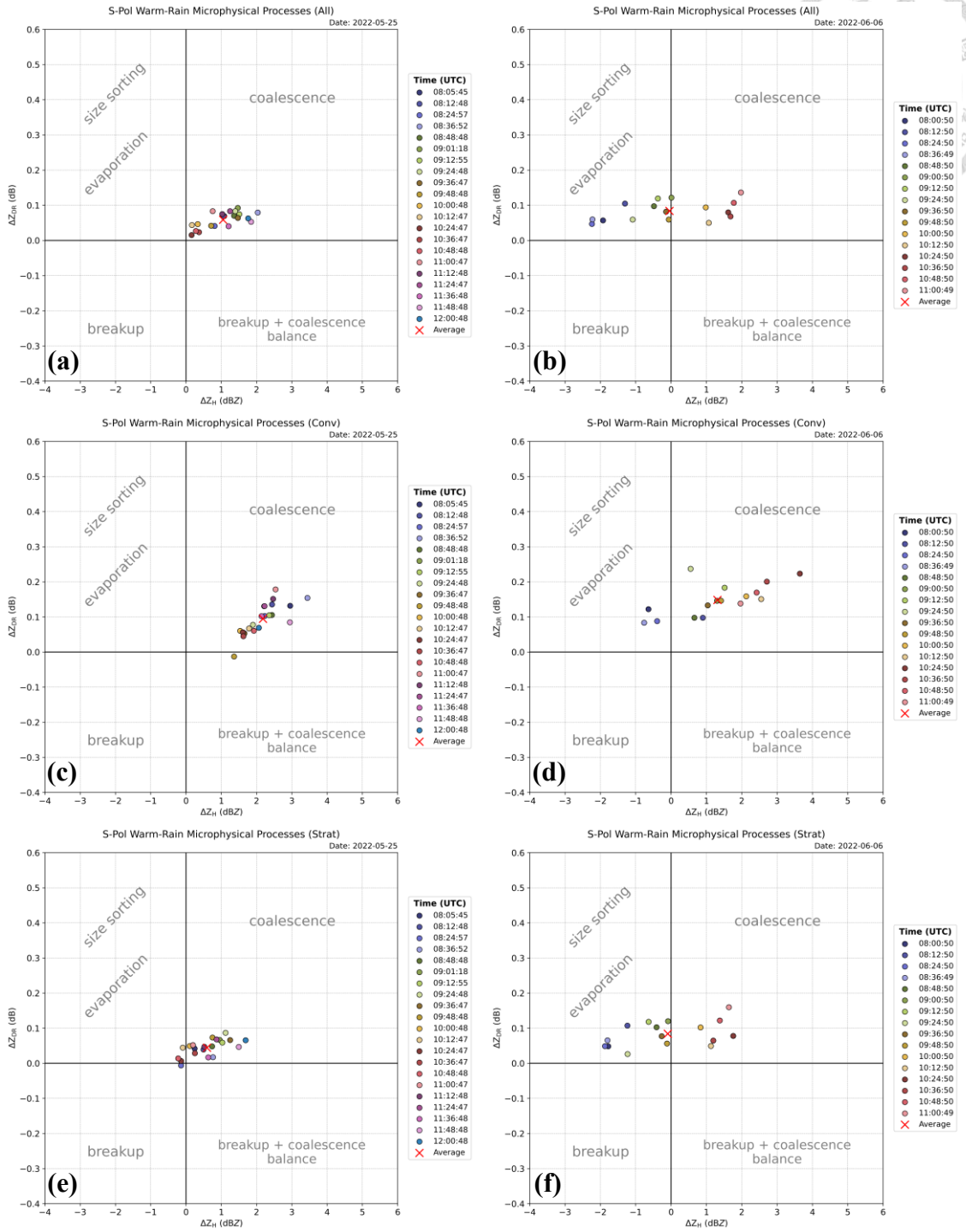

Figure 4.30 Four-quadrant parameter space for EP1. (a),(c),(e) correspond to the SOP1 case, and (b),(d),(f) to the IOP3 case, with panels arranged by row as entire domain, convective, and stratiform precipitation regimes. In each panel, colored dots represent individual time points (UTC), and the red cross represents their average. The corresponding microphysical processes for every quadrant are also annotated.

doi:10.6342/NTU202504817

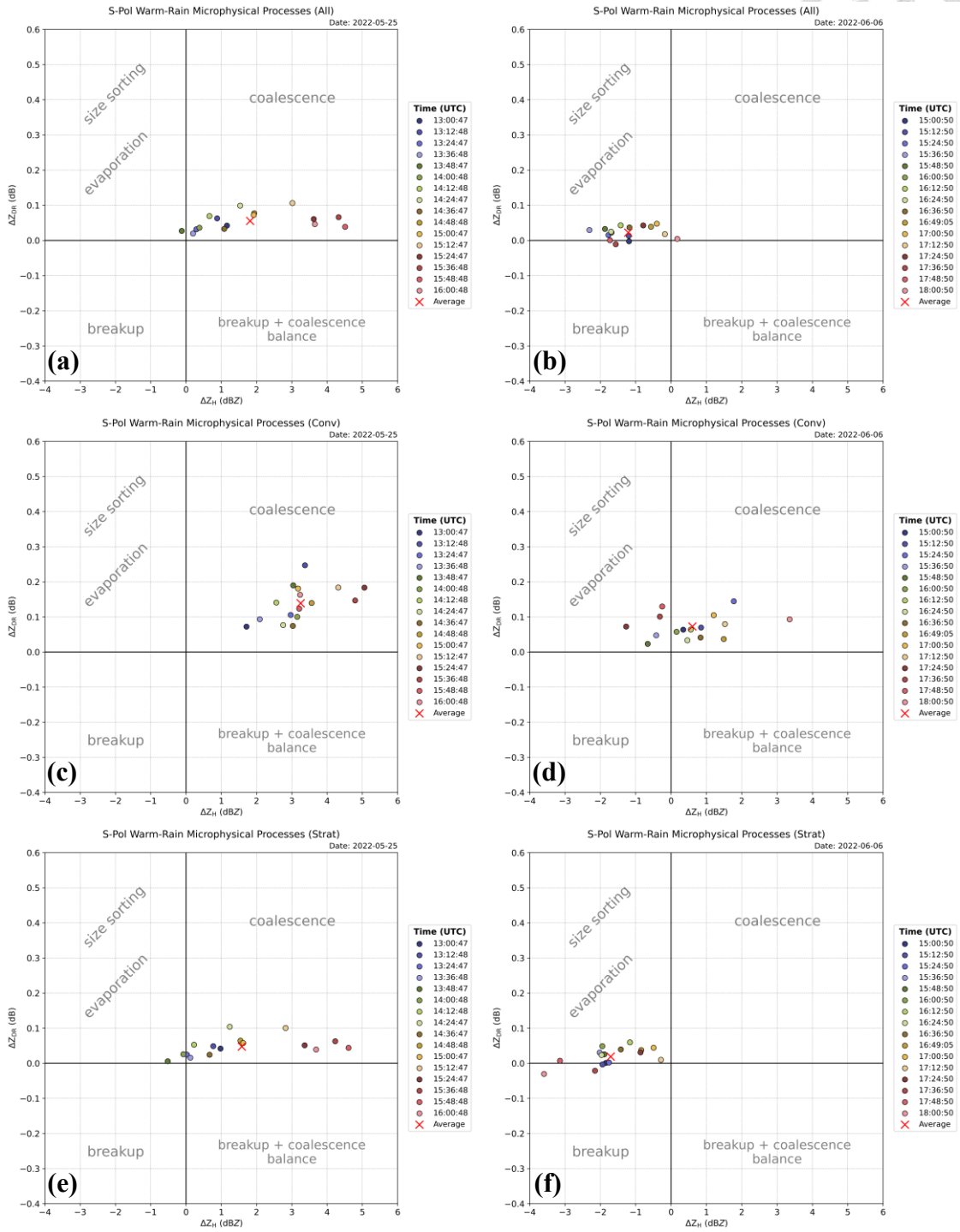

Figure 4.31 As in Figure 4.30, but for EP2.

doi:10.6342/NTU202504817

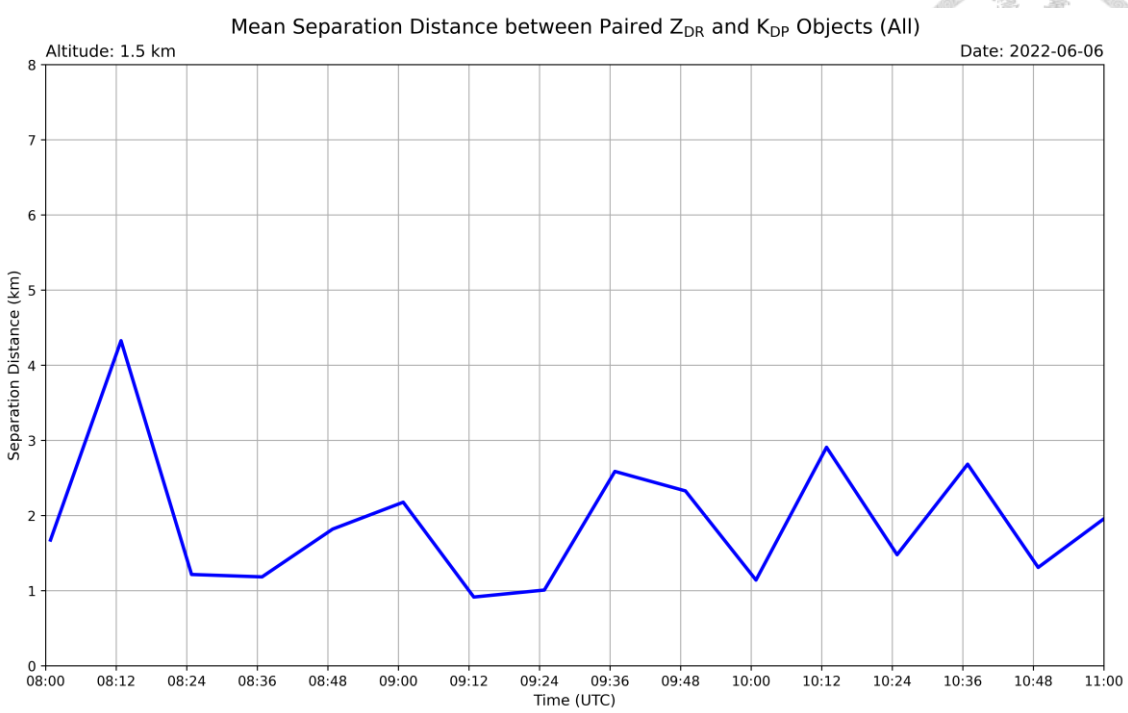

Figure 4.32 Time series of the mean separation distance between paired Z_{DR} and K_{DP} objects during EP1 of the IOP3 case over the entire analysis domain at 1.5-km height.

doi:10.6342/NTU202504817